



Chair of Automation

Doctoral Thesis



Future Distributed Geomonitoring
Analysis Methods, Algorithms &
Technologies

Dipl.-Ing. Roland Schmidt

December 2020



EIDESSTÄTLICHE ERKLÄRUNG

I declare on oath that I wrote this thesis independently, did not use other than the specified sources and aids, and did not otherwise use any unauthorized aids.

I declare that I have read, understood, and complied with the guidelines of the senate of the Montanuniversität Leoben for "Good Scientific Practice".

Furthermore, I declare that the electronic and printed version of the submitted thesis are identical, both, formally and with regard to content.

Datum 18.12.2020

Signature Author
Roland Schmidt



Copyright © 2020

Chair of Automation
Department Product Engineering
Montanuniversitaet Leoben
Peter-Tunner Straße 25
8700 Leoben, Austria

W: automation.unileoben.ac.at
E: automation@unileoben.ac.at
T: +43(0)3842/402-5301
F: +43(0)3842/402-5302

Cite this thesis as

```
@phdthesis{schmidt2020PhD,  
  Author = {Schmidt, Roland},  
  School = {Montanuniversitaet Leoben,  
            Department Product Engineering,  
            Chair of Automation},  
  Title  = {Future Distributed Geomonitoring - Analysis Methods,  
            Algorithms & Technologies},  
  Year   = {2020}}
```

All rights reserved.

Last compiled on December 22, 2020; the document has been compiled 1235 times in total.

This thesis was typeset using L^AT_EX (PDF_Latex, Bib_Tex and MakeIndex from Mac_TeX-2013). Formulas and equations are formatted according to ISO80000-2. Computations were performed using The MathWorks MATLAB (R2015a, R2015b, 2017a). Illustrations were designed using GNU Image Manipulation Program (GIMP V2.8), Inkscape. All registered trademarks and trade names are the property of their respective holders.

Acknowledgement

The research work was partly performed within the Celtic-Plus Project (Project-ID: C2013/2-2) "Advanced Sensing for Urban Monitoring" on the Chair of Automation, Montanuniversitaet Leoben in Cooperation with Geodata Messtechnik GmbH. This project was partially financed with the auspices of the CELTIC-Plus project ASUA (www.celticplus.eu/projectasua/), the Austrian financing for this project was provided by the Austrian Forschungsfoerderungsgesellschaft (FFG) and Geodata GmbH.

Very special thanks also go to Geodata MT GmbH, in particular to Johann Golser, Fritz Reissner and Klaus Chmelina for their support in the collaborative work on the ASUA project and for providing data and photos from the field. In addition, I would also like to thank all other project members of the ASUA project for their joint work.

At this point I would like to begin with a general word of thanks, without mentioning specific names, because every person with whom I have had contact has contributed to the creation of this work. Only through these contacts, even if it was only in early childhood, have I become what I am today. Of course, there are much more significant experiences and people who have had much more influence on this work than some stranger without a name, but nevertheless my evolution has been influenced by them.

Nevertheless, there are people and groups of people I want to thank in particular. The following individuals fall into this list, whereby it is not ordered on importance for contribution to this thesis:

- My doctoral supervisor, Prof. Paul O'Leary, for making it possible for me to write this thesis and for giving me the space at the department to develop scientifically to where I am today. Additionally, I must also take this opportunity to thank Prof. Peter Lee for his advice and review of this work.
- My girlfriend and my family, for supporting me in the last view years to finish this thesis and helping me to motivate, when the work on the thesis got stuck.
- The persons that supported me with their feedback to research topics of the thesis and gave me feedback during the writing process.
- The rest of my friends, the colleagues of the hunting group, the FabLab Leoben and the motorbike colleagues and working colleagues, who have brought me relaxation and variety.

Abstract

The core task of geo-monitoring is to find and employ suitable sensors and methods to monitor natural and artificial structures for changes and to trigger an alarm if necessary. In order to achieve this, reliable sensors and suitable evaluation methods are required. A reliable alarm process and long-term storage of the recorded data complete the requirements of such a system.

In the first part the inclination sensors commonly used in geo-monitoring are investigated in detail. Due to the differential measuring principle, the inclination sensors have a high temperature stability and the sensor noise is independent of the inclination. It was shown, that the noise of the inclination sensor following a differential measurement principle has a Cauchy Lorentz distribution. Therefore, different statistical methods have to be applied than for a normal distribution. By means of singular value decomposition it can be shown that the sensor elements have a different gain factor to each other. If orthogonalisation is applied on the data the confidence interval is improved by up to 34%.

The second part of the work is dedicated to discrete basis functions, which enable an advanced method for the reconstruction of structural displacements. Two independent measurements which follow physically different principles, e.g. 3D displacement measurements (total station) and slope measurements (inclinometer), are combined with each other by means of sensor fusion. Thereby, more reliable results can be achieved. Due to the efficiency of the analytical data processing, an implementation on local battery-powered embedded systems is possible.

In the last part of this thesis, the "ASUA Urban Automation Reference Platform" and the associated devices, which were (co-)developed in the Celtic-Next project "*Advanced Sensing for Urban Automation*" (ASUA), are discussed. Due to the continuous change in the requirements for geo-monitoring devices with regard to networking, integration into heterogeneous systems and data availability, these systems must also adapt. The developed devices enable local data processing for complex problems (reconstruction), local alarms and control via a cloud-based control system.

The solutions found in the work provide the basis for a new generation of connected geo-monitoring devices that enable intelligent local data processing. The model-based reconstruction allows a significant improvement of the results by data combination and tolerates failures of single measurement sensors. The detailed sensor analysis shows that the usual statistics fail for many sensors used in geo-monitoring. Thus, other statistical methods and filters have to be applied to obtain reliable results.

Keywords

Geo-monitoring, inclinometers, basis functions, Cauchy-Lorentz distribution, model based reconstruction, condition monitoring

Kurzfassung

Die Kernaufgabe des Geomonitorings ist es, mit geeigneten Sensoren und Methoden natürliche und künstliche Strukturen auf Veränderungen zu überwachen und nötigenfalls Alarm auszulösen. Um dies bewerkstelligen zu können, werden neben zuverlässigen Sensoren auch geeignete Auswertemethoden benötigt. Ein zuverlässiger Alarmierungsweg und langfristige Speicherung der aufgenommenen Daten runden das System ab.

Im ersten Teil werden die oft im Geomonitoring verwendeten Neigungssensoren detailliert analysiert. Durch das differenzielle Messprinzip weisen die Neigungssensoren eine sehr hohe Temperaturstabilität auf und das Sensorrauschen ist neigungsunabhängig. Es wurde gezeigt, dass das Rauschen des Neigungssensors, der nach einem Differenzialmessprinzip arbeitet, eine Cauchy Lorentz Verteilung aufweist. Daher müssen andere statistische Methoden als bei einer Normalverteilung angewendet werden. Mittels Singulärwertzerlegung lässt sich zeigen, dass die Sensorelemente einen unterschiedlichen Verstärkungsfaktor zueinander aufweisen. Korrigiert man dies durch orthogonalisieren der Daten, verbessert sich das Konfidenzintervall um bis zu 34 %.

Der zweite Teil der Arbeit widmet sich diskreten Basisfunktionen, die eine fortgeschrittene Methode zum Rekonstruieren von Verformungen an Bauwerken ermöglichen. Zwei voneinander unabhängige Messungen die physikalisch unterschiedlichen Prinzipien folgen, z.B. 3D Verschiebungsmessungen (Total station) und Neigungsmessungen (Inklinometer), werden mittels Informationsfusion miteinander kombiniert wobei verlässlichere Ergebnisse erreicht werden können. Durch die Effizienz der analytischen Datenverarbeitungsmethoden ist eine Umsetzung auf lokalen batteriebetriebenen Datenloggern mit eingebetteten Systemen möglich.

Im letzten Teil wird auf eine, während dieser Dissertation im Rahmen des Celtic-Next Projekts "*Advanced Sensing for Urban Automation*" (ASUA), (mit-)entwickelte "ASUA Urban Automation Reference Platform" und die damit verbundenen Geräte eingegangen. Durch die laufende Änderung der Anforderungen an Geomonitoring Geräte in Bezug auf Vernetzung, Integration in heterogene Systeme und Datenverfügbarkeit, müssen sich auch diese Geräte anpassen. Die gefundene Lösung ermöglicht die lokale Datenverarbeitung bei komplexen Problemen (Rekonstruktion), lokale Alarmierung und eine Steuerung über ein cloud-basiertes Kontrollsystem.

Die in der Arbeit gefundenen Lösungen bieten die Grundlage für eine neue Generation von vernetzten Geomonitoring Geräten, die intelligente lokale Datenverarbeitung ermöglichen. Die modellbasierte Rekonstruktion ermöglicht eine maßgebliche Verbesserung der Ergebnisse durch Datenkombination und toleriert Ausfälle von einzelnen Messsensoren. Die detaillierte Sensoranalyse zeigt, dass die üblicherweise verwendete Statistik bei vielen der hier verwendeten Sensoren versagt und andere statistische Methoden und Filter angewendet werden müssen um verlässliche Ergebnisse zu erhalten.

Schlagwörter

Geomonitoring, Neigungssensoren, Basisfunktionen, Cauchy Lorentz Verteilung, modellbasierte Rekonstruktion, Zustandsüberwachung

Glossary

| | | |
|---|-----|--|
| x, y | ... | scalar |
| \hat{x}, \hat{y} | ... | estimator for scalar |
| \mathbf{x}, \mathbf{y} | ... | vector |
| $\hat{\mathbf{x}}, \hat{\mathbf{y}}$ | ... | estimator for vector |
| \mathbf{X}, \mathbf{Y} | ... | matrix |
| $\mathbf{x}^T, \mathbf{X}^T$ | ... | transposed vector, transposed matrix |
| $\mathbf{X}^{-1}, \mathbf{X}^+, \mathbf{X}^-$ | ... | inverse, pseudoinverse, generalised inverse matrix |
| $\mathbf{X} \circ \mathbf{Y}$ | ... | Hadamard product |
| $\mathbf{X} \otimes \mathbf{Y}$ | ... | Kronecker product |
| $\mathbf{x} * \mathbf{y}$ | ... | convolution |
| $\{x, y\}$ | ... | a set of variables |
| x_i | ... | i^{th} element of \mathbf{x} |
| x_{ij} | ... | i^{th} row / j^{th} column element of \mathbf{X} |
| i, j, k | ... | indexing variables |
| m, n | ... | number of rows, columns, samples, etc. |
| α, β, γ | | coefficients of a polynomial |
| $\mathbf{0}$ | ... | vector of zeros |
| $\mathbf{1}$ | ... | vector of ones |
| \mathbf{e}_i | ... | unit vector in i^{th} dimension |
| \mathbf{I} | ... | identity matrix |
| \mathbf{W} | ... | weighting matrix |
| \mathbf{J} | ... | Jacobian matrix |
| \mathbf{L} | ... | linear operator |
| \mathbf{B} | ... | general basis |
| \mathbf{G} | ... | discrete orthogonal polynomial basis |
| \mathbf{D} | ... | differentiating matrix |
| $\mu_{\mathbf{x}}$ | ... | expectation value of \mathbf{x} |
| \bar{x} | ... | sample mean of \mathbf{x} |
| $\sigma_{\mathbf{x}}^2$ | ... | variance of \mathbf{x} |
| $s_{\mathbf{x}}^2$ | ... | sample variance of \mathbf{x} |
| $\Lambda_{\mathbf{x}}$ | ... | covariance matrix of \mathbf{x} |
| ν | ... | degrees of freedom (d.f.) |
| $t_{(\nu)}$ | ... | Student distribution with ν d.f. |
| $\mathcal{F}_{(\nu_1, \nu_2)}$ | ... | Fisher distribution with ν_1 and ν_2 d.f. |
| $\chi_{(\nu)}^2$ | ... | Chi-squared distribution with ν d.f. |
| i.i.d. | ... | independent and identically distributed |

Contents

| | | |
|----------|---|-----------|
| 1 | Introduction | 1 |
| 1.1 | Monitoring of Structure | 2 |
| 1.2 | Outline of the Thesis | 4 |
| 1.3 | Original Work | 5 |
| 1.4 | List of Publications | 7 |
| 2 | Analysis of Inclination Sensing Elements | 9 |
| 2.1 | MEMS technology for inclination sensors | 9 |
| 2.2 | Comparison of Different Inclination Sensors | 11 |
| 2.3 | SCA103T-D04 Inclination Sensor | 12 |
| 2.4 | Characterisation of the SCA103T | 14 |
| | 2.4.1 Histograms and Distributions for $x(t)$ and $y(t)$ | 18 |
| | 2.4.2 Correlation in the Perturbations of $x(t)$ and $y(t)$ | 21 |
| 2.5 | Long-term Laboratory Measurement | 24 |
| 2.6 | The SCA830 Single Axis Inclination Sensor | 25 |
| 3 | Model Based Reconstruction | 29 |
| 3.1 | Physical Deformation Model | 30 |
| 3.2 | Polynomials | 32 |
| | 3.2.1 Design of Polynomials | 33 |
| | 3.2.2 Polynomial Regression | 34 |
| | 3.2.3 Covariance Propagation | 36 |
| 3.3 | Constrained Polynomials | 39 |
| | 3.3.1 Polynomials with Constraining Roots | 40 |
| | 3.3.2 Polynomial with Constraining Value Pairs | 42 |
| | 3.3.3 Polynomial Approximation with Generalised Constraints | 45 |
| 3.4 | Basis Functions | 51 |
| | 3.4.1 Nomenclature | 51 |
| | 3.4.2 Discrete Orthonormal Polynomials (DOP) | 56 |
| | 3.4.3 Derivatives of Discrete Orthonormal Polynomials | 59 |
| | 3.4.4 Local Approximation | 61 |
| | 3.4.5 Linear Differential Operator | 62 |
| | 3.4.6 Basis Function Approximation with Constraints | 64 |
| 3.5 | Model Based Reconstruction of Monitoring Data | 67 |
| | 3.5.1 Data Fusion | 69 |
| | 3.5.2 Long-Term Observations | 71 |

| | | |
|----------|---|------------|
| 4 | Future Urban Monitoring Infrastructure | 74 |
| 4.1 | Distributed Monitoring | 74 |
| 4.2 | The Celtic Plus ASUA Project | 75 |
| 4.2.1 | UrbMics in ASUA | 75 |
| 4.3 | Monitoring Devices for Challenging Environments | 76 |
| 4.4 | Cloud Systems in ASUA | 80 |
| 4.4.1 | The ASUA Urban Automation Reference Platform | 80 |
| 4.4.2 | UrbMics Centre | 82 |
| 4.5 | Local UrbMics Network | 82 |
| 4.5.1 | Handling of the Monitoring Sensor Data | 85 |
| 4.5.2 | Data and Metadata of Sensors | 86 |
| 4.5.3 | Setting Alarms in ASUA | 87 |
| 5 | Outlook and Conclusion | 88 |
| A | Review of Statistical Distributions | 92 |
| A.1 | Histograms | 92 |
| A.2 | Statistical parameters | 94 |
| A.3 | Cauchy-Lorentz Distribution | 96 |
| A.3.1 | Parameter estimation for Cauchy distribution | 97 |
| A.3.2 | Random number generation | 98 |
| B | List of Figures | 99 |
| C | Bibliography | 104 |

1 | Introduction

This PhD thesis addresses methods, algorithms and technologies that are suitable for future tasks of distributed and modern geo-monitoring. Geo-monitoring deals with the monitoring of natural and man-made objects to ensure the security of persons or infrastructure. Especially during construction works and renovations different sensors are mounted onto bridges, rails or buildings. Also during tunnel construction, especially in urban areas, the surroundings and the infrastructure there must be monitored.

To determine the deformation of a point on a surface or a tunnel wall, a 3D deformation measurement is normally carried out using a robotic total station. Other sensors are necessary for measurements below the surface. For example, extensometers are used to measure displacements in the longitudinal axis of a borehole [6]. Inclinometers allow the measurement of displacements perpendicular to the bore axis in which the sensor is mounted [7]. They measure the tilt (or slope) of the investigated object where the sensor is attached to. Currently, inclinometers are used in many structural and geo-mechanical monitoring systems, see Machan and Bennett [38] for a good overview. Further applications in the monitoring of rigid structures can be found in literature [22, 66, 72, 73].

In many measurement applications various different types of sensors are used. Thus, the data of the physically different measurement systems are merged into a combined solution using data fusion. This approach allows a more accurate and stable solution for a specific problem and also enables the detection of faulty sensors.

Geo-monitoring at a construction site extends over the period from a few months before the start of construction until some time after the construction work has been completed. Therefore, it is necessary that the used sensors provide stable and reliable values over their entire period of use. A suitable processing of the raw data provides more accurate data or allows the use of more cost-effective sensors.

The advances and developments in connected sensors and mobile devices also lead to a need for construction companies to access measurement results in real time via the Internet and to be able to react immediately in the event of an alarm. These emerging needs are changing the requirements for sensor technology, data transmission and data availability. The requirements for cloud-based, battery-powered measurement systems in challenging environments such as mining and tunnelling are even more

specialised than the requirements in traditional IoT applications.

An increasingly important role of future geo-monitoring solutions is their integration into larger urban monitoring solutions. The Smart City approach is a key enabler for new technologies, new urban services and digital economy, whereby many smart solutions of all sectors of society together make a smart city possible [67]. There are several examples available, where geo-monitoring applications are used in smart cities, e.g. smart construction sites [67] and Building Information Modeling (BIM) [41] where an autonomous data exchange during the construction process is done and meta data as well as dynamic sensor data is provided via a BIM interface [37]. This BIM framework is further extended to City Information Modeling [11, 71], where BIM is integrated into wider city planing and development.

The backend of the data exchange is managed in Urban Automation Networks (UAN), which act as central service for Information and Communication Technologies (ICT) to make the components and services of Smart Cities more interconnected, efficient and intelligent [24]. To cope with the amount of data and the processing of the data new strategies like open central data repositories are needed as well as the performance of available and emerging databases need to be researched [25].

Many of the currently existing geo-monitoring systems and sensors are stand-alone solutions or not even connected to a network. Thus, available sensors can often only be used for specific applications and can only be integrated into third-party systems at great expense.

Therefore, new sensors and devices should enable machine-to-machine (M2M) communication. Furthermore, these end devices should be easily configurable in order to be integratable into cloud-based monitoring systems.

1.1 Monitoring of Structure

Our modern civilisation relies on the safety and durability of our environment, hence in the past buildings and infrastructure were constructed and built to last for centuries; e.g. Hagia Sophia, in Istanbul, was built in 537 A.D. and after several renovations it is still in good condition and hosts nowadays a mosque after being a museum from 1935 to 2020. A newer, more technical, example is the London Underground, which opened its first line in 1863 with steam powered trains. The first electrified line followed in 1890. Due to the age of this tunnel system, this metro system is a good example for existing urban infrastructure that has to be monitored to ensure safe operation. Several guidelines for monitoring structures such as tunnels can be found in literature [18, 70].

The main objectives of in-situ monitoring of structures can be defined as: 1) control the deformation of the tunnel; 2) control the settlements on the surface; 3) measure the development of stress in the structural members; 4) indicate the progressive

deformation, which required immediate action to prevent collapse and 5) furnish evidence for insurance claims [70].

Various methods and sensors are available to fulfil these five monitoring objectives. The list of sensors ranges from extensometers, theodolites, accelerometers to inclinometers etc., but it is not limited to these sensor examples. Inclinometer sensors are handy to use and provide different possibilities for surveying land or buildings, especially for the detection of deformation of structures and movements of soil. The basic assumption for structural monitoring tasks with inclinometers is to monitor a real physical system, e.g. a bridge or railway tracks, whereby the observed system follows the laws of physics. When monitoring a larger structure, e.g. a bridge, multiple tilt sensors are needed for capturing the actual condition during observation.

Since any physical system abides by the law of physics it can be described using differential equations for models of the structure; both ordinary differential equations (ODE) and partial differential equations (PDE). Depending on the observed structure different types of sensors are used for monitoring and the size of area that is monitored determines the number of used sensors.

In some cases it is necessary to use different sensor systems to determine the deformation of a system. For example, in a subway tunnel it is not possible to perform continuous optical measurements due to subway trains, but inclination sensors on the tracks enable a continuous monitoring. Since the inclinometer sensors cannot detect horizontal displacement, optical measurements are performed in regular intervals. To combine the data of both sensor systems the demand for suitable data fusion algorithms is given. At over-constrained systems regularisation enables the detection of faulty sensors and a validation of the acquired sensor data.

Monitoring sensors are used for detecting deformation of an object for a limited period of time, e.g. during structural work on the engineering structure. The default procedure is to mount the sensors on the structure and take a *zero measurement* to gather a reference snapshot of the system where further reconstructions can be compared with. Before work on the observed object starts it is advantageous to monitor the system for a longer period of time to determine whether any environmental factors have influence on the structure, e.g. temperature, load, etc.

The physical structure abides by the laws of physics and thus the deformation is influenced by the design of the structure itself. Additionally, the structure has natural constraints that have to be considered in the solution, e.g. the horizontal position of pillars are considered stationary when measuring vertical displacements. This a-priory knowledge associated with these constraints can be utilised to implement a physics based regularisation. This results in an improved accuracy for the final result.

When appropriate models for a specific problem are set up, the system can be simulated prior to the real application to estimate, if the expected result meets the

expectations. In addition, the optimal sensors for each application can be selected with regard to accuracy, resolution and price. However, each sensor has his own characteristics and the precision of sensors can be improved by applying additional data processing like filtering. To find an algorithm to improve the accuracy of a sensor, a detailed sensor analysis is necessary. Chapter 2 of this thesis presents this analysis for the most commonly used high precision inclination sensor in the geotechnical environment.

1.2 Outline of the Thesis

The thesis is divided into five sections, with a separate section dedicated to each research focus of this thesis.

Detailed Analysis of Inclination Sensors

Section II deals with a detailed analysis of the most commonly used inclination sensors in geo-monitoring. The calculation of the deformation of a structure, which is monitored by inclination sensors, requires stable and highly precise sensors. A detailed characterisation of different inclination sensors is performed to improve the quality of the reconstruction and increase the estimation quality. Since statistical distributions play a major role in the analysis of sensors and the presence of sensor noise of Cauchy-Lorentzian type an additional section with a review of statistics is appended to this thesis.

Model Based Reconstruction

In Section III the theory of model based reconstruction for monitoring problems is introduced. Polynomials and basis functions with constraints are suitable to model structural problems. Solving the inverse problem enables the computation of the deformation of a structure from sensor data like inclination sensors. Optical 3D displacement measurements of control positions with a robotic total station provide reference data to estimate the quality of the reconstruction. Data fusion of inclination data and the data of optical reference measurements within this model based reconstruction improves the quality and reliability of the result significantly.

Future Urban Monitoring Infrastructure

Section VI presents the practical results and prototypes that were created for the Celtic-Plus project *Advanced Sensing for Urban Automation*¹ (ASUA) as part of this work. The Urban Automation Reference Platform, developed together with the ASUA project partners, is a framework that enables a generic integration of different heterogeneous sensor systems with the same priority in a horizontal manner. The specific prototype that has emerged from this work, a modular wireless monitoring system with cloud support for monitoring tasks in urban domains as well as the corresponding cloud infrastructure, is presented in detail. A robust design of the hardware is required, low power and stand-alone modes are implemented, and remote configuration updates via the cloud are possible.

The acquired and local processed sensor data is transmitted to the cloud based supervisory system as well as the public ASUA IoT cloud.

1.3 Original Work

Apart from the development of the geo-monitoring system, the interfaces to the cloud and the distributed system, this thesis contributes to the characterisation of the monitoring sensors and the implementation of standard reconstruction problems on distributed local monitoring devices. This includes:

1. The residual analysis of various inclination sensors and the interpretation of the observed results is presented. It is shown that some inclination sensors can be modelled more precisely by a Cauchy-Lorentz distribution than by a Gaussian. Sensors that follow a differential measurement principle contain several sensor elements. Typically, the same sensor gain is assumed for each sensor element. A Singular Value Decomposition (SVD) is used to demonstrate, that this gain is not identical in general. A SVD is suitable to determine this difference in the gain and allows a more accurate estimation of the expectation value of a sample.
2. The specific mathematical cases that regularly occur in geo-monitoring are introduced and the corresponding numerical approaches for solving them are presented. Constrained polynomials as well as constrained basis functions are suitable for model based reconstruction of deformation of rigid structures.
3. Robust data acquisition systems were developed and built for use in geo-monitoring tasks. These devices have sufficient computing power to enable local data processing, e.g. model based reconstruction. The nodes organise

¹The Celtic-Plus Project *Advanced Sensing for Urban Monitoring* (ASUA, Project-ID: C2013/2-2) was an European research project between 2015 and 2017 in which the Chair of Automation / University of Leoben participated and parts of the here presented work arose from research for this project.

their own meshed network, with a gateway serving as a connection to the cloud. The devices have a black out mode, where local data storage, local data processing, event detection and alarm triggering are performed.

4. The *Urban Automation Reference Platform* was developed together with an international research group in the ASUA Project. The framework for urban automation follows a generic approach enabling the integration of different heterogeneous sensor systems and offers possibilities for finding and processing geospatial data as well as rule processing and alarm triggering.
5. Model based reconstruction was implemented on a Linux-based embedded system. Inclination sensors used for geo-monitoring tasks served as a data source. The locally reconstructed data is transferred to a cloud, such as the "Urban Automation Reference Platform", where the data is used for event detection and alarm triggering.

1.4 List of Publications

Conference Papers

1. *Non-Destructive Thermography Analysis of Impact Damage on Large-Scale CFRP Automotive Parts* [39]
Journal article in *Materials 2013*
A. Maier, R. Schmidt, B. Oswald-Tranta and R. Schledjewski
2. *Crack Depth Determination with Inductive Thermography* [51]
Conference proceedings at *Proceedings of SPIE - The International Society for Optical Engineering 2015*
B. Oswald-Tranta and R. Schmidt
3. *A Smart Multi-Sensor System for Structural Monitoring* [62]
Conference paper and oral presentation at *Geomonitring 2016* in Braunschweig, Germany:
R. Schmidt, P. O’Leary, M. Harker, K. Chmelina and J. Golser
4. *Precision Inclinometer Measurement System with a Wireless Gateway* [61]
Conference paper and oral presentation at *2016 IEEE International Instrumentation and Measurement Technology Conference (I2MTC)* in Taipei, Taiwan:
R. Schmidt, P. O’Leary and M. Harker
5. *Comparison of Samples with Flat Bottom Holes and with Hidden Occlusions Using Flash Thermography* [52]
Conference paper at *2016 Quantitative InfraRed Thermography*
B. Oswald-Tranta, R. Schmidt and T. Grandl
6. *MEMS Based Inclinometers: Noise Characteristics and Suitable Signal Processing* [63]
Conference paper and oral presentation at *2017 IEEE International Instrumentation and Measurement Technology Conference (I2MTC)* in Turin, Italy:
R. Schmidt, P. O’Leary, R. Ritt and M. Harker
7. *Thermographic Investigations of Metal Inclusions in 3D Printed Samples* [53]
Conference paper at *SPIE - The International Society for Optical Engineering 2017*
B. Oswald-Tranta, R. Schmidt and C. Tuschl

2 | Analysis of Inclination Sensing Elements

Inclination sensors form the basis for deformation measurements right-angled to a measurement axis, e.g. a deformation measurement of a borehole. The quality of the sensor data affects the overall measurement result, therefore a good knowledge about the sensor and the corresponding data processing is crucial. Since statistical distributions play a key role in the analysis of the sensors used, a summary of the most important properties of the occurring distributions has been prepared in Appendix A.

In this thesis micro-electro-mechanical systems (MEMS) inclination sensors from *Murata Manufacturing Co., Ltd.* are used to determine the tilt of specific points [43]. The sensors can be classified according to different properties of the sensor. For monitoring applications the resolution and accuracy are the most important parameters. The stability of inclination sensors over a long time period and a wide temperature range is also a basic requirement. For wireless sensor nodes the supply voltage and a low power consumption are also important parameters.

2.1 MEMS technology for inclination sensors

Inclination sensors, or tilt sensors, are used to measure inclination of an object by measuring the force of gravity. In the past analogue devices with weights or liquids were used, nowadays MEMS are used to measure inclination. These MEMS sensors are manufactured using nanotechnology [69].

There are multiple physical principles for measuring inclination in MEMS sensors such as using the piezo-electric effect, where the acceleration stresses a crystal structure that yields a voltage change indicating the inclination. The majority of the MEMS inclination sensors detect changes of capacity when a proof mass is moved by the acceleration. The proof mass, that is fixed between springs, can move in the sensor. The design of the proof mass includes plates that move between two fixed outer plates. Between the two outer plates and the moving plate are two electromagnetic fields that change when the beam moves. The capacitance is measured and the

acceleration and inclination derived from the changing capacitance. Figure 2.1 shows a simplified model of the MEMS sensor.

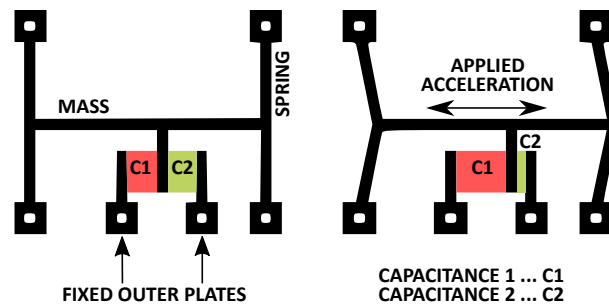


Fig. 2.1 Simplified MEMS model: The sprung proof mass is moved by the acceleration which causes the change of the two capacitances C1 and C2. This is used to derive the acceleration and suitable signal conditioning and filtering yields the inclination. MEMS sensors use multiple parallel-plate capacitors on one sensing element.

Another approach for MEMS sensors is to use the pull-in effect to measure the inclination. Figure 2.2 shows a simplified model for the electromechanical system consisting of two electrodes, whereby one electrode is connected to a spring and has the possibility to move and the other one is fixed [57].

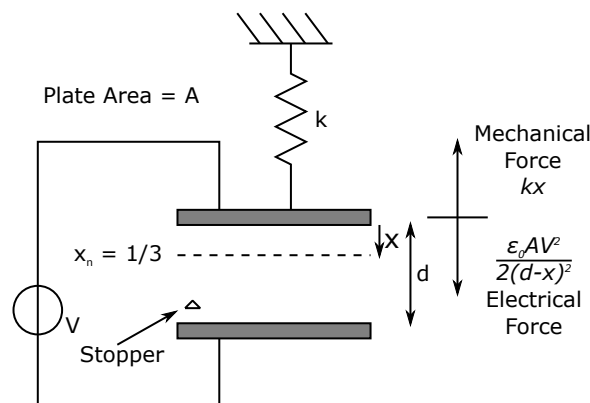


Fig. 2.2 Sketch of a simplified basic electromechanical system of a pull-in MEMS [57].

If a voltage is applied the electric force of the resulting electrical fields pulls the movable plate to the other one. The energy of the electric field and the energy of the mechanical springs are in a stable position for low voltages. If the voltage exceeds a certain voltage, the pull-in voltage V_{pi} the systems gets unstable and the proof mass hits a stopper. This V_{pi} is used to derive the corresponding acceleration or inclination from the deformation of the system. In MEMS sensors of this type multiple fingers and parallel plate capacitors are implemented for gathering a higher sensitivity [57]. Figure 2.3 shows a Scanning Electron Microscope (SEM) image of a MEMS sensor with parallel-plate capacitors and the fingers on the moving middle part.

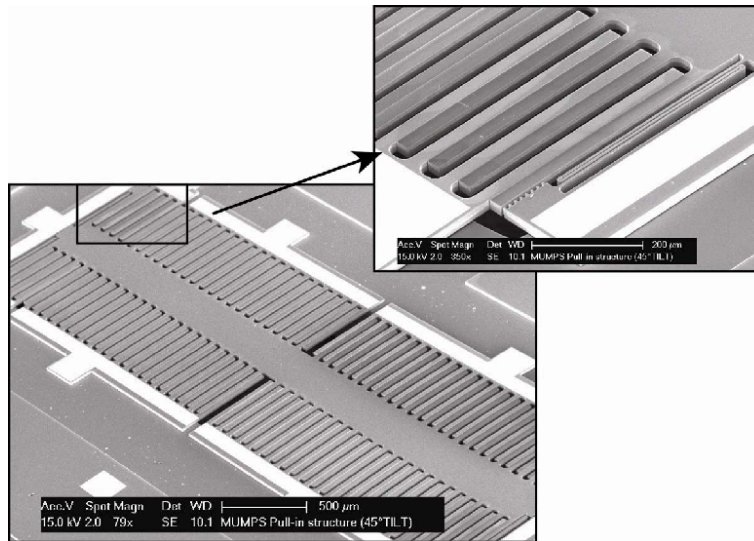


Fig. 2.3 SEM image of a MEMS sensor for measuring acceleration and inclination. The proof mass is placed on the back-side of the structure [9].

2.2 Comparison of Different Inclination Sensors

In this section an overview of the different inclination sensors is given and a detailed sensor characterisation is presented. The Murata SCA103T receives the most attention in this thesis, as it is currently used for many geo-monitoring tasks due to its accuracy and stability.

Table 2.1 presents the different inclination sensors (and accelerometers) presented in this chapter.

| Model | Nr. Axis | Range [°] | ADC Res. | Sensitivity | Supply Voltage |
|--------------------|----------|---------------------------------|----------|----------------------|----------------|
| SCA830-D07 | 1 | $\pm 90^\circ$ ($\pm 1g$) | 16 bit | $0.00175^\circ/LSB$ | 3.3 V |
| SCA103T-D04 (int.) | 1 | $\pm 15^\circ$ ($\pm 0.26g$) | 12 bit | $0.009^\circ/LSB$ | 5 V |
| SCA103T-D04 (ext.) | 1 | $\pm 7.5^\circ$ ($\pm 0.13g$) | 24 bit | $8.9e - 7^\circ/LSB$ | 24 V |

Tab. 2.1 Comparison of different inclination sensors.

Figure 2.4 depicts the resolution over the range of the single sensors. The SCA103T with the external 24bit ADC provides a very high sensitivity, but at cost of a supply voltage of 24 V. Additionally, the solution with an external data processing unit is quite expensive compared to the sensor's internal processing circuit.

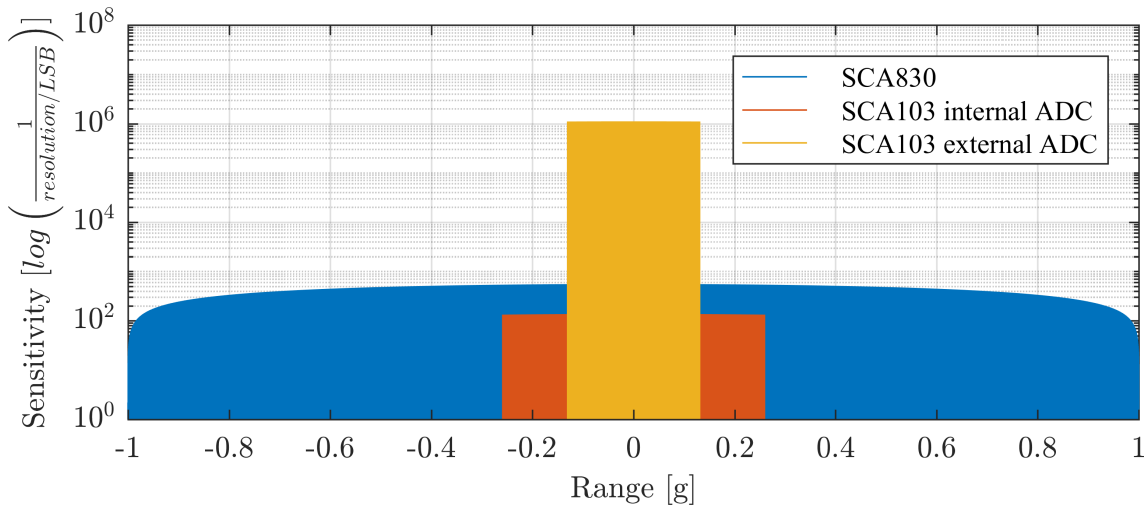


Fig. 2.4 Comparison of range and sensitivity of different inclination sensors

2.3 SCA103T-D04 Inclination Sensor

The SCA103T inclination sensor was Murata's most advanced high precision inclinometer sensor available for testing during the phase of characterising these sensors. The sensor itself has two individual sensing elements that are oriented in the mutually opposite direction. The SCA103T provides both, a digital and an analogue output, where the conditioned and filtered signal of the two internal MEMS sensing elements is available. To benefit from the high precision of the sensor the analogue output combined with an external high resolution ADC and suitable signal processing has to be used. The schematic of the SCA103T is shown in Figure 2.5 [63].

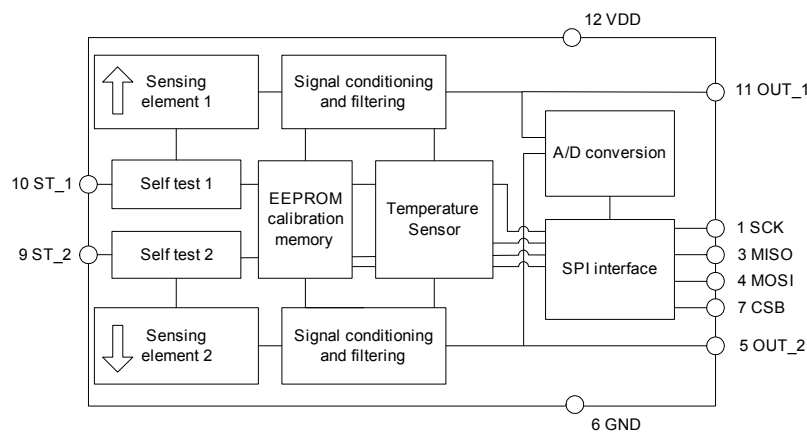


Fig. 2.5 Schematic of the SCA103T inclinometer, [43] © Murata

For characterisation of the sensors, several sensors with suitable data acquisition electronics with external analogue digital converter (ADC) were provided from Geodata. This acquisition electronic board provides, beside signal filtering, a

RS485 bus interface to allow reliable data acquisition over long distances in rough environments. The inclination sensors are protected by different stable steel covers allowing different mounting options for individual applications. Figure 2.6 shows the acquisition board and two inclination sensors in metal cylinders [63].

On the acquisition board an ADC acquires the sensor data from the analogue output of the sensors, additionally a low pass filter is applied internally to the acquired data. Via the RS485 bus the temperature of the acquisition board is provided, however the temperature of the sensors, which would be required for additional temperature compensation, is not provided [63].

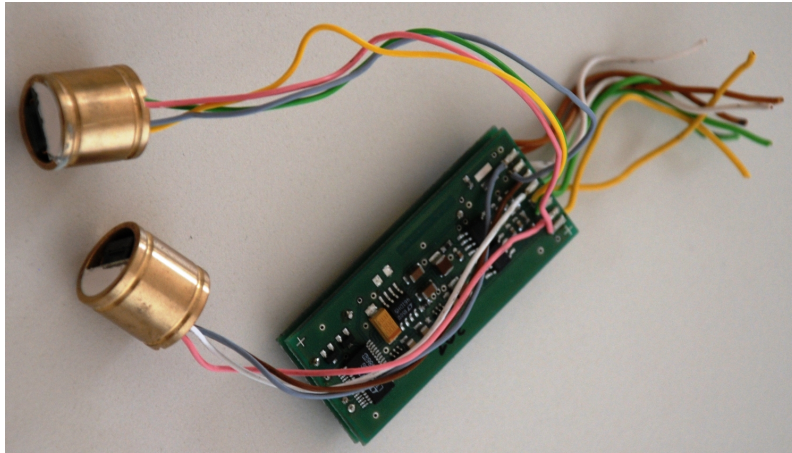


Fig. 2.6 Photograph of a pair of inclinometers connected to the data acquisition electronics. Each metal cylinder contains one MEMS sensor. In the implementation shown the Sensors are connected using the analogue interfaces, i.e. using the signals VDD, GND, OUT_1 and OUT_2 [63] © 2017 IEEE.

The Murata SCA103T inclination sensor is, beside the analogue sensor output, equipped with an internal ADC. The ADC has a resolution of 12 *bit* and a range of $\pm 15^\circ$ ($\pm 0.26 g$). The data is accessible via a digital SPI [32] interface. In order to operate the sensor, the chip has to be powered with a power supply of 5 V. Since the SCA103T sensor operates according to a differential measurement principle, the raw data of both sensing elements, RDAX and RDAY, can be accessed via the SPI interface with a maximum frequency of 5300 samples per sec/channel. Also the temperature of the sensor can be accessed via SPI [43].

According to the manufacturers manual [43] the inclination in degrees can be computed by,

$$\alpha[mg] = \frac{D_{out}[LSB] - D_{out@0^\circ}[LSB]}{Sens[LSB/g]} \quad (2.1)$$

whereby D_{out} is defined as,

$$D_{out} = RDAX - RDAY. \quad (2.2)$$

Commonly inclination or acceleration measurements from a sensor are provided in g or mg . The conversion from mg to degree is computed as follows,

$$\alpha[^\circ] = \arcsin(\alpha[mg]). \quad (2.3)$$

The temperature compensation for the internal inclination measurement is done directly on the SCA103T, for external temperature compensation for an analogue measurement (external ADC), the temperature data has to be acquired via the SPI interface. The accuracy of the internal temperature sensing element is specified in the datasheet with $\pm 1^\circ\text{C}$ [63].

The two sensing elements of the SCA103T inclination sensor are arranged in the mutually opposite direction. As described in section 2.1 these sensors are basically accelerometers, where signal conditioning and filtering is applied to the signal of each sensing element to optimize the signal for measuring inclination. The signals of the two sensing elements are here defined as $x(t)$ and $y(t)$ and consist of following components:

$$x(t) = g + i(t) + v(t) + n_x(t), \quad (2.4)$$

$$y(t) = g - i(t) + v(t) + n_y(t) \quad (2.5)$$

where g is due to gravitation, $i(t)$ is the inclination as a function of time, $v(t)$ is the component due to ambient vibrational noise, $n_x(t)$ and $n_y(t)$ are the individual noise components of each sensor. Defining the differential $d_m(t)$ and sum $s_m(t)$ measurement signals as:

$$d_m(t) = x(t) - y(t) = 2i(t) + n_x(t) - n_y(t), \quad (2.6)$$

$$s_m(t) = x(t) + y(t) = 2g + 2v(t) + n_x(t) + n_y(t). \quad (2.7)$$

Consequently, it is possible to determine both the extraneous vibrations and inclinations from the sensor data.

2.4 Characterisation of the SCA103T

To characterize the inclination sensor under known conditions a laboratory setup was designed. This enables the investigation of the behaviour and stability of the sensors at given inclination angles and also the measurement of multiple sensors in parallel under same conditions, see Figure 2.7. The sensor adapter allows the mounting of individual manufactured stable sensor carriers. Figure 2.7 shows the laboratory setup, the pointer and scale and the sensor adapter with a carrier and the mounted SCA103T sensor in analogue and digital configuration [63].

This setup includes a rotatable body, a sensor adapter and a pointer that allows the accurate adjustment of the desired angle. The angle can be set manually via the pointer and scale by a resolution of 0.25° over a range of $\pm 25^\circ$. The accuracy of $\epsilon = 1$ was considered as sufficient, since the goal of the measurement was to

characterize the noise at different deflections and not to determine the absolute accuracy of the sensors.

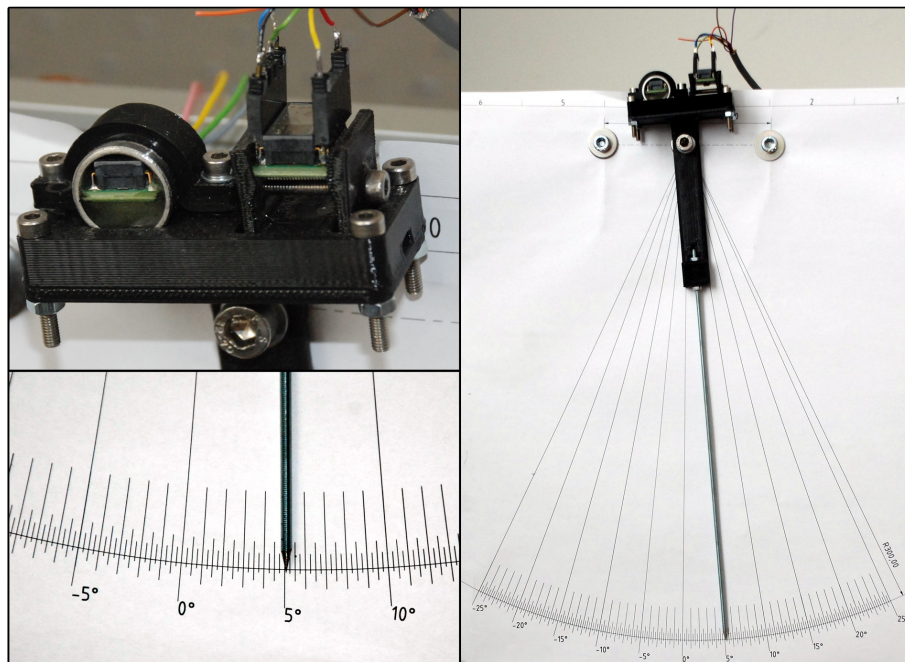


Fig. 2.7 Laboratory set up to measure the stability of the inclinometer measurements. Left top: detail view of the two sensors, the right one with the SPI and the left one with analogue interface and additional data acquisition electronics included. Left bottom: detail view of the the measurement scale. Right: overall view of the complete laboratory set up [63] © 2017 IEEE.

The setup enabled the acquisition of various data sets for characterising the sensors under different deflections. Figure 2.8 shows two data sets of the SCA103T inclinometer with different deflections, the blue line from the analogue high precision signal, the red line represents the raw SPI data. The vertical green bars indicate the segmentation of the data for statistical evaluation [63].

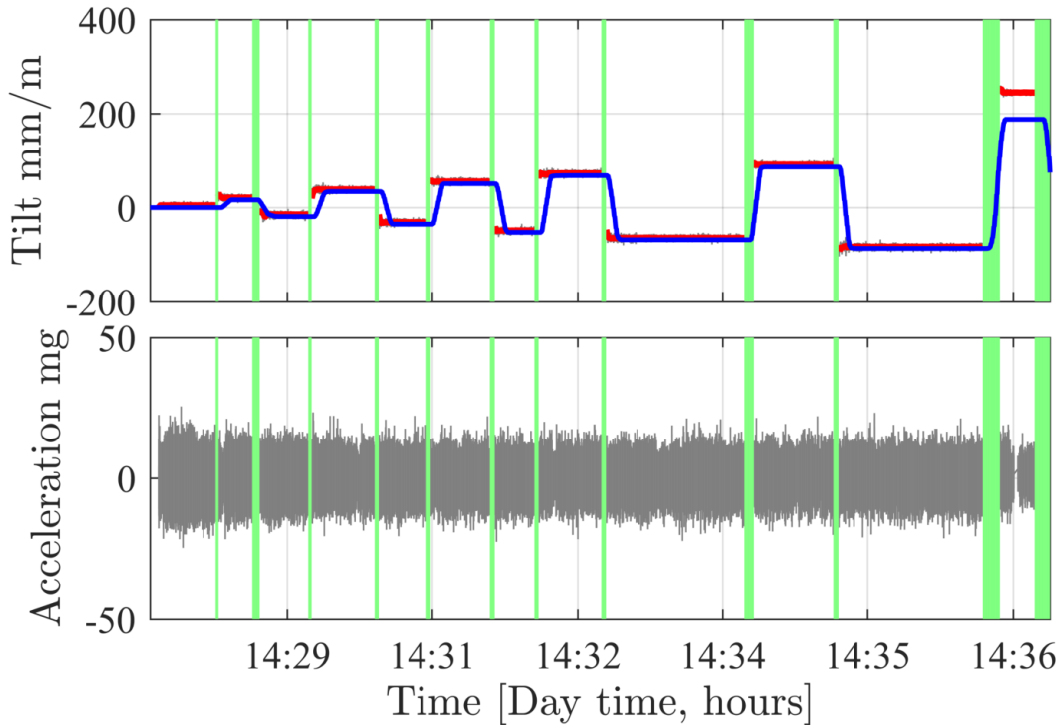


Fig. 2.8 Laboratory measurement to characterize the sensor performance: Top: The tilt measured in [mm/m] for various angles, (blue) precision analogue measurement, (gray) raw SPI data and (red) filtered SPI data 1 Hz bandwidth. The vertical green bars indicate the segmentation of the data for statistical evaluation. Bottom: the measured accelerations [63] © 2017 IEEE.

A statistical evaluation of the acceleration data a yielded a virtually perfect Gaussian distribution with $\mu \approx 0$ and $\sigma_a = 5.06 \text{ mg} \pm 14 \text{ }\mu\text{g}$ with 95% certainty, when sampled at $f_s = 452 \text{ Hz}$ and using no averaging. The Gaussian nature of the noise in the acceleration data permits the use of filtering, e.g. sliding average, to obtain smaller bandwidth and lower noise power. The noise power scales linearly with the reduction in bandwidth. Consequently, at the bandwidth $f_{bw,a} = 0.0885 \text{ Hz}$, as used for the analogue data we obtain an effective noise-floor of $\sigma_{nfa} = 36 \text{ }\mu\text{g}$ [63].

The histogram for the acquired tilt signal is shown in Fig. 2.9. It reveals that the statistics for the tilt data are better described by a three term Cauchy-Lorentz distribution, that is defined as:

$$f(x; x_m, \gamma, I) = I \left\{ \frac{\gamma^2}{(x - x_m)^2 + \gamma^2} \right\}. \quad (2.8)$$

than a Gaussian. The parameter values obtained for the tilt data are: the median $x_m = 60 \text{ }\mu\text{m/m}$, $\gamma = 1.2883 \text{ mm/m}$ and $I = 0.219$. More details on estimating parameters for a Cauchy-Lorentz distribution can be found in [19]. It is important to note, that simple computing a sliding average will not necessarily yield a value with a narrower confidence interval. There are no central moments existing for the Cauchy-Lorentz distribution nor any other definition for a mean, therefore no mean

value exists and can be computed [19]. It is possible to compute the medians or the truncated mean with a 24 % truncation interval (see [19]), if smaller confidence intervals are required [63].

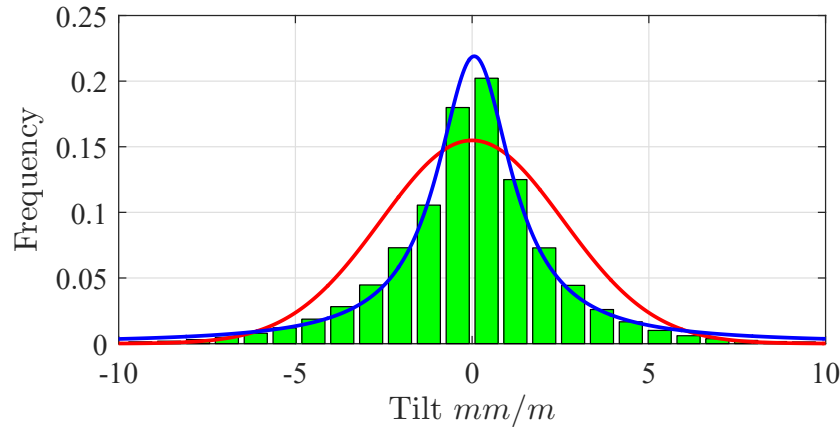


Fig. 2.9 Histogram of the tilt measurements together with the maximum Likelihood Gaussian (red) $\sigma_t = 2.5765 \text{ mm/m} \pm 7.2 \mu\text{m/m}$ with 95 % certainty and the maximum entropy Cauchy-Lorentz distribution (blue) with the parameters $x_m = 60 \mu\text{m/m}$, $\gamma = 1.2883 \text{ mm/m}$ and $I = 0.219$, [63] © 2017 IEEE.

For further investigations a data set for the SCA103T sensor was acquired. The SCA103T was positioned at $m = 11$ different deflections and a total of $n = 183\,311$ samples were acquired. The raw data¹ and a filtered result are shown in Fig. 2.10 [63].

¹A brief note on nomenclature: All data presented in the histograms have integer values corresponding to the digital reading of the individual sensor. Consequently, the width of the distributions are all in LSB.

PDF refers to probability distribution function and CDF to cumulative distribution function. The notation $p(\alpha)$ refers to the probability of the variable α having a given value. The symbol σ_α refers to the standard deviation of α and γ_α is the half-width at half-maximum value of the Cauchy Lorentz distribution for α .

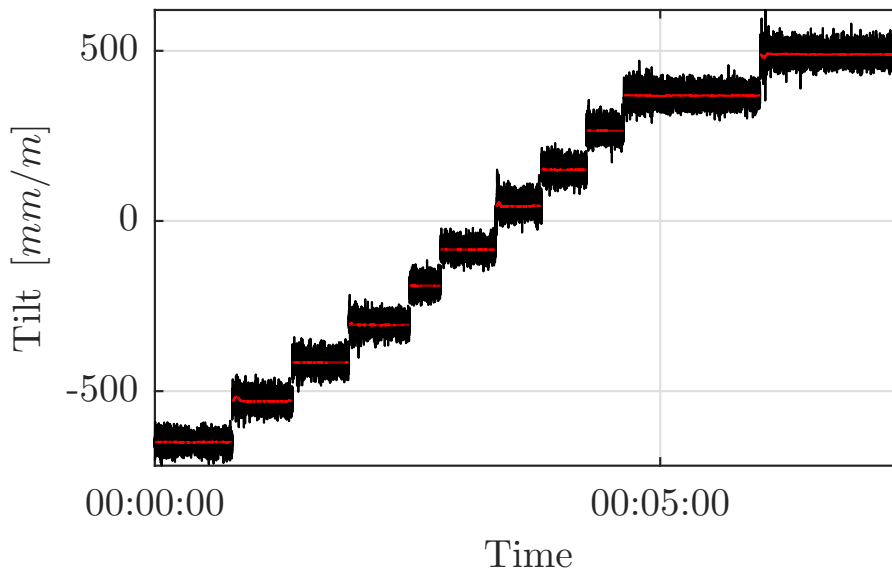


Fig. 2.10 The signal acquired from the SCA103T sensor after evaluation to *tilt*: (black) signal prior to filtering and (red) after filtering. A total of $n = 183\,311$ samples are used for the ensuing statistical analysis, [63] © 2017 IEEE.

The histograms for each of the $m = 11$ segments together with Gaussian and Cauchy-Lorentz distribution approximations are shown in Fig. 2.11 and the numerical values for the distribution parameters are given in Table 2.2. The χ^2 test for the Cauchy-Lorentz distribution in each of the $n = 11$ segments is an order of magnitude better than the corresponding Gaussian approximation; this is consistent with the visual inspection. These results justify the further and more detailed investigation of the nature of the noise in the system. Furthermore, the data from the segments show that the distribution width γ is independent of the specific inclination x_0 ; consequently, we may conclude that the distribution of the noise is independent of the deflection angle.

2.4.1 Histograms and Distributions for $x(t)$ and $y(t)$

Given the fact that there is no correlation between x_0 and γ , it is permissible to concatenate the median free data from each segment to obtain a larger sample size for the determination of the noise characteristics. This has been performed for the signals $x(t)$ and $y(t)$; their respective histograms and PDFs are shown in Fig. 2.12, while the deviation from a Gaussian CDF is given in Fig. 2.13. Clearly, the signals $x(t)$ and $y(t)$ are subject to Gaussian noise. It is important to note that $\sigma_x = 17.4$ and $\sigma_y = 19.2$ yield different values indicating that the sensor channels may have different gains with respect to ambient vibrational noise [63].

Now proceeding to the computation of the statistics for $d_m(t)$ and $s_m(t)$: the respective histograms and Gaussian models are shown in Fig. 2.14. In addition, a Cauchy-Lorentz PDF was calculated for the signal $d_m(t)$. The fact that $d_m(t)$ has

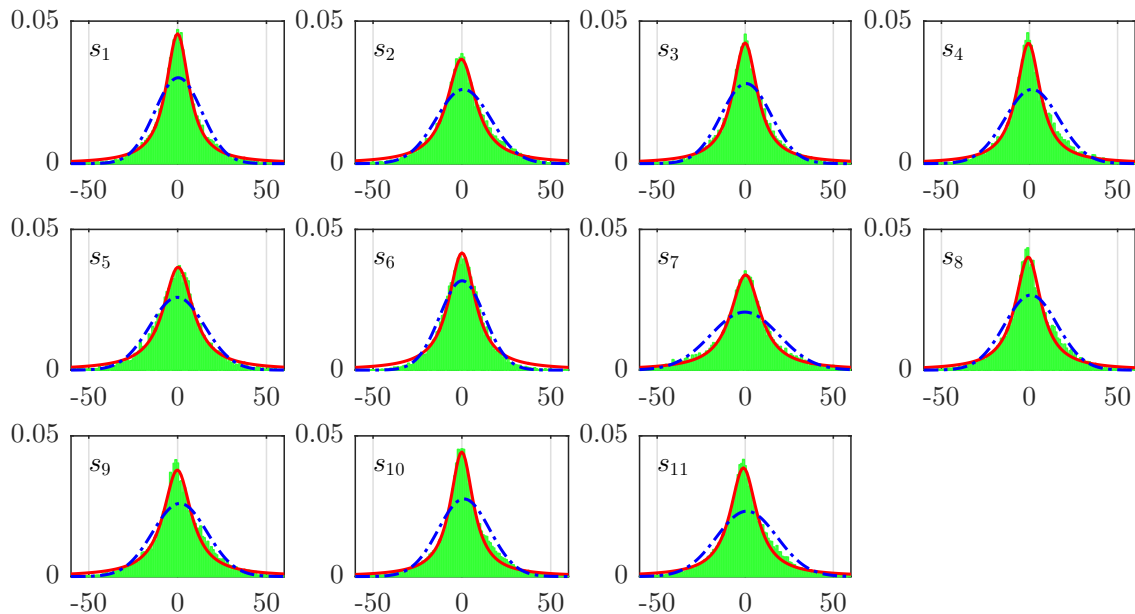


Fig. 2.11 Histogram for $x - y$ in each of the segments $i \in 1 \dots 11$ denoted by s_i , as shown in Fig. 2.10. The PDF for the Cauchy and Gaussian distributions are shown in red and blue respectively. The corresponding coefficients for the distributions are given in Table 2.2. The histograms have been centered around the median value of each segment, this simplifies the comparison of the results in each segment, [63] © 2017 IEEE.

| | n | x_o | γ_{x-y} | I_o | χ_C^2 | μ | σ | χ_G^2 |
|----------|-------|-------|----------------|-------|------------|---------|----------|------------|
| S_1 | 19126 | -650 | 7.89 | 4.56 | 1.42 | -649.65 | 13.24 | 20.21 |
| S_2 | 14648 | -529 | 10.00 | 3.67 | 2.07 | -528.10 | 15.31 | 12.00 |
| S_3 | 13812 | -416 | 8.51 | 4.23 | 1.76 | -415.48 | 14.20 | 18.63 |
| S_4 | 14755 | -305 | 8.27 | 4.23 | 2.68 | -303.60 | 15.32 | 25.73 |
| S_5 | 7789 | -191 | 10.21 | 3.66 | 2.35 | -191.20 | 15.43 | 11.94 |
| S_6 | 15155 | -84 | 9.18 | 4.16 | 3.11 | -83.86 | 12.57 | 7.79 |
| S_7 | 11265 | 43 | 10.35 | 3.39 | 1.21 | 42.74 | 19.35 | 21.33 |
| S_8 | 11166 | 151 | 8.91 | 4.02 | 2.94 | 151.76 | 14.96 | 18.90 |
| S_9 | 9347 | 265 | 9.54 | 3.79 | 3.15 | 266.25 | 15.35 | 15.72 |
| S_{10} | 32523 | 368 | 7.89 | 4.43 | 2.24 | 369.18 | 14.46 | 25.01 |
| S_{11} | 33725 | 490 | 9.17 | 3.86 | 2.00 | 490.90 | 17.17 | 24.14 |

Tab. 2.2 Statistics for each of the $n = 11$ segments, as shown in Fig. 2.10. Whereby: n is the number of samples in the segment, x_o , γ and I_o (scaled by $\times 100$) are the parameters of the Cauchy-Lorentz distribution, χ_C^2 for its PDF (scaled by $\times 1E4$), μ and σ as the coefficients for the Gaussian and χ_G^2 for the PDF (scaled by $\times 1E4$), [63] © 2017 IEEE.

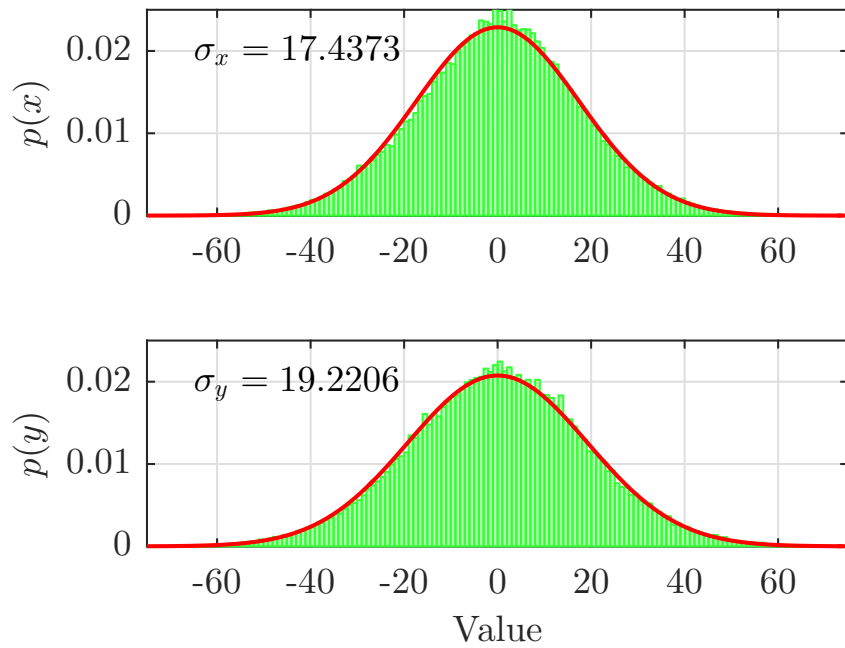


Fig. 2.12 Histogram of the values $x(t)$ and $y(t)$ with their corresponding Gaussian approximations with respective standard deviations, [63] © 2017 IEEE.

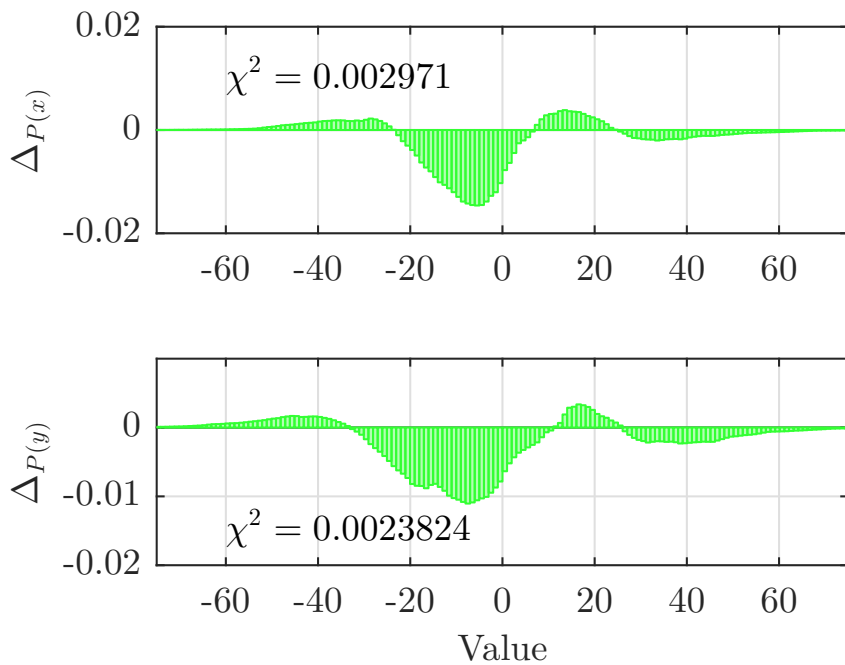


Fig. 2.13 Deviation of the cumulative distribution functions $P(x)$ and $P(y)$ from their ideal Gaussian models and the respective χ^2 values, [63] © 2017 IEEE.

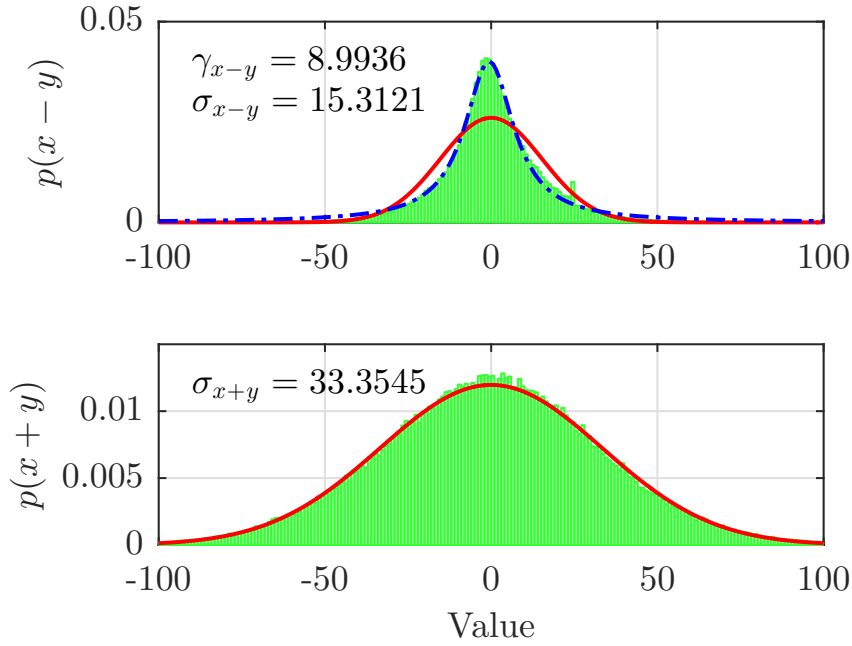


Fig. 2.14 Histogram of the values $p(x-y)$ and $p(x+y)$ with Gaussian (red) approximations. Additionally for $p(x-y)$ a Cauchy-Lorentz (blue) distribution has been approximated, [63] © 2017 IEEE.

Cauchy-Lorentz distribution implies that the perturbations of $x(t)$ and $y(t)$ must be correlated, since the difference of two Gaussians is also a Gaussian if the signals are not correlated. Furthermore, given $\sigma_x = 17.4$ and $\sigma_y = 19.2$ we would expect $\sigma_{x+y} \approx 25.91$; however, we observe $\sigma_{x+y} \approx 33.35$, obviously ignoring the relative gains of the sensor chains is degrading the quality of the result [63].

2.4.2 Correlation in the Perturbations of $x(t)$ and $y(t)$

To investigate the correlations in the perturbations of $x(t)$ and $y(t)$ a bivariate histogram has been computed, see Fig. 2.15. The correlation between the signals is clearly visible. The orientation of the dominant axis is not at 45° , a further indication that the sensor chains have differing gains. If the gain of the sensor chains were equal the dominant axis would be at 45° [63].

Singular value decomposition (SVD) is now used to determine the dominant axes and the distributions of the data with respect to these axes. Defining the matrix $D \triangleq [\mathbf{x}, \mathbf{y}]$ where \mathbf{x} is the column vector of the values of $x(t)$ (similarly for \mathbf{y} and $y(t)$). The SVD for a matrix D is defined as,

$$D = USV^T. \quad (2.9)$$

The matrix V forms an ortho-normal vector basis set for the span $\{D\}$, in the 2D case this corresponds to a rotation matrix from which we can determine the orientation of the major and minor axes. S is a diagonal matrix containing the singular values,

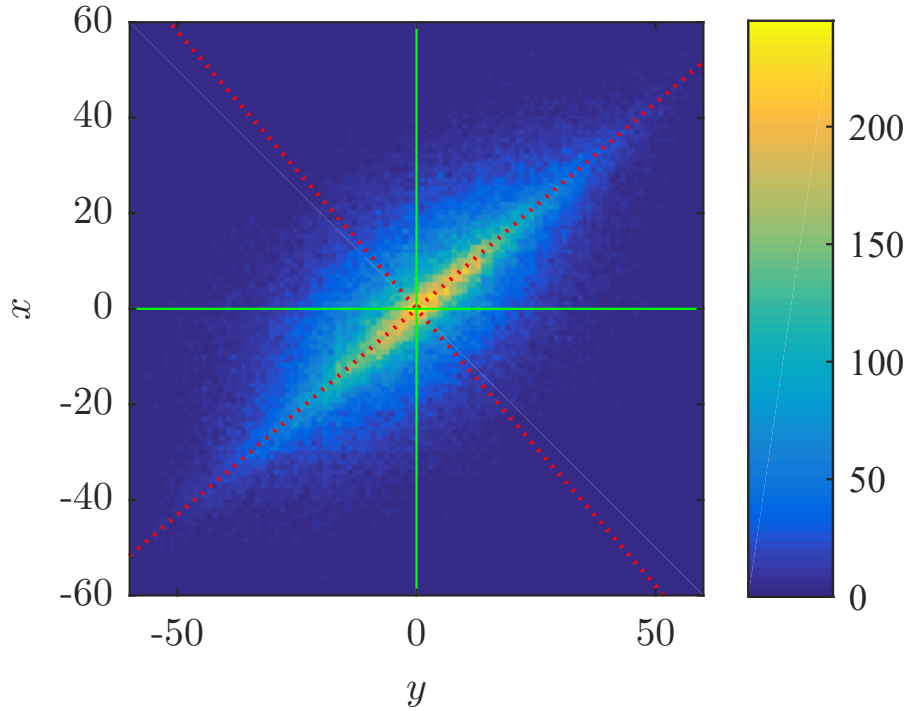


Fig. 2.15 Bivariate histogram for $x(t)$ and $y(t)$, the color indicates the frequency and is proportional to $p(x, y)$, [63] © 2017 IEEE.

i.e., the 2-norm distance of the points in \mathbf{D} to the vector basis set. \mathbf{U} is the scale free orthogonal projection of \mathbf{D} onto \mathbf{V} [63]. Consequently, we now obtain,

$$d_{SVD} = \mathbf{U}(:, 1) \mathbf{S}(1, 1) \quad (2.10)$$

$$s_{SVD} = \mathbf{U}(:, 2) \mathbf{S}(2, 2) \quad (2.11)$$

as orthogonalised estimates for d_m and s_m . The matrix \mathbf{V} has the values,

$$\mathbf{V} = \begin{bmatrix} 0.6530 & 0.7574 \\ 0.7574 & -0.6530 \end{bmatrix}. \quad (2.12)$$

corresponding to the angle $\phi = 40.77^\circ$ and a relative gain for the sensors of $g_r = 0.86$. The histograms and respective probability distribution functions for d_{SVD} and s_{SVD} are shown in Figure 2.16 [63]. Note: the observed standard deviation $\sigma_s = 23.64$ now corresponds closely to the predicted value, if the relative gain g_r is taken into account,

$$\sigma = \sqrt{\sigma_x^2 + (g_r \sigma_y)^2} = 24.01. \quad (2.13)$$

This indicates that the application of SVD has performed the correct orthogonalisation of the signals $x(t)$ and $y(t)$. Furthermore, the γ value for the Cauchy-Lorentz distribution has also been reduced. These results indicate that both vibration and inclination can be measured with a better confidence interval when orthogonalisation is applied [63].

The results of computing γ_{x-y} and γ_d after applying orthogonalisation to each segment of the data from Fig. 2.10 are shown in Table 2.3. A mean reduction in γ of $r_\gamma \approx 0.66$ has been achieved [63].

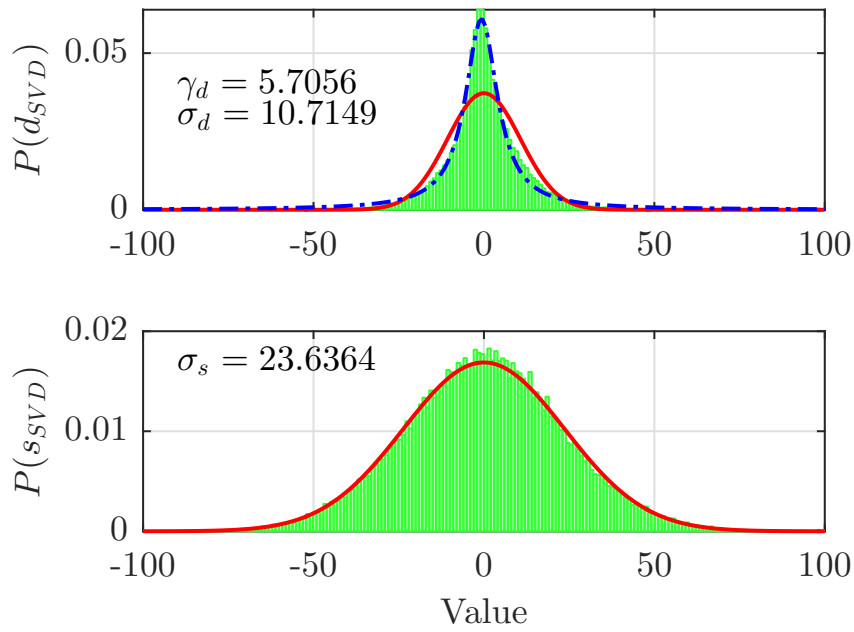


Fig. 2.16 Histograms for the orthogonalised values d_{SVD} and s_{SVD} together with the Gaussian (red) and Cauchy-Lorentz (blue) PDF, [63] © 2017 IEEE.

| | γ_{x-y} | γ_d | r |
|----------|----------------|------------|------|
| S_1 | 7.89 | 5.01 | 0.63 |
| S_2 | 10.00 | 6.54 | 0.65 |
| S_3 | 8.51 | 5.47 | 0.64 |
| S_4 | 8.27 | 5.27 | 0.64 |
| S_5 | 10.21 | 6.97 | 0.68 |
| S_6 | 9.18 | 5.45 | 0.59 |
| S_7 | 10.35 | 6.94 | 0.67 |
| S_8 | 8.91 | 5.86 | 0.66 |
| S_9 | 9.54 | 6.42 | 0.67 |
| S_{10} | 7.89 | 5.09 | 0.64 |
| S_{11} | 9.17 | 6.09 | 0.66 |

Tab. 2.3 The results for γ_{x-y} and γ_d obtained after applying orthogonalisation to each segment of the data shown in Figure 2.10. A mean reduction in γ of $r_\gamma = 0.66$ has been achieved, [63] © 2017 IEEE.

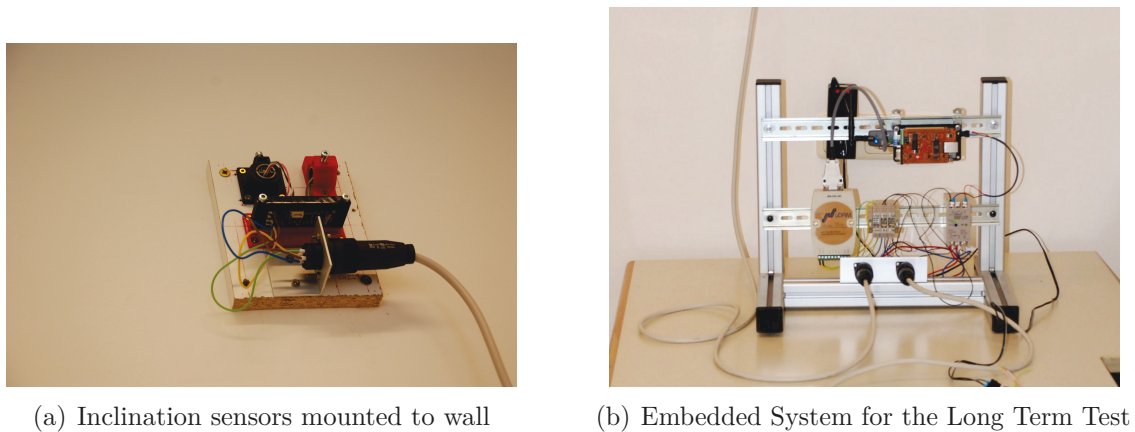


Fig. 2.17 Long Term Test stand in laboratory

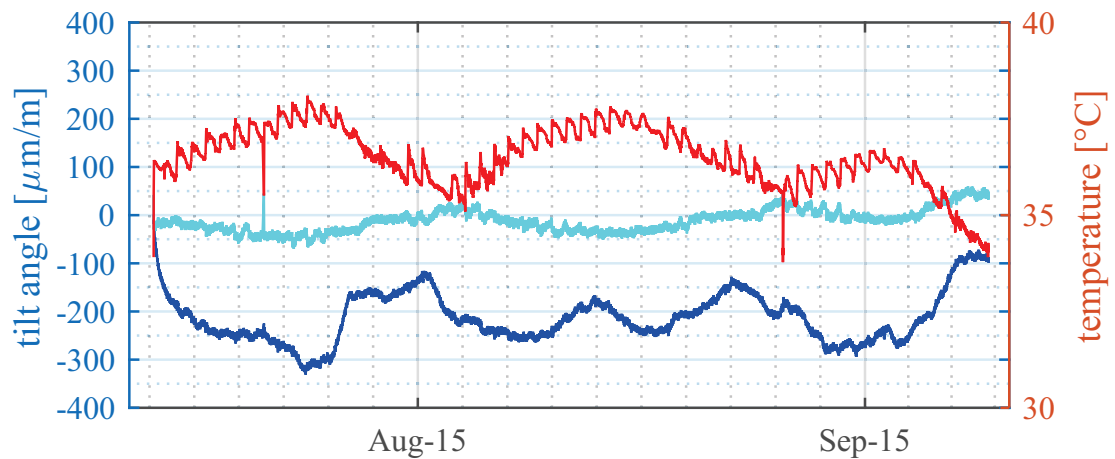


Fig. 2.18 Graph of the data logged from two inclinometers measuring in mutually orthogonal directions. This data was acquired with a measurement interval $t_s = 5$ s: tilt of sensor I_1 (blue), tilt of sensor I_2 (cyan) and temperature T (red). There are approximately $n = 10^5$ samples, [63] © 2017 IEEE.

2.5 Long-term Laboratory Measurement

To determine the long term stability of the analogue tilt sensor and its temperature sensitivity a laboratory set-up was made. Two inclination sensors, arranged in a mutually orthogonal manner, were mounted to a wall over a period of 58 days. The logged data, acquired with the sampling interval $t_s = 5$ s, is shown in Fig. 2.18 [63].

The co-variance matrix Λ_{T,I_1,I_2} for temperature T , tilt I_1 and I_2 is,

$$\Lambda_{T,I_1,I_2} = \begin{bmatrix} 0.42 & -10.72 & -1.43 \\ -10.72 & 309.10 & 34.66 \\ -1.43 & 34.66 & 610.91 \end{bmatrix}. \quad (2.14)$$

This indicates a temperature sensitivity $s_t = -10.72 \frac{\mu\text{m}}{\text{dC}}$ for I_2 ; however, some

care is required during interpretation since there would appear to be some additional periodic influence on the I_1 . A linear graphical estimate of the correlation is shown in Figure 2.19, this yielded the result $s_l = -25.53 \frac{\mu\text{m}}{\text{dC}} \cdot \text{m}$. The divergence of these two results obtained by independent means indicates that there may be an additional mutual influence on the measurement [63].

It is important to note that the temperatures measured are not ambient temperatures, these are the temperatures measured within the sensor unit. The ambient temperature changes during this time were significantly larger. The determined temperature sensitivity is indeed very low and irrelevant for the resolution required in construction site monitoring [63].

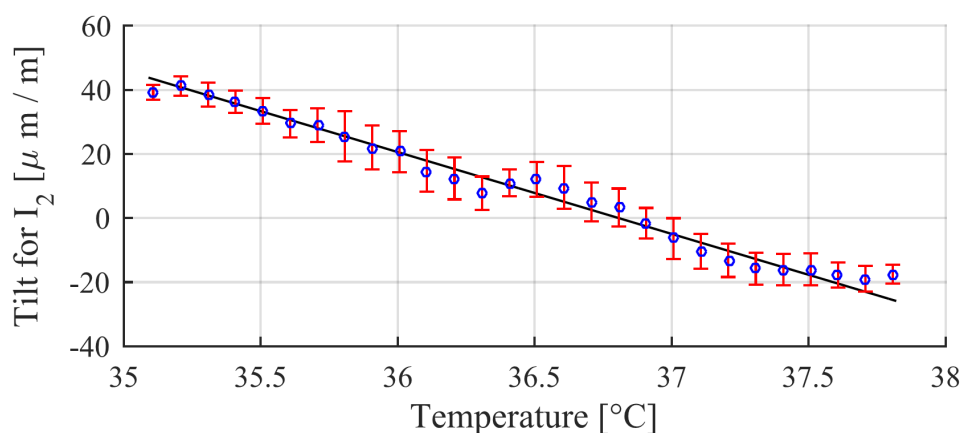


Fig. 2.19 Linear estimation of the correlation between temperature and I_2 , the slope is $s_l = -25.53 \frac{\mu\text{m}}{\text{dC}} \cdot \text{m}$, [63] © 2017 IEEE.

2.6 The SCA830 Single Axis Inclination Sensor

The second type of sensor that was observed is the Murata SCA830 sensor, see Fig. 2.20 for the schematic diagram. This sensor is a single axis inclination sensor with, compared to the SCA103T, just one sensing element. Consequently, it is not

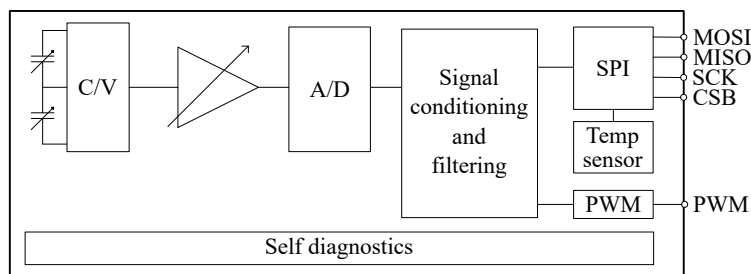


Fig. 2.20 Schematic of the SCA830-D07 MEM inclinometer sensor [1].

possible to perform orthogonalisation prior to signal processing. Data from this sensor

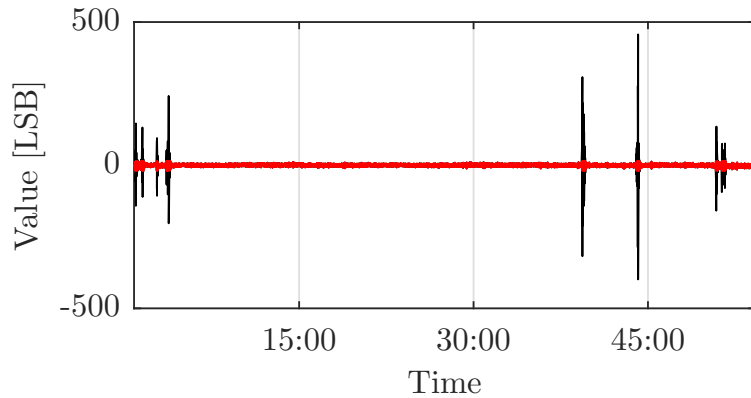


Fig. 2.21 The full signal acquired with the SCA830 sensor over a period of approximately one hour. The portions marked in red correspond to all values lying within 1 % (percentile). This data set contains $n = 400\,693$ samples. The values are in LSB acquired directly from the ADC. The device features a 16-bit ADC with a range of ± 1 g, [63] © 2017 IEEE.

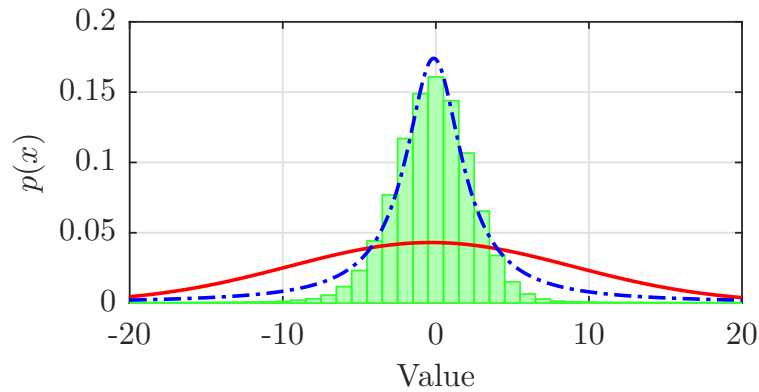


Fig. 2.22 Histogram of the SCA830 Signal, with the Gaussian (red) and Cauchy-Lorentz (blue) models for the complete data set, [63] © 2017 IEEE.

was collected over prolonged periods of time. A sample data set collected over a period of approximately one hour during laboratory testing is shown in Fig. 2.21 [63].

The peaks observed in Figure 2.21 caused much concern and lead to extensive testing of the sensor at night during periods when there was little or no activity in the building. We finally came to the conclusion that the observed peaks are due to disturbances within the building, but are unavoidable in any real application. They lead to wide tails in the probability distributions. In particular when working on construction sites, as reported in [61], such perturbations must be considered [63].

The histogram, Gaussian and Cauchy-Lorentz approximations to the signal from the SCA830 device are shown in Figure 2.22. This result has been obtained using the complete data sequence. Once again the Cauchy-Lorentz distribution provides an appropriate model for the noise behaviour.

Considering the statistics for $p(x)$ in the range $p(x) \in 1 \dots 99\%$. This 98 percentile signal is shown in Fig. 2.21 — it basically corresponds to eliminating local outliers.

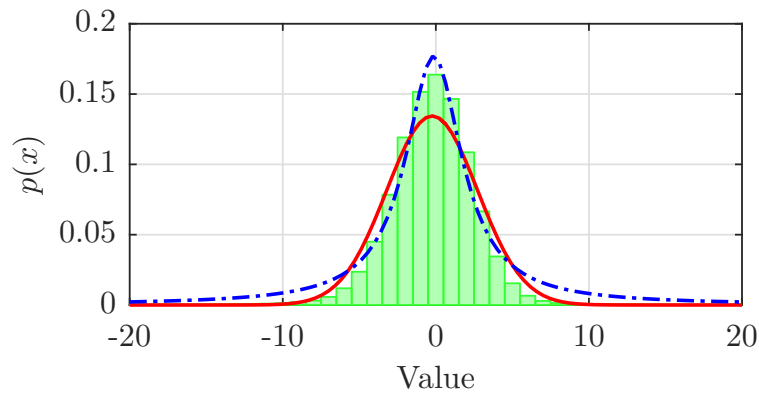


Fig. 2.23 Histogram of the SCA830 Signal, with the Gaussian (red) and Cauchy-Lorentz (blue) models for the centered 98 % percentile of the data set, [63] © 2017 IEEE.

The histogram, Gaussian and Cauchy-Lorentz approximations for this signal are shown in Fig. 2.23. This is an interesting result, since in this case the Gaussian provides a possibly satisfactory noise model. Consequently, after eliminating outliers, it would be possible to apply classical signal processing techniques — although they implicitly assume Gaussian perturbations — to obtain satisfactory results. However, for precision measurements modelling the Cauchy-Lorentz nature of the perturbations is unavoidable [63].

3 | Model Based Reconstruction

In practice inclinometer sensors combined with a solid mathematical framework are the go-to solution for several applications to measure deformation of structures or monitoring foundation for heave, subsidence or settlement. With inclination sensors the deformation cannot be measured directly, but changes in the slope or inclination are used to derive the displacement of a point. Since the inclination is the deviation with respect to the gravity field, inclinometers are best suited for deflection measurements in the vertical or horizontal direction. However, appropriate algorithms are needed to derive the deformations of inclinometer measurements.

The most common model to evaluate data from inclination sensors is a trigonometric approach for inclination sensors, that are mounted to rods of defined length L . The end of the rods are connected with the surrounding structure via e.g. bolts. To enable the measurement of longer structures these rods are connected together via joints and form a inclinometer chain, see Figure 3.1.

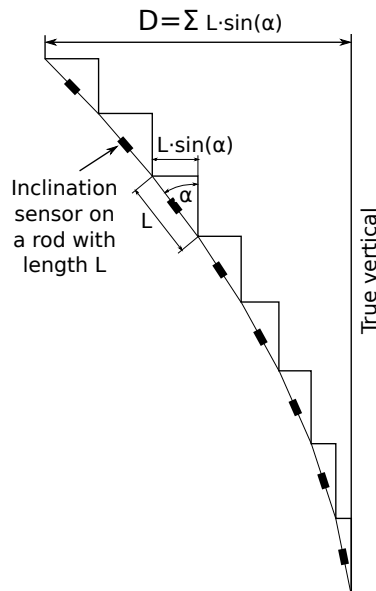


Fig. 3.1 Measurement principle for a vertical in place inclinometer measurement [42].

When acquiring the inclination α_i for the i^{th} inclinometer the horizontal displacement

D_i can be computed by

$$D_i = L \cdot \sin(\alpha_i). \quad (3.1)$$

Summing up all individual horizontal displacements

$$D = \sum_{i=1}^m L \cdot \sin(\alpha_i) \quad (3.2)$$

yield the total horizontal displacement D for the complete vertical inclinometer chain.

The evaluation of the deformation of an inclinometer chain is easy to handle because only trigonometric correlations are used. Since only the inclinations of the rods have an influence on the result and the measurements are independent of the environment, they can also be used for almost all measuring tasks.

The downsides of this kind of measurement are, that the noise of each single sensor spreads to all further evaluated displacements of points, and additional, if one sensing element fails, all deformations of points after the failing sensor couldn't be evaluated either. Also at more complex measurement tasks e.g. no constraints can be taken into account with this method.

When monitoring structures that abide the laws of physics it is possible to set up admissible models to model their deformation.

3.1 Physical Deformation Model

Specific structures have a specific behaviour when they deform. The Euler-Bernoulli equation [21], Equation 3.3, describes the relation between the deflection of a beam and a static applied load q , whereby w is the describing curve of the beam, E the elastic modulus and I the second moment of area for the cross-section.

$$\frac{d^2}{dx^2} \left(EI \frac{d^2 w}{dx^2} \right) = q \quad (3.3)$$


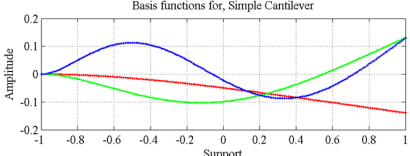

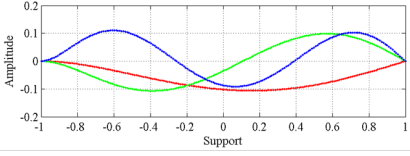

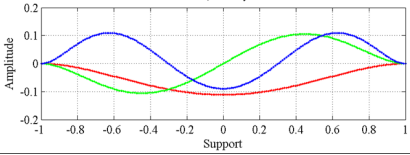

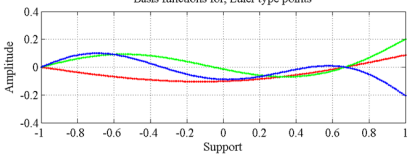
The Euler-Bernoulli equation can be used as model for various problems with different boundary conditions, e.g. one end of the beam is fixed or a specific point has a certain inclination. To yield a unique solution Dirichlet- and Neuman boundary conditions [55] are used to model constraints, i.e. supports, displacements, rotations, etc.

The deformations that a bending beam can take up are determined by the bending modes. Since a physical system assumes an equilibrium at the lowest energy content, the actual bending is composed of the linear combination of the individual bending modes which has the lowest potential under the given boundary conditions [5].

The discrete orthonormal basis functions, presented in Chapter 3.4, are admissible to represent the bending modes for elastic structures with a constant rigidity over the complete length, i.e. a constant E and I [46].

The process of structural modelling of the problem is done prior to installing the sensors on the physical object. The model of the structure combined with sensor positions and the known sensor behaviour enables an estimation of the accuracy of the later measurements. Through this pre-assessment it is possible to optimize the measurement set-up yielding the optimal placement of the sensors.

As an example a beam with different boundary conditions is used, i.e. a cantilever, a cantilever with additional support, a simply supported beam, a beam that is fixed on both sides, etc. The models are shown in Table 3.1 in the left column. In the right column the first four basis functions, that correspond to the problem on the left, are shown.

| physical model | according basis functions |
|---|--|
|  |  |
|  |  |
|  |  |
|  |  |

Tab. 3.1 Examples for standard bending problems of a beam. The plotted basis functions are synthesised by constraint discrete orthogonal basis functions, see Chapter 3.4.

Examples of these physical deformations are found in various structures. For each individual problem a unique mathematical model has to be developed. There are different approaches to set up suitable models. In this thesis the framework is based on constrained polynomials and constrained basis functions.

3.2 Polynomials

Scientists and engineers are often faced with measurement data of different kinds. To interpret the data correctly different aspects have to be considered, e.g. what type of sensor is used, what is the accuracy and precision of the sensor or how does the system, that is measured, react to changes of the input.

A-priori knowledge, that is available for most measurements, can be interpreted and used to model the system. However, the aim is to find an analytical function which describes the correlation of the input and the output in a specific system. The system is described mathematically according to Figure 3.2 whereby the input vector is \mathbf{x} , the output vector is \mathbf{y} and $f(\mathbf{x})$ together with the parameters $\boldsymbol{\alpha}$ are representing the relation of input to output data.

Since throughout this work we are talking about measurement data, the following functions are discrete functions. They map a set of inputs \mathbf{x} to a set of outputs \mathbf{y} , i.e. f is a vector valued function of a vector.

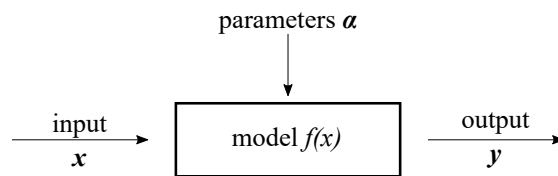


Fig. 3.2 General mathematical model for a measurement system. The mapping between input \mathbf{x} and output \mathbf{y} is defined by the model $f(\mathbf{x})$ and the corresponding parameters $\boldsymbol{\alpha}$.

The process of System Identification is used to find a suitable model and the appropriate parameters that describe a specific system. To choose a suitable model $f(\cdot)$ a-priori knowledge of the system is beneficial. Additionally, a limited number of measurements of input and appropriate output values are done, whereby the measurements may be disturbed by noise. With the chosen model and the reference measurements a calibration is performed, where the parameters $\hat{\boldsymbol{\alpha}}$ are estimated via linear regression, denoted here as g , from the input and output data according to:

$$\hat{\boldsymbol{\alpha}} = g(\mathbf{x}, \mathbf{y}). \quad (3.4)$$

Once the model for a system is established and the input of the system is known, the response can be simulated without performing real tests. In this case we are talking about a forward problem.

$$\hat{\mathbf{y}} = f(\mathbf{x}). \quad (3.5)$$

The opposite to the forward problem is the inverse problem, where a specific system

| degree of polynomial | type of polynomial |
|----------------------|--------------------|
| 1 | linear |
| 2 | quadratic |
| 3 | cubic |
| 4 | quartic |
| 5 | quintic |

Tab. 3.2 Naming of polynomials depending on the polynomial degree

response is wished and the model should deliver the input, that has to be applied to the system. Systems often have several input variables, all of which influence the output of the system. For a given output result, different combinations of input variables may be valid, so there may be several correct solutions.

$$\hat{\mathbf{x}} = f^{-1}(\mathbf{y}) \quad (3.6)$$

Typically there is a differentiation between linear and non-linear models. Linear models are numerically easy to handle since they can be described via Matrix vector equations. Finding the parameters of linear models is normally done via linear regression analysis. Non-Linear models can describe much more complex behaviour. Finding the parameters of the model is normally an iterative process and time consuming.

Polynomials are linear functions (linear in the parameters) and well established. Additionally, according to Stone-Weierstrass's approximation theorem [64] a polynomial as mathematical model is in most cases a good starting point, due to the fact, that for every continuous function in a closed interval the polynomial approximation yields a uniform approximation as long as the degree of the polynomial is high enough [64].

3.2.1 Design of Polynomials

Polynomials are often suitable to model data that is based on physical principles. They are also well known by engineers and appear in science and mathematics quite often. Monomials consist of variables and coefficients, a concatenation of several monomials form a polynomial, e.g.

$$y = a_0 + a_1x + a_2x^2 + \dots + a_dx^d = \sum_{i=0}^d a_ix^i \quad (3.7)$$

This equation 3.7 is called a design equation. For polynomials of low degrees special names are used to describe their type [12], such as:

A general notation for a polynomial of a specific degree d is,

$$p_d(x, \alpha_1 \dots \alpha_d) = \sum_{i=0}^d \alpha_i x^i, \quad (3.8)$$

whereby x is the location, where the polynomial is evaluated and $\alpha_1 \dots \alpha_d$ are the coefficients of the polynomial. The given coefficients define the polynomial completely and allow the evaluation of the polynomial on any arbitrary position.

The polynomial can be represented in vector or matrix form. The Vandermonde vector \mathbf{v}_d is defined as,

$$\mathbf{v}_d(x) = [x^d, x^{d-1}, \dots, x^2, x, 1], \quad (3.9)$$

and the coefficient vector as

$$\boldsymbol{\alpha} = [\alpha_d, \alpha_{d-1}, \dots, \alpha_1, \alpha_0]^T. \quad (3.10)$$

Hence, the polynomial can be written as,

$$y = \mathbf{v}_d(x) \boldsymbol{\alpha}. \quad (3.11)$$

If the polynomial gets evaluated on n points these points are combined to form the vector $\mathbf{x}_k = [x_1, \dots, x_n]^T$. Concatenating the Vandermonde vectors \mathbf{v}_d for \mathbf{x}_k yield the Vandermonde matrix \mathbf{V}_d ,

$$\mathbf{V}_d = \begin{bmatrix} x_1^d & x_1^{d-1} & \dots & x_1 & 1 \\ x_2^d & x_2^{d-1} & \dots & x_2 & 1 \\ \vdots & \vdots & & \vdots & \vdots \\ x_n^d & x_n^{d-1} & \dots & x_n & 1 \end{bmatrix} = \begin{bmatrix} \mathbf{v}_d(x_1) \\ \mathbf{v}_d(x_2) \\ \vdots \\ \mathbf{v}_d(x_n) \end{bmatrix} = [\mathbf{x}_k^d, \mathbf{x}_k^{d-1}, \dots, \mathbf{x}_k^1, \mathbf{1}] \quad (3.12)$$

The Vandermonde matrix will be abbreviated as \mathbf{V}_d and is referred to as the design matrix for the polynomial. The matrix equation to evaluate all values of the polynomial for \mathbf{x}_k is

$$\mathbf{y} = \mathbf{V}_d(\mathbf{x}) \boldsymbol{\alpha}. \quad (3.13)$$

3.2.2 Polynomial Regression

In general, a regression analysis yields an unconstrained least squares approximation for a specific model, e.g. a polynomial. For more specific problems, such as those dealt within this thesis, a-priori knowledge of a system can be used to define additional constraints for the problem to enhance the solution. The approximation of constrained polynomials is discussed in Section 3.3.

If the degree $d = 1$, the polynomial regression yields a straight line. This is called linear regression. Each data point p_i of an observation consists of the value pair $[x_i, \tilde{y}_i]^T$, whereby the true \tilde{y}_i value is perturbed by noise δ_{y_i} , this results in the measured value \hat{y}_i ,

$$\hat{y}_i = y_i + \delta_{y_i}. \quad (3.14)$$

In most cases, independent and identically distributed (i.i.d.) Gaussian noise can be assumed for several reasons [34]. The central limit theorem states, that for a sufficiently large number of independent random variables, the normalised sum of the values has the form of a Gaussian distribution, even when the underlying variables are not normally distributed. Therefore, almost all common frameworks for statistical analysis deal with maximum likelihood predictors based on least square approximation, which is well known by scientists and engineers. Although, Gaussian noise is common, other types of noise can also occur, see [63]. Therefore, some care has to be taken and the type(s) of noise present in the system needs to be investigated.

Due to the noise in the signal the data points are not lying exactly on the approximated polynomial, yielding a residual r_i associated with each point,

$$r_i = y_i - \hat{y}_i = y_i - \sum_{i=0}^d a_i x^i. \quad (3.15)$$

Writing this system of equations for n points yields,

$$\begin{bmatrix} r_1 \\ \vdots \\ r_n \end{bmatrix} = \begin{bmatrix} y_1 \\ \vdots \\ y_n \end{bmatrix} - \begin{bmatrix} x_1^d & x_1^{d-1} & \dots & x_1 & 1 \\ \vdots & \vdots & \vdots & \vdots & \vdots \\ x_n^d & x_n^{d-1} & \dots & x_n & 1 \end{bmatrix} \begin{bmatrix} a_d \\ a_{d-1} \\ \vdots \\ a_1 \\ a_0 \end{bmatrix} \quad (3.16)$$

Using vector notation for Equation 3.16 yields,

$$\mathbf{r} = \mathbf{y} - \hat{\mathbf{y}} = \mathbf{y} - \mathbf{V}_d \mathbf{a} \quad (3.17)$$

To minimize the least square approach an optimisation problem is set up, whereby the function, that has to be minimised, the cost or loss function ϵ , is set up as,

$$\epsilon = \sum_{i=0}^n r_i^2 = \mathbf{r}^T \mathbf{r}. \quad (3.18)$$

Substituting for \mathbf{r} and expanding yields,

$$\epsilon = (\mathbf{y} - \mathbf{V}\mathbf{a})^T (\mathbf{y} - \mathbf{V}\mathbf{a}) \quad (3.19)$$

$$\epsilon = \mathbf{y}^T \mathbf{y} - 2\mathbf{a}^T \mathbf{V}^T \mathbf{y} + \mathbf{a}^T \mathbf{V}^T \mathbf{V} \mathbf{a}. \quad (3.20)$$

Building the derivative with respect to \mathbf{a} and equating to zero yields the optimised coefficients \mathbf{a} ,

$$\mathbf{a} = (\mathbf{V}^T \mathbf{V})^{-1} \mathbf{V}^T \mathbf{y}. \quad (3.21)$$

The term $(\mathbf{V}^T \mathbf{V})^{-1} \mathbf{V}^T$ is known as the Moore and Penrose pseudo-inverse [54] and is denoted by \mathbf{V}^+ . It is a least squares approximation to the inverse of a rectangular matrix. Equation 3.21 is also often expressed as:

$$\mathbf{a} = \mathbf{V}^+ \mathbf{y}. \quad (3.22)$$

Now given the coefficient vector \mathbf{a} the estimated values for $\hat{\mathbf{y}}$ can be computed as,

$$\hat{\mathbf{y}} = \mathbf{V} \mathbf{a} \quad (3.23)$$

$$= \mathbf{V} \mathbf{V}^+ \mathbf{y}. \quad (3.24)$$

This review of polynomial regression and the resulting derivations reveal the fundamental algebraic structures needed for approximation by basis functions. The two fundamental equations of polynomial regressions that should stick in memory are:

$$\hat{\mathbf{y}} = \mathbf{V} \mathbf{a} \quad \text{and} \quad \mathbf{a} = \mathbf{V}^+ \mathbf{y}. \quad (3.25)$$

The design matrix \mathbf{V} is the Vandermonde matrix and represents this specific type of polynomial vector basis set. But in general this method is also valid for approximating functions with other vector basis sets, e.g. Fourier or discrete orthogonal basis sets.

3.2.3 Covariance Propagation

The observations of objects often require the use of multiple sensors. When planing the observation the overall accuracy of the complete measurement system has to be estimated. Covariance propagation yields an estimate for the confidence at each computed point.

Let Λ_x be the covariance of the vector \mathbf{x} . The general form of Λ_x for a total of n sensors is

$$\Lambda_x = \begin{bmatrix} Cov(x_1, x_1) & Cov(x_1, x_2) & \dots & Cov(x_1, x_n) \\ Cov(x_2, x_1) & Cov(x_2, x_2) & \dots & Cov(x_2, x_n) \\ \vdots & \vdots & \vdots & \vdots \\ Cov(x_n, x_1) & Cov(x_n, x_2) & \dots & Cov(x_n, x_n) \end{bmatrix}. \quad (3.26)$$

The covariance of one variable with itself is equal to the variance of the single variable $Cov(x_1, x_1) = Var(x_1) = \sigma_{x_1}^2$. These variances are located in the diagonal of Λ_x .

When the statistical data of the sensors is available and the sensors are not affecting each other the covariance matrix can be set up by filling up the diagonal with the variances of the sensors.

If the variance of the individual sensors varies a vector $\boldsymbol{\sigma}^2$, containing the specific variances, has to be set up. The covariance matrix Λ_x is then defined as,

$$\Lambda_x = \text{diag} \{ \boldsymbol{\sigma}^2 \} = \begin{bmatrix} \sigma_1^2 & 0 & \dots & 0 \\ 0 & \sigma_2^2 & \dots & 0 \\ \vdots & \vdots & \vdots & \vdots \\ 0 & 0 & \dots & \sigma_n^2 \end{bmatrix}. \quad (3.27)$$

If all sensors are of the same type, $\sigma_{x_1}^2 = \sigma_{x_2}^2 = \sigma_{x_n}^2 = \sigma^2$, the convolution matrix can be generated by multiplying the variance σ^2 with the identity matrix \mathbf{I} ,

$$\Lambda_x = \sigma^2 \mathbf{I} = \begin{bmatrix} \sigma^2 & 0 & \dots & 0 \\ 0 & \sigma^2 & \dots & 0 \\ \vdots & \vdots & \vdots & \vdots \\ 0 & 0 & \dots & \sigma^2 \end{bmatrix}. \quad (3.28)$$

If no statistical data for the sensors is available the covariance matrix has to be determined with physical measurements. To get a sufficient amount of data several measurements of all m sensors have to be performed. The values of the i^{th} measurement are stored in a vector $\mathbf{x}_i = [x_{1,i}, x_{2,i}, \dots, x_{m,i}]^T$, whereby all measurements vectors are concatenated to the matrix \mathbf{X} .

$$\mathbf{X} = [\mathbf{x}_1, \mathbf{x}_2, \dots, \mathbf{x}_n] = \begin{bmatrix} x_{1,1} & x_{1,2} & \dots & x_{1,n} \\ x_{2,1} & x_{2,2} & \dots & x_{2,n} \\ \vdots & \vdots & \vdots & \vdots \\ x_{m,1} & x_{m,2} & \dots & x_{m,n} \end{bmatrix} \quad (3.29)$$

The covariance matrix Λ_x is now computed by

$$\Lambda_x = \frac{1}{m-1} \sum_{k=1}^m (\mathbf{x}_k - \boldsymbol{\mu}_x)(\mathbf{x}_k - \boldsymbol{\mu}_x)^T, \quad (3.30)$$

whereby the vector $\boldsymbol{\mu}_x = [\mu_1, \mu_2, \dots, \mu_m]^T$ contains the mean values of all measurements for each sensor and $\boldsymbol{x}_k = [x_{1,k}, x_{2,k}, \dots, x_{m,k}]^T$ contains all values of the k^{th} measurement.

To perform a covariance propagation a suitable mathematical model for the specific problem has to be set up and the covariance matrix Λ_x containing the statistical data has to be set up. Here the covariance propagation will be shown for the case of a linear differential operator \mathbf{L} , where the model is defined as:

$$\boldsymbol{y} = \mathbf{L} \boldsymbol{x}. \quad (3.31)$$

Beside the model also the covariance matrix is needed. The covariance itself is a measure for the relation between two random variables. If there is no mutual influence between two random variables the covariance is zero. In the covariance matrix the covariances between all variables and also the covariances of random variables with themselves are combined. The covariance Λ of a vector \boldsymbol{y} is defined as,

$$\Lambda_y \equiv \{\boldsymbol{y} - E(\boldsymbol{y})\} \{\boldsymbol{y} - E(\boldsymbol{y})\}^T, \quad (3.32)$$

where $E(\boldsymbol{y})$ is the expected value of \boldsymbol{y} . Substituting Equation 3.31 results in:

$$\Lambda_y = \{\mathbf{L} \boldsymbol{x} - E(\mathbf{L} \boldsymbol{x})\} \{\mathbf{L} \boldsymbol{x} - E(\mathbf{L} \boldsymbol{x})\}^T \quad (3.33)$$

$$= \mathbf{L} \{\boldsymbol{x} - E(\boldsymbol{x})\} \{\boldsymbol{x} - E(\boldsymbol{x})\}^T \mathbf{L}^T \quad (3.34)$$

$$= \mathbf{L} \Lambda_x \mathbf{L}^T. \quad (3.35)$$

If the model and the covariance matrix are available the covariance propagation can be determined by,

$$\Lambda_y = \mathbf{L} \Lambda_x \mathbf{L}^T \quad (3.36)$$

With an appropriate system model and knowledge of the noise of each sensor the covariance propagation can also be used to compute a prediction and a confidence interval for derived data. To verify the correctness of the model a Monte-Carlo simulation [15] can be used, whereby data sets with known random noise are generated as input for the model computation. The output of the simulation yields data where the statistics can be computed and the correctness of the prediction can be verified [8].

3.3 Constrained Polynomials

When a physical system is monitored, commonly a-priory knowledge is available, since there is a reason to start the monitoring of this specific system. This knowledge of the system is used to set up a suitable model [50]. In addition, a detailed knowledge of a system allows the recognition and recording of boundary conditions which can be used to further improve the result of a calculation, e.g. at sea level water freezes at 0 °C and has its atmospheric boiling point at 100 °C. These constraints regularize the solutions of the observed system, since they lower the degrees of freedom of the system.

Common constraints are zero points, key value pairs or specific slopes at defined points. Examples of constraints are shown in Figure 3.3.

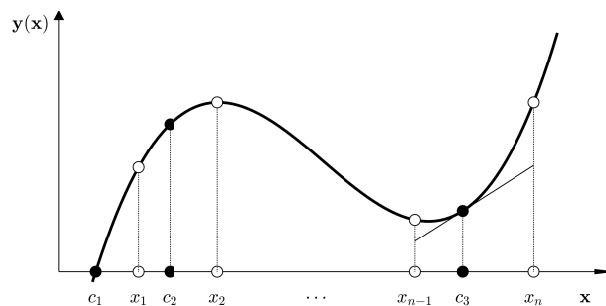


Fig. 3.3 A polynomial with three different types of constraints. At location c_1 a known zero constraint is implemented, location c_2 represents a known value pair and at location c_3 a constraint with a defined slope (derivative constraint) is shown [50].

There are different ways to define these constraints. The constraints on polynomials are in the form,

$$y(c)^{(k)} = a, \quad (3.37)$$

whereby c represents the location of the constraint; k the order of the derivative of the specific constraint and a the value of the constraint. A very general way to define the constraints is to use a triplet of values $\mathbf{t} = [c, k, a]$, whereby all triplets of constraints of a specific polynomial can be concatenated to the matrix \mathbf{T} . Each row in this matrix represents one generalised constraint of a total of m constraints:

$$\mathbf{T} = [\mathbf{t}_1, \mathbf{t}_2, \dots, \mathbf{t}_m]^T = \begin{bmatrix} c_1 & k_1 & a_1 \\ c_2 & k_2 & a_2 \\ \vdots & \vdots & \vdots \\ c_m & k_m & a_m \end{bmatrix}. \quad (3.38)$$

This type for representing the constraints enables the implementation of initial and boundary value constraints that are not only limited to positions of data points x_i , it is possible to locate the constraints at any desired position of the system [50].

Depending on the system following types of constraints can be applied:

1. Polynomials with known roots, i.e. $y(c) = 0$, see Section 3.3.1;
2. Polynomials with known value pairs, i.e. $y(c) = a$. This special form is called Dirichlet boundary condition, see Section 3.3.2.
3. Polynomials with generalised constraints, i.e. differential constraint $y^{(k)}(x) = a$, whereby a is the value of the k^{th} derivative of $y(c)$. The special form of this constraint where $k = 1$ is called the Neumann constraint, see Section 3.3.3.

3.3.1 Polynomials with Constraining Roots

A polynomial with known zeros has constraints of the type,

$$y(c_i) = 0, \quad (3.39)$$

whereby the locations of the zero constraints are summarised in the vector $\mathbf{c} = [c_1, \dots, c_m]^T$. This type of constraint can be found in many physical and engineering systems related to eigenfunctions that exhibit zero constraints. Especially, if the mathematical problem can be described by Sturm-Liouville equations. E.g. a simple supported cantilever has zero constraints at both supports, see Figure 3.4. In more general problems the solution should also enable the approximation of a constraining polynomial, where the constraining roots are located within or outside the supports of the beam [50].

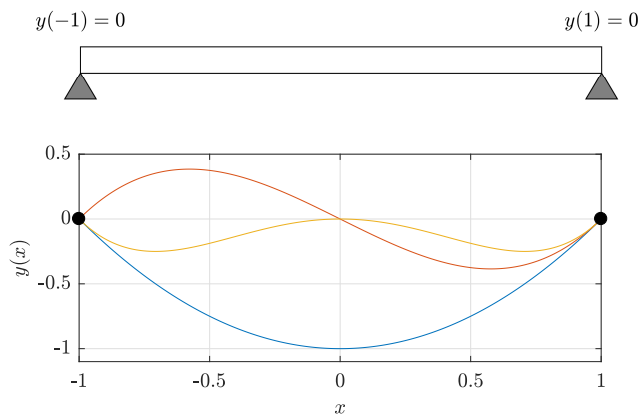


Fig. 3.4 Example for a physical problem with constraining roots: A simple supported beam has zero constraints on both supports [50].

The goal is to approximate a polynomial, $p(x, \boldsymbol{\alpha})$ of degree d while the values of the polynomial are zero at the known locations \mathbf{c} . The approach to solve this problem is, that the proposed polynomial, $p_d(x, \boldsymbol{\alpha})$ is a product of two polynomials,

$$p_d(x, \boldsymbol{\alpha}) = p_m(x, \boldsymbol{\gamma})p_{d-m}(x, \boldsymbol{\beta}), \quad (3.40)$$

whereby $p_m(x, \boldsymbol{\gamma})$ represents the polynomial defining the roots and $p_{d-m}(x, \boldsymbol{\beta})$ is the polynomial approximation for the residual of $p_d(x, \boldsymbol{\alpha})$ and $p_m(x, \boldsymbol{\gamma})$.

Since the polynomial $p_m(x, \boldsymbol{\gamma})$ is defined by the roots this polynomial is known prior to the approximation and can be computed by,

$$p_m(x, \boldsymbol{\gamma}) = \prod_{k=1}^m (x - c_k) \quad (3.41)$$

With the given coefficients $\boldsymbol{\gamma}$ the task of the approximation is to determine the coefficients $\boldsymbol{\beta}$ that minimize the residual values in a least square sense. Then the mapping of $\boldsymbol{\beta}$ to $\boldsymbol{\alpha}$ to yield the required coefficients. Additionally, the covariance $\Gamma_{\boldsymbol{\alpha}}$ can be computed [50].

Algebraic Formulation

The model for the polynomial is,

$$\mathbf{y} = \mathbf{V}\boldsymbol{\alpha}, \quad (3.42)$$

whereby \mathbf{V} is the Vandermonde Matrix and $\boldsymbol{\alpha}$ are the coefficients resulting from the product of the polynomials $p_m(x, \boldsymbol{\gamma})$ and $p_{d-m}(x, \boldsymbol{\beta})$. The coefficients $\boldsymbol{\gamma}$ for the polynomial representing the zero constraints are derived by expanding the product,

$$\prod_{k=1}^m (x - c_k) = (x - c_1)(x - c_2) \dots (x - c_m). \quad (3.43)$$

There are several methods available to multiply two polynomials. The convolution can be applied directly as $\boldsymbol{\alpha} = \boldsymbol{\gamma} * \boldsymbol{\beta}$ or the coefficients of $\boldsymbol{\gamma}$ are used to form the convolution matrix Γ ,

$$\Gamma = \begin{bmatrix} \gamma_1 & 0 & 0 \\ \gamma_0 & \gamma_1 & 0 \\ 0 & \gamma_0 & \gamma_1 \\ 0 & 0 & \gamma_0 \end{bmatrix}. \quad (3.44)$$

The use of the convolution matrix Γ is necessary in this case, since it enables setting up an optimisation problem to minimize the residual r . If $\boldsymbol{\beta} = [\beta_2, \beta_1, \beta_0]^T$ and $\boldsymbol{\gamma} = [\gamma_1, \gamma_0]^T$ then $\boldsymbol{\alpha}$ is computed as,

$$\boldsymbol{\alpha} = \Gamma\boldsymbol{\beta} = \begin{bmatrix} \gamma_1 & 0 & 0 \\ \gamma_0 & \gamma_1 & 0 \\ 0 & \gamma_0 & \gamma_1 \\ 0 & 0 & \gamma_0 \end{bmatrix} \begin{bmatrix} \beta_2 \\ \beta_1 \\ \beta_0 \end{bmatrix} \quad (3.45)$$

Substituting this term into Equation 3.42 results in,

$$\mathbf{y} = \mathbf{V}\Gamma\boldsymbol{\beta}. \quad (3.46)$$

The residual \mathbf{r} is computed by,

$$\mathbf{r} = \hat{\mathbf{y}} - \mathbf{y} \quad (3.47)$$

$$\mathbf{r} = \hat{\mathbf{y}} - \mathbf{V}\Gamma\boldsymbol{\beta} \quad (3.48)$$

The cost function can now be defined by,

$$\epsilon = \{\hat{\mathbf{y}} - \mathbf{V}\Gamma\boldsymbol{\beta}\}^T \{\hat{\mathbf{y}} - \mathbf{V}\Gamma\boldsymbol{\beta}\} \quad (3.49)$$

Solving this cost function ϵ in a least square sense delivers,

$$\boldsymbol{\beta} = (\mathbf{V}\Gamma)^+ \hat{\mathbf{y}}, \quad (3.50)$$

whereby $(\mathbf{V}\Gamma)^+$ denotes the Moore-Penrose pseudo-inverse of the matrix $(\mathbf{V}\Gamma)$. Instead of computing the pseudo-inverse of $(\mathbf{V}\Gamma)$ it is also possible to compute the inverse via QR decomposition [23],

$$\mathbf{Q}\mathbf{R} = \mathbf{q}\mathbf{r}(\mathbf{V}\Gamma), \quad (3.51)$$

$$\boldsymbol{\beta} = \mathbf{R}^+ \mathbf{Q}^T \hat{\mathbf{y}}. \quad (3.52)$$

The coefficients $\boldsymbol{\alpha}$ can now be computed by $\boldsymbol{\alpha} = \Gamma\boldsymbol{\beta}$.

3.3.2 Polynomial with Constraining Value Pairs

The next type of constraints are polynomials with known value pairs, where for specific x values the corresponding y values are defined. The constraints are in the form of,

$$y(c_i) = a_i \quad (3.53)$$

These known value pairs (c_i, a_i) are contained in the vectors $\mathbf{x}_c = [c_0, \dots, c_m]$ and $\mathbf{y}_c = [a_0, \dots, a_m]$, the noisy data is contained in the vector \mathbf{y} . This problem is the natural extension of the polynomial approximation with known zeros, but in this case instead of the zeros values are given [50].

In Figure 3.5 a polynomial with the according value constraints x_c and y_c (red dots) are shown.

The first task is to find a polynomial $y_p(x)$ of degree $m - 1$ that fulfils all m constraints. This polynomial can be found via polynomial interpolation and yields the coefficients $\boldsymbol{\delta}$ which follows $p_{m-1}(c_i, \boldsymbol{\delta}) = a_i$. Evaluating the polynomial for all x we get $y_p(x) = p_{m-1}(x, \boldsymbol{\delta})$. This portion is the particular solution for the problem, since it is dependent from the particular values of the constraints a_i . The particular solution \mathbf{y}_p for the in Figure 3.5 presented data is shown in Figure 3.6.

After the particular solution is found, the residual for the observation $\hat{\mathbf{y}}$ w.r.t. \mathbf{y}_p is computed by,

$$\hat{\mathbf{y}}_h = \hat{\mathbf{y}} - \mathbf{y}_p. \quad (3.54)$$

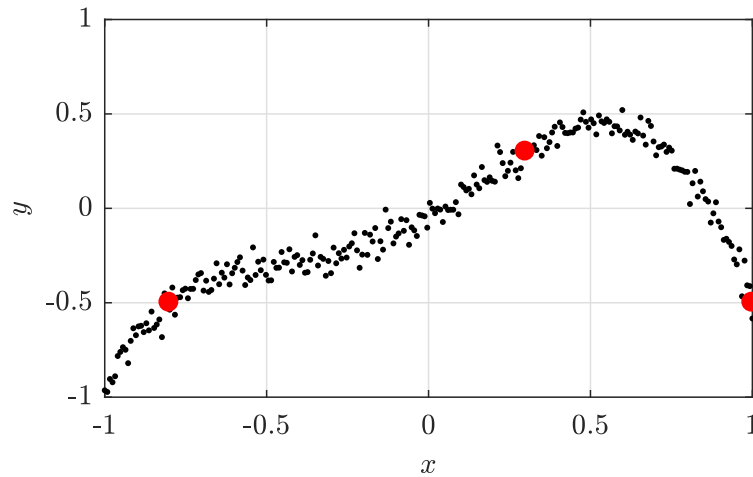


Fig. 3.5 Dataset with constraint value pairs: The black dots represent the noisy data, the red dots the constraining value pairs $\mathbf{x}_c = [-0.8, 0.3, 1]^T$ and $\mathbf{y}_c = [-0.5, 0.3, -0.5]^T$.

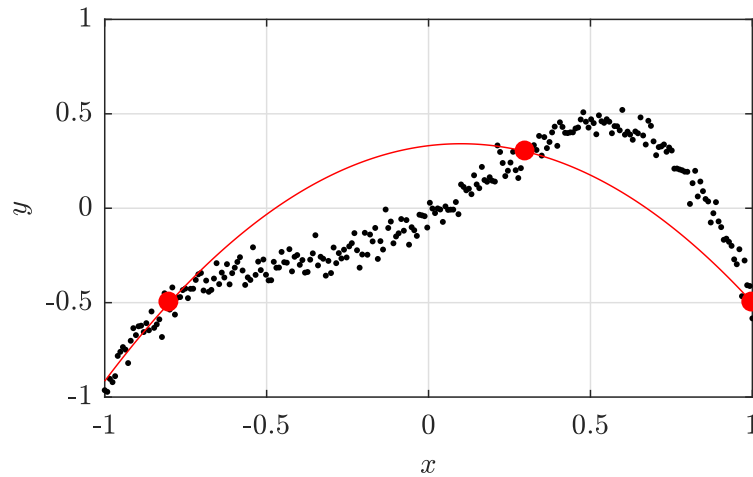


Fig. 3.6 Particular solution for a value constrained polynomial.

The residual $\hat{\mathbf{y}}_h$ is shown in Figure 3.7. Note that the value pair constraints in the residual turned into zero constraints.

The coefficients for a polynomial, that fulfils the constraints in a homogeneous manner can be found via polynomial approximation of $\hat{\mathbf{y}}_h$; this is the same task as done for polynomials with zero constraints, see Section 3.3.1. This portion of the solution, that represents \mathbf{y}_h is independent of the values of the constraints and defined as homogeneous solution [50]:

$$\mathbf{y}_h(x) = \mathbf{p}_m(x, \boldsymbol{\gamma})\mathbf{p}_{d-m}(x, \boldsymbol{\beta}) \quad (3.55)$$

The polynomial consisting of the homogeneous and the particular solution is defined as:

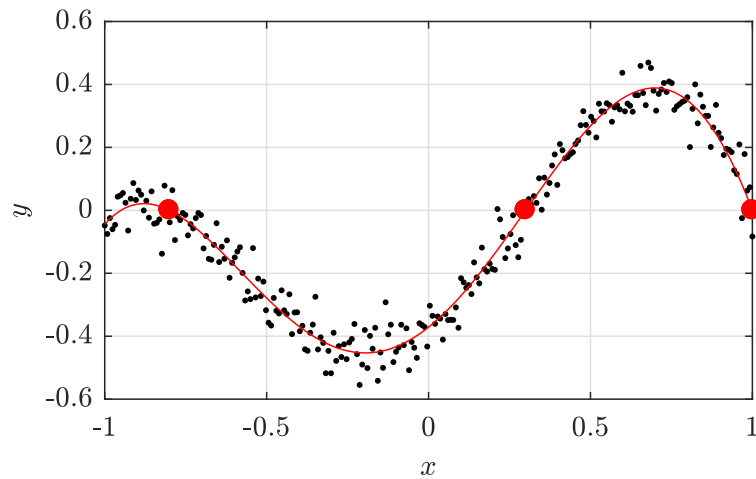


Fig. 3.7 Homogeneous solution for a value constraint polynomial. The homogeneous solution is the residual of the observed data and the particular solution.

$$p_d(x, \boldsymbol{\alpha}) = \underbrace{p_m(x, \boldsymbol{\gamma}) p_{d-m}(x, \boldsymbol{\beta})}_{y_h(x)} + \underbrace{p_{m-1}(x, \boldsymbol{\delta})}_{y_p(x)}. \quad (3.56)$$

The sum of the homogeneous and the particular solution yield the approximation for the observed data with the constraining key value pairs. The approximation for the original observed data with the a-priori known value constraints is shown in Figure 3.8.

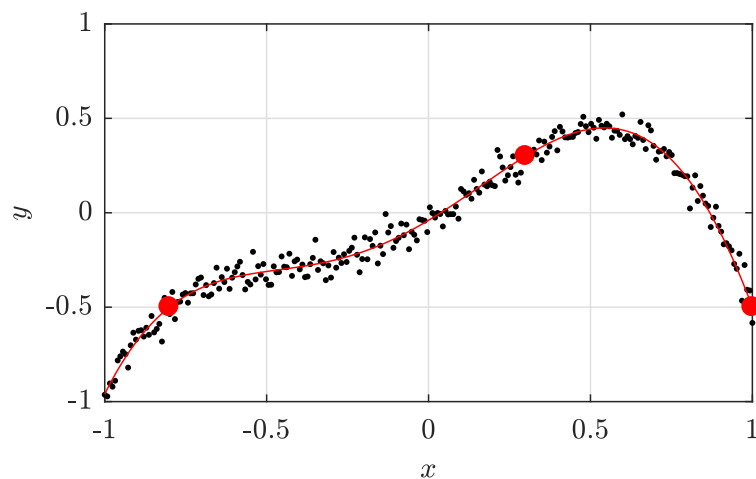


Fig. 3.8 The final approximation for the value constrained data yielded from the sum of the homogeneous and the particular solution.

The functions generated for solving the problem are presented in Figure 3.9.

The approximation of the polynomial can be summarised into the following simple algebraic steps:

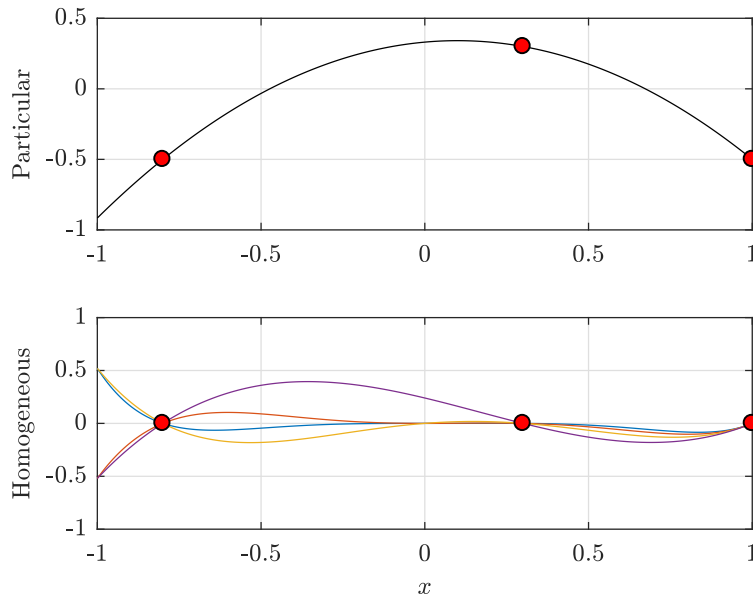


Fig. 3.9 The final approximation for the value constrained data yielded from the sum of the homogeneous and the particular solution.

1. Determine the coefficients $\boldsymbol{\delta}$ of the particular polynomial $p(x_i, \boldsymbol{\delta})$ via interpolation, whereby any algorithm, that yields a polynomial consisting of monomials that fulfils the constraints, is suitable.
2. Next we compute the homogeneous data, $\hat{y}_h(x_i) = \hat{y}_i - p(x_i, \boldsymbol{\delta})$ and use polynomial interpolation to yield the coefficients $\boldsymbol{\gamma}$ of the polynomial that fulfils the zero constraints of the residual, i.e. $p_m(x, \boldsymbol{\alpha})$.
3. Use polynomial approximation as presented in 3.3.1 for the homogeneous portion of the problem.
4. Compute $\boldsymbol{\alpha}$ from $\boldsymbol{\gamma}$, $\boldsymbol{\beta}$ and $\boldsymbol{\delta}$ according to,

$$\boldsymbol{\alpha} = \boldsymbol{\gamma} * \boldsymbol{\beta} + \boldsymbol{\delta}, \quad (3.57)$$

whereby the $*$ operator denotes a convolution for polynomial multiplication [31, 50].

3.3.3 Polynomial Approximation with Generalised Constraints

Since the constraints in physical problems are not limited to known roots or known value pairs it is also necessary to be able to compute solutions for problems with a more general type of constraints. Considering a cantilever with constraints just on one side. To fully describe such a system, derivative constraints up to order three have to be taken into account, see Figure 3.10.



Fig. 3.10 Normal and derivative constraints on a cantilever.

A more general form to describe the constraints is,

$$\left. \frac{d^k y(x)}{d x^k} \right|_c = y^{(k)}(c) = a. \quad (3.58)$$

This allows the structured implementation of multiple constraints at defined locations c_i with different orders k_i of the derivatives and also different corresponding values a_i of the constraint. These values can be combined to a triplet t_i of values to enable a structured description of the constraints,

$$t_i = [c_i, k_i, a_i], \quad (3.59)$$

whereby the triplets are concatenated to the Matrix $\mathbf{T} \triangleq [t_1, \dots, t_m]^T$. This possibility for defining the constraints in such a general way enables the definition of more complex problems that can be solved with this approach. A large family of inverse problems related to systems governed by ordinary differential equations, that can be formulated as e.g. initial value or boundary value problems, have such derivative constraints that are known a-priori [50].

The use of this approach also enables the generation of a vector basis set, that spans a sub-space of functions that fulfil the constraints at this location. These functions, that are represented by the sub-space, are called admissible functions.

Being able to describe where the constraint i with the derivative order of k_i with the value a_i is located at the position c_i we need a suitable method to implement these constraints in a manner that enables the computation of a solution for the specific problem.

The problem can be separated into a homogeneous and a particular solution, whereby the particular solution fulfils the constraints and the homogeneous solution approximates the noisy data of the residual of the particular solution. To find the particular solution a polynomial has to be found, that fulfils all the constraints, including the k^{th} derivative ones.

To fit a polynomial to normal and derivative constraints a specific design matrix \mathbf{C} is set up, where each concatenated row defines the solution to one specific constraint. For normal constraints the Vandermonde vector \mathbf{v}_d is used, for derivative constraints the Vandermonde vector is derived according to the degree of derivation k of the constraint [50].

The derivation of a polynomial is straight forward, since the derivative of each term can be computed by,

$$\frac{d}{dx} \sum_{k=0}^n a_k x^k = \sum_{k=1}^n k \cdot a_k x^{k-1} \quad (3.60)$$

The equation to compute a value with the Vandermonde vector \mathbf{v}_d and the coefficients $\boldsymbol{\alpha}$ is

$$y(x) = \mathbf{v}_d \boldsymbol{\alpha} = \alpha_d x^d + \alpha_{d-1} x^{d-1} + \dots + \alpha_1 x + \alpha_0. \quad (3.61)$$

The first derivative of the polynomial in Equation 3.61 is

$$\dot{y}(x) = d \alpha_d x^{d-1} + (d-1) \alpha_{d-1} x^{d-2} + \dots + 2 \alpha_2 x + \alpha_1 \quad (3.62)$$

There are two possibilities to define the derivative of the polynomial to enable the following computations. The first possible definition of the derivative is to define a vector,

$$\dot{\boldsymbol{\alpha}} = \begin{bmatrix} 0 \\ d \alpha_d \\ (d-1) \alpha_{d-1} \\ \vdots \\ 2 \alpha_2 \\ \alpha_1 \end{bmatrix} \quad (3.63)$$

such that,

$$\dot{\mathbf{y}}(x) = \mathbf{v}_d(x) \dot{\boldsymbol{\alpha}}. \quad (3.64)$$

Using this definition of $\dot{\boldsymbol{\alpha}}$ the relation between $\boldsymbol{\alpha}$ and $\dot{\boldsymbol{\alpha}}$ is

$$\dot{\boldsymbol{\alpha}}_{k-1} = k \boldsymbol{\alpha}_k, \quad (3.65)$$

whereby each coefficient is shifted by one location and additionally scaled by k .

The second possibility is to formulate $\dot{\mathbf{y}}(x)$ via the derivative of the Vandermonde vector $\dot{\mathbf{v}}_d(x)$ such that

$$\dot{\mathbf{y}}(x) = \dot{\mathbf{v}}_d(x) \boldsymbol{\alpha}. \quad (3.66)$$

An algebraic formulation in this manner enables a least square approximation of constrained data. The vector $\dot{\mathbf{v}}_d(x)$ used in Equation 3.66 is defined as,

$$\dot{\mathbf{v}}_d(x) \triangleq [d x^{d-1}, (d-1) x^{d-2}, \dots, 1, 0]. \quad (3.67)$$

To allow an efficient computation of $\dot{\mathbf{v}}_d(x)$ a matrix \mathbf{M} has to be determined such that,

$$\dot{\mathbf{v}}_d(x) = \mathbf{v}_d(x) \mathbf{M}. \quad (3.68)$$

The task of the matrix \mathbf{M} is to form the derivative $\frac{d}{dx}$ of a polynomial, whereby each monomial can be differentiated on its own. To yield the derivative of a monomial

the term is scaled by the exponent of x and the exponent reduced by one number. In the notation for polynomials the reduction of the exponent is yielded by shifting all terms by one place in the vector. For the scaling the vector s is defined as,

$$s = [d, (d - 1), \dots, 2, 1] \quad (3.69)$$

and extended to a scaling matrix S via

$$S = \text{diag}\{\mathbf{s}\}. \quad (3.70)$$

To shift all entries by one position the matrix M is generated in the form

$$M = \begin{bmatrix} 0 & 0 \\ S & 0 \end{bmatrix}. \quad (3.71)$$

Using this definition in Equation 3.66 we obtain,

$$\dot{\mathbf{y}}(x) = \mathbf{v}_d(x) M \boldsymbol{\alpha}, \quad (3.72)$$

thus, following relationships can be determined,

$$\dot{\mathbf{v}}_d(x) = \mathbf{v}_d(x) M \quad (3.73)$$

$$\dot{\boldsymbol{\alpha}} \triangleq M \boldsymbol{\alpha}. \quad (3.74)$$

This approach is also valid for derivations of higher degrees, e.g. the derivative if the i^{th} order is computed as,

$$\mathbf{v}_d^{(i)}(x) = \mathbf{v}_d(x) M^i \quad (3.75)$$

$$\boldsymbol{\alpha}^{(i)} = M^i \boldsymbol{\alpha}. \quad (3.76)$$

With these definitions available we can set up a formulation for the constraints. For each constraint a triplet is defined,

$$t_i = [c_i, k_i, a_i]. \quad (3.77)$$

These triplets are used to define constraining vectors $\mathbf{v}_d^{k_i}(c_i)$, which are combined together to a set of equations of the form:

$$\begin{bmatrix} \mathbf{v}_d^{(k_1)}(c_1) \\ \vdots \\ \mathbf{v}_d^{(k_m)}(c_m) \end{bmatrix} \boldsymbol{\alpha} = \begin{bmatrix} a_1 \\ \vdots \\ a_m \end{bmatrix}. \quad (3.78)$$

This set of equations specify the constraints and degrees of freedom of the system. Defining the matrix of constraining vectors $\mathbf{v}_d^{k_i}(c_i)$ as matrix C allows the formulation of Equation 3.78 as,

$$C \boldsymbol{\alpha} = \mathbf{a}. \quad (3.79)$$

The rank of the matrix $r_c = \text{rank}(\mathbf{C})$ indicates the number of independent constraints. If r_c is smaller than the number of constraints m there are redundant constraints. A further condition that has to be fulfilled is, that all values \mathbf{a} must lie in the range of \mathbf{C} , $\mathbf{a} \in \text{range}\{\mathbf{C}\}$. If these conditions are not fulfilled the constraints are inconsistent [50].

Approximating the vector $\boldsymbol{\alpha}$ from Equation 3.79 yields,

$$\boldsymbol{\alpha} = \mathbf{C}^+ \mathbf{a} + \mathbf{N}_c \boldsymbol{\gamma} \quad (3.80)$$

whereby \mathbf{N}_c forms a orthonormal vector basis set for the null-space of \mathbf{C} .

Expanding the resulting equation for \mathbf{y} ,

$$\mathbf{y} = \mathbf{V}\{\mathbf{C}^+ \mathbf{a} + \mathbf{N}_c \boldsymbol{\gamma}\} \quad (3.81)$$

yields,

$$\mathbf{y} = \underbrace{\mathbf{V}\mathbf{C}^+ \mathbf{a}}_{\mathbf{y}_p} + \underbrace{\mathbf{V}\mathbf{N}_c \boldsymbol{\gamma}}_{\mathbf{y}_h}. \quad (3.82)$$

Equation 3.82 shows, that the equation splits into a particular solution \mathbf{y}_p , that fulfils the generalised constraints, and a homogeneous solution \mathbf{y}_h , which is used to perform the least square approximation [50].

Implementation

The solution of this task is structured into following tasks:

1. Set up the Matrix \mathbf{T} containing the triplets t_i for each constraint.
2. Compute the Matrix \mathbf{C} from the constraint values contained in \mathbf{T} and the Vandermonde vector \mathbf{v}_d or one of his derivatives ($c_i = \mathbf{v}(\mathbf{c}_i)\mathbf{M}^k$).
3. Find a particular solution $y_p = \mathbf{p}(c_i, \alpha_p)$ that fulfils the given constraints, whereby also k -derivative constraints have to be taken into account in this solution portion. The coefficients $\boldsymbol{\alpha}_p$ are computed via,

$$\boldsymbol{\alpha}_p = \mathbf{C}^+ \mathbf{a} \quad \text{and} \quad (3.83)$$

$$\mathbf{y}_p = \mathbf{V}\mathbf{C}^+ \mathbf{a} \quad (3.84)$$

4. Compute the homogeneous portion of the problem as residual from the given noisy data and the particular solution, e.g.

$$\hat{\mathbf{y}}_h = \hat{\mathbf{y}} - \mathbf{y}_p \quad (3.85)$$

5. Approximate a polynomial $\mathbf{p}(\hat{\mathbf{y}}_h, \boldsymbol{\alpha}_h)$ representing the homogeneous solution, that fulfils the resulting zero constraints of the residual $\hat{\mathbf{y}} - \mathbf{y}_p$. The coefficients

of the homogeneous solution $\boldsymbol{\alpha}_h$ may be also denoted as $\boldsymbol{\gamma}$ within this thesis. To compute the coefficients $\boldsymbol{\gamma}$ for the homogeneous solution the null-space \mathbf{N}_C for C has to be computed.

The null-space \mathbf{N}_C is a vector basis set of orthogonal functions which represents all polynomials that are valid solutions and fulfil the constraints in a homogeneous manner. $\boldsymbol{\gamma}$ is computed according to,

$$\boldsymbol{\gamma} = (\mathbf{V}\mathbf{N}_C)^+ \hat{\mathbf{y}}_h. \quad (3.86)$$

6. The final approximation is the sum of the particular and the homogeneous portion,

$$\mathbf{y} = \mathbf{y}_h + \mathbf{y}_p. \quad (3.87)$$

The coefficient $\boldsymbol{\alpha}$ for our model $\mathbf{y} = \mathbf{V}\boldsymbol{\alpha}$ is the sum of the coefficients of the particular and the homogeneous solution,

$$\boldsymbol{\alpha} = \boldsymbol{\alpha}_p + \boldsymbol{\alpha}_h = C^+ \mathbf{a} + \mathbf{N}_C \boldsymbol{\gamma}. \quad (3.88)$$

Covariance Propagation

The covariance matrix $\Lambda_{\hat{\mathbf{y}}}$ is computed from the noisy data $\hat{\mathbf{y}}$. When we compute the homogeneous solution using the approximation of Equation 3.86 we yield,

$$\mathbf{y}_h = \mathbf{V}\mathbf{N}_C \boldsymbol{\gamma} = \underbrace{\mathbf{V}\mathbf{N}_C \{\mathbf{V}\mathbf{N}_C\}^+}_{\mathbf{K}} \hat{\mathbf{y}}_h. \quad (3.89)$$

With the definition

$$\mathbf{K} \triangleq \mathbf{N}_C \{\mathbf{V}\mathbf{N}_C\}^+ \quad (3.90)$$

from Equation 3.89 we can compute the covariance of $\Lambda_{\boldsymbol{\alpha}}$ by

$$\Lambda_{\boldsymbol{\alpha}} = \mathbf{K} \Lambda_{\hat{\mathbf{y}}} \mathbf{K}^T. \quad (3.91)$$

3.4 Basis Functions

The columns in the design matrix \mathbf{B} , introduced in Section 3.2, are the basis for a function space, which allows the representation of every continuous function as an independent linear combination of basis functions. In the case of using geometric polynomials, they are the monomial basis and are called Vandermonde basis. This basis functions are easy to use and wide spread in the literature [36]. However, the use of the Vandermonde matrix leads to a number of problems and limit the practical usability, since the basis functions are not orthogonal.

As a consequence of this, the computation of \mathbf{B}^+ is computationally expensive and quickly becomes numerically degenerate as the degree of the polynomial increases. This makes it impossible to compute a useable inverse. The condition number of the Vandermonde Basis of degree $d = 10$ and $n = 100$ points equally spaced between $[-1 \leq x \leq 1]$ is $> 10^4$ which makes the Vandermonde not suitable for solving large scale problems. The high condition number is an indication for an ill-conditioned problem, which leads to inaccuracies when computing the inverse of the design matrix.

There are several basis functions beside the Vandermonde basis that can be used for approximating data that can be classified in three main groups according to their moment, [48]:

1. Geometric moments
2. Polar moments
3. Periodic moments

Choosing a basis for a specific problem depends on the nature of the data being analysed and on the model features. When using a suitable basis function set the amount of redundancy information is minimised as are the effects of Runge's phenomena and Gibbs error [48]. Using a different type of basis function doesn't change the basic principles for computations with them.

The focus in this thesis is mainly on geometric moments, since these ones are used to describe bending of structures and therefore used for reconstructions in geo-monitoring.

3.4.1 Nomenclature

When discussing basis functions we also have to define a specific nomenclature prior to defining an algebraic framework. Since all basis functions are related to each other they can fulfil specific conditions.

If functions are **orthogonal** they have the mathematical property of describing non-overlapping, uncorrelated or independent objects of some kind. In a mathematical view two vectors are orthogonal if the inner/scalar product is zero, e.g. $\mathbf{x}^T \mathbf{y} = \mathbf{y}^T \mathbf{x} = 0$ while $\mathbf{x}^T \mathbf{x} = \xi$ and $\mathbf{y}^T \mathbf{y} = \psi$ and ξ and ψ are scalars.

Orthogonality does not refer to the magnitude of the vectors. If two vectors are **orthonormal** the vectors form a set of unit vectors, e.g. $\mathbf{x}^T \mathbf{x} = 1$ and $\mathbf{y}^T \mathbf{y} = 1$ while the condition $\mathbf{x}^T \mathbf{y} = \mathbf{y}^T \mathbf{x} = 0$ is still fulfilled. If the vectors are complex, $x, y \in \mathbb{C}$, the vector basis set is called a unitary set. The same concept is also expanded to matrices like the basis functions that result in following nomenclature [27],

1. **orthogonal** basis $\mathbf{B}^T \mathbf{B} = \mathbf{C}$, where \mathbf{C} is a diagonal matrix and
2. **orthonormal** basis $\mathbf{B}^T \mathbf{B} = \mathbf{I}$, where \mathbf{I} is the identity matrix.

For completeness there are also additional basis sets, like the unitary or weighted orthogonal basis, that are also described in literature, see [49], but not specially handled in this thesis.

Synthesising Basis Functions

For approximating discrete data with discrete basis functions in a least square sense the support points of the basis functions have to be identical with the points on the x-axis. There are several algorithms available for synthesising these functions that use a recurrence relationship, e.g. for the Vandermonde basis the following relationship is used,

$$b_n = \begin{cases} 1, & \text{for } n = 0 \\ x, & \text{for } n = 1 \\ b_{n-1}^2, & \text{for } 2 \leq n \leq d \end{cases} \quad (3.92)$$

which yields the Vandermonde matrix,

$$\mathbf{V} = \begin{bmatrix} 1 & x_1 & x_1^2 & \dots & x_1^d \\ \vdots & \vdots & \vdots & \vdots & \vdots \\ 1 & x_n & x_n^2 & \dots & x_n^d \end{bmatrix}. \quad (3.93)$$

As stated already before, the Vandermonde Matrix is bad conditioned and not orthogonal, and that leads to several problems. It also becomes degenerate at high degrees ($d \gtrsim 8$), thus there is no unique inverse and therefore, the Vandermonde basis is not suitable for signal synthesis [27].

Legendre Polynomials

There are several methodologies available for the generation of discrete orthogonal basis functions that are based on a three-term recurrence relationship of the form [10, 20],

$$\mathbf{b}_n = \alpha_n(\mathbf{b}_{n-1} \circ \mathbf{x}) + \beta_n \mathbf{b}_{n-2}. \quad (3.94)$$

\mathbf{x} represents the vector of the support nodes, that may be arbitrarily spaced on the x-axis. The two scalar recurrence coefficients $\{\alpha_n, \beta_n\}$ are mutable, different values for them deliver different polynomials, e.g. the Legendre polynomials can be synthesised using the recurrence relationship with α_n and β_n defined as,

$$\alpha_n = \frac{(2n+1)}{n+1} \quad \text{and} \quad \beta_n = \frac{n}{n+1} \quad (3.95)$$

yielding

$$b_n(x) = \frac{(2n+1)}{n+1} x \circ b_{n-1}(x) - \frac{n}{n+1} \circ b_{n-2}(x). \quad (3.96)$$

The first two basis functions for the synthesis are $b_0 = \mathbf{0}$ and $b_1 = \mathbf{x}$. The Legendre polynomials fulfil the orthogonality condition in the range $x = [-1, 1]$ in an integral sense, such that

$$\int_{-1}^{+1} P_m(x) P_n(x) dx = \begin{cases} 0 & \text{if } p \neq q, \\ \frac{2}{2p+1} & \text{if } p = q. \end{cases} \quad (3.97)$$

These basis functions are not orthogonal for discrete values. The quality of the basis functions with respect to their orthogonality can be verified by interpreting the residual matrix \mathbf{R} . For computing \mathbf{R} first the basis functions \mathbf{B} are synthesised with the redundancy relationship from Equation 3.96 and \mathbf{x} , a vector with equally spaced nodes in the interval of $[-1, 1]$. The first six Legendre polynomials for degree $d = 10$ on $n = 100$ equidistant nodes are shown in Figure 3.11.

The matrix of residual errors for a set of basis functions can be computed as,

$$\mathbf{R} = \mathbf{B}^T \mathbf{B} - \text{diag}(\mathbf{B}^T \mathbf{B}). \quad (3.98)$$

Considering a perfectly orthogonal basis set all elements of the residual matrix \mathbf{R} would be zero. The residual matrix for the Legendre polynomials are shown in Figure 3.12. Observing this residual matrix, it is obvious that the discrete Legendre basis functions are not orthogonal.

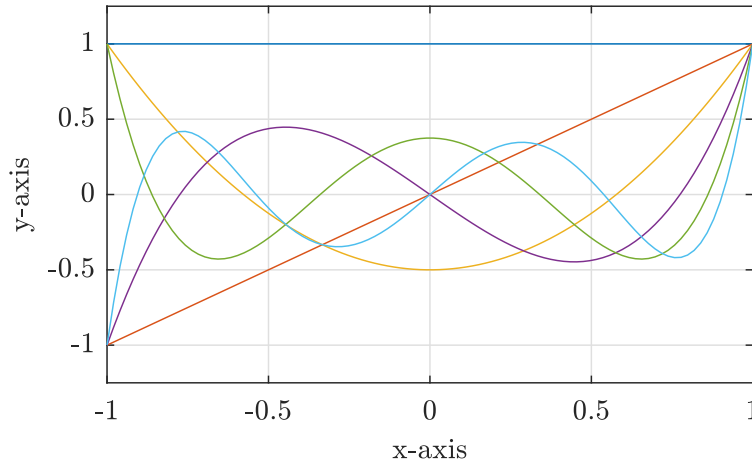


Fig. 3.11 Plot of the first six Legendre polynomials in the interval of $[-1, 1]$.

These Legendre polynomials are one example for synthesising basis functions from a recurrence relationship. Beside these Legendre polynomials there are also other basis functions that can be synthesised by recurrence relations like the Chebyshev or Gram-Schmidt polynomials, see [16, 60].

Gram-Schmidt Polynomials

The Gram-Schmidt polynomials [26] are continuous polynomials which form a complete orthogonal (and unitary) set of basis functions, if they are synthesised by uniformly spaced nodes. The Gram-Schmidt recurrence relation performs an orthogonalisation, referred to as Gram-Schmidt orthogonalisation, that can also be used for the QR-decomposition of matrices. Theoretically, the Gram-Schmidt polynomials form an ideal basis, fulfilling an ideal orthogonally condition:

$$\int_{-1}^1 G_n(x) G_m(x) dx = \delta(n, m). \quad (3.99)$$

The three term recurrence relation for the Gram-Schmidt synthesis is [13]

$$g_n = 2\alpha_{n-1}x \circ g_{n-1}(x) - \frac{\alpha_{n-1}}{\alpha_{n-2}}g_{n-2}, \quad (3.100)$$

whereby,

$$\alpha_{n-1} = \frac{m}{n} \left(\frac{n^2 - 1/4}{m^2 - n^2} \right)^{1/2} \quad (3.101)$$

and

$$g_0(x) = 1, \quad g_{-1}(x) = 0 \quad \text{and} \quad \alpha_{-1} = 1. \quad (3.102)$$

The nodes for the Gram polynomials are equally spaced according to,

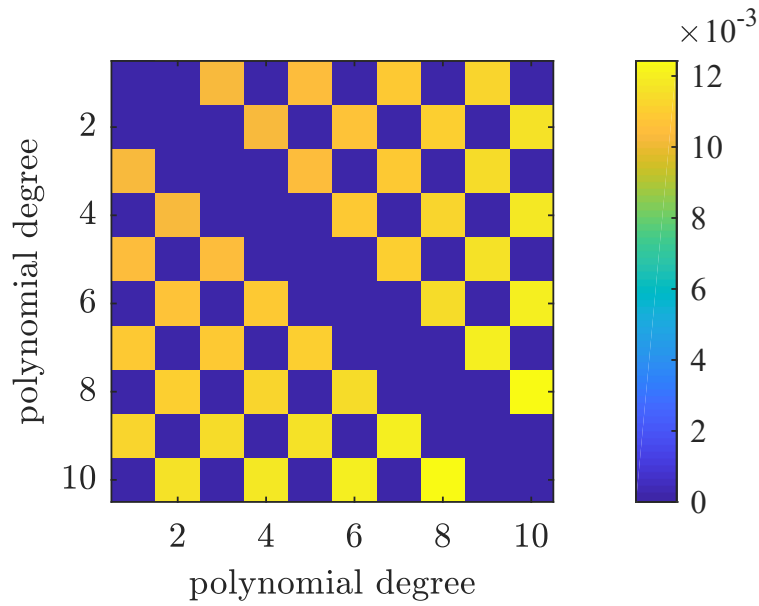


Fig. 3.12 The residual matrix $R = B^T B - \text{diag}(B^T B)$ for the Legendre polynomials of degree $d = 10$, computed for $n = 100$ nodes. R is scaled by the first entry of the diagonal of $B^T B$.

$$x = -1 + \frac{(2k-1)}{m}, \quad 1 \leq k \leq m. \quad (3.103)$$

Note that they do not span the full range of $[+1, -1]$. Figure 3.13 shows the first eight Gram-Schmidt basis functions. The first basis function is scaled by the scaling factor of $\hat{g}_0 = \frac{1}{\sqrt{nr.nodes}}$ and the polynomials of a higher rank are normalised by

$$\hat{g}_n = \frac{\mathbf{g}_n}{\|\mathbf{g}_n\|}. \quad (3.104)$$

The residual matrix R for the Gram-Schmidt polynomials is shown in Figure 3.14

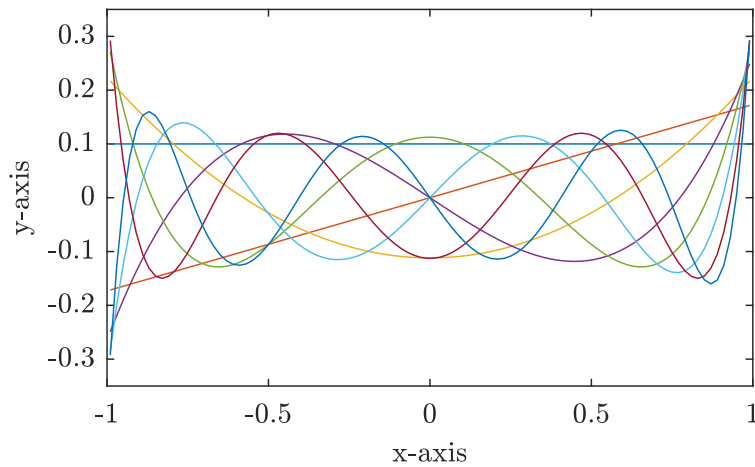


Fig. 3.13 The first eight Gram-Schmidt polynomials.

for $n = 100$ points and degree $d = 10$.

The error in \mathbf{R} is significantly lower than the residual error of the Legendre polynomials but the significant digits are with 10^{-13} . Compared to the computational accuracy available, the eps^1 for the double number 1.0 is $e = 2.2204 \times 10^{-16}$ in Matlab[®] [40] this accuracy is still three digits poorer.

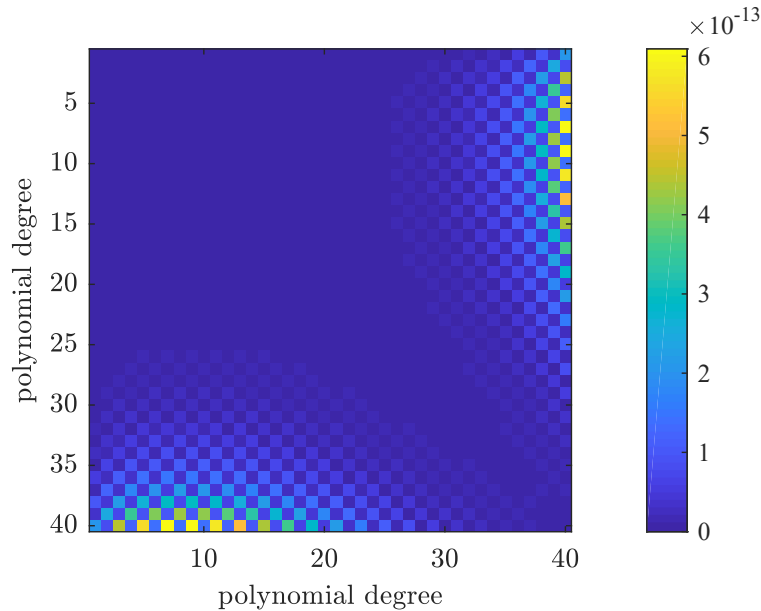


Fig. 3.14 The residual matrix $\mathbf{R} = \mathbf{B}^T \mathbf{B} - \text{diag}(\mathbf{B}^T \mathbf{B})$ for the Gram-Schmidt polynomials of degree $d = 40$. \mathbf{R} is scaled by the first entry of the diagonal of $\mathbf{B}^T \mathbf{B}$.

3.4.2 Discrete Orthonormal Polynomials (DOP)

All common methods for synthesising an orthogonal or orthonormal polynomial basis use the three term recurrence relationship:

$$\mathbf{p}_n = \alpha_n \mathbf{x} \circ \mathbf{p}_{n-1} + \beta_n \mathbf{p}_{n-2}. \quad (3.105)$$

As stated before, using different terms for α and β yield different bases. The three term recurrence relation results in unstable processes, since not all prior terms are taken into account and also round-off errors effect the result. This makes it almost impossible to synthesize polynomial basis functions of higher degree with this three term recurrence formulation.

O’Leary [44] published a universal synthesis algorithm to synthesize a polynomial basis which is truly orthonormal (unitary) and that this is the only method to yield

¹The floating-point relative accuracy (eps) is the difference from a number to the next available number in a system. It is depending on the base number and the number format used (single or double).

a perfect orthonormal polynomial basis. Compared to Equation 3.105 the recurrence relationship can be formulated more generally as,

$$\mathbf{p}_n = \alpha_n \mathbf{x} \circ \mathbf{p}_{n-1} + \mathbf{P}_c \boldsymbol{\beta}_n, \quad (3.106)$$

whereby the complete polynomial basis of degree $n - 1$ is contained in the matrix \mathbf{P}_c . Performing orthogonalisation by projecting \mathbf{p}_n onto \mathbf{P}_c ensures that the n^{th} basis function is also orthogonal to all basis functions of lower degree,

$$\mathbf{p}_n^\perp = (\mathbf{I} - \mathbf{P}_c \mathbf{P}_c^+) \{ \alpha_n \mathbf{x} \circ \mathbf{p}_{n-1} + \mathbf{P}_c \boldsymbol{\beta}_n \}. \quad (3.107)$$

Expanding Equation 3.107 yields,

$$\mathbf{p}_n^\perp = \alpha_n (\mathbf{I} - \mathbf{P}_c \mathbf{P}_c^+) \mathbf{x} \circ \mathbf{p}_{n-1} + (\mathbf{I} - \mathbf{P}_c \mathbf{P}_c^+) \mathbf{P}_c \boldsymbol{\beta}_n \quad (3.108)$$

The fact that the projection of \mathbf{P}_c onto its own orthogonal complement must be zero, i.e. $(\mathbf{I} - \mathbf{P}_c \mathbf{P}_c^+) \mathbf{P}_c = 0$ indicates, that the synthesis of a unitary basis is independent of $\boldsymbol{\beta}_n$.

The remaining polynomial,

$$\mathbf{p}_n^\perp = \alpha_n (\mathbf{I} - \mathbf{P}_c \mathbf{P}_c^+) \mathbf{x} \circ \mathbf{p}_{n-1}, \quad (3.109)$$

is normalised by,

$$\hat{\mathbf{p}}_n^\perp = \frac{\mathbf{p}_n^\perp}{\|\mathbf{p}_n^\perp\|_2} = \frac{\alpha_n (\mathbf{I} - \mathbf{P}_c \mathbf{P}_c^+) \mathbf{x} \circ \mathbf{p}_{n-1}}{\sqrt{\alpha_n^2 (\mathbf{x} \circ \mathbf{p}_{n-1})^T (\mathbf{I} - \mathbf{P}_c \mathbf{P}_c^+) (\mathbf{x} \circ \mathbf{p}_{n-1})}} \quad (3.110)$$

to ensure a unitary basis which is perfectly conditioned. The term $\alpha_n / \sqrt{\alpha_n^2}$ is a sign function, hence α_n is cancelled out of Equation 3.110:

$$\hat{\mathbf{p}}_n^\perp = \frac{(\mathbf{I} - \mathbf{P}_c \mathbf{P}_c^+) \mathbf{x} \circ \mathbf{p}_{n-1}}{\sqrt{(\mathbf{x} \circ \mathbf{p}_{n-1})^T (\mathbf{I} - \mathbf{P}_c \mathbf{P}_c^+) (\mathbf{x} \circ \mathbf{p}_{n-1})}}. \quad (3.111)$$

Both, α and $\boldsymbol{\beta}$, are not used for the generation of the one existing polynomial basis that is perfectly conditioned. This generation process is performed incrementally where after each iteration the existing basis $\mathbf{P}_c \hat{=} \mathbf{P}_{n-1}$ is augmented with the newly generated orthonormal basis $\hat{\mathbf{p}}_n^\perp$,

$$\mathbf{P}_n = [\mathbf{P}_c, \hat{\mathbf{p}}_n^\perp]. \quad (3.112)$$

This synthesis can be split into two parts, an *initial step* and afterwards an *incremental process*. The initial step consists of the generation of the first two basis functions. \mathbf{p}_0 is a column vector of m ones scaled by $m^{-\frac{1}{2}}$.

\mathbf{p}_1 represents the centralised and normalised x vector,

$$\mathbf{p}_0 = \frac{\mathbf{1}}{\sqrt{m}} \quad \text{and} \quad \mathbf{p}_1 = \frac{\mathbf{x} - \bar{x}}{\|\mathbf{x} - \bar{x}\|_2}. \quad (3.113)$$

After the generation of the first two basis functions each further function of the next higher degree is synthesised in following steps:

1. Generation of the basis function \mathbf{p}_n of next higher degree

$$\mathbf{p}_n = \mathbf{p}_1 \circ \mathbf{p}_{n-1} \quad (3.114)$$

2. Complete re-orthogonalisation via

$$\mathbf{p}_n^\perp = \left(\mathbf{I} - \mathbf{P}_{n-1}^\top \mathbf{P}_{n-1} \right) \mathbf{p}_n. \quad (3.115)$$

Via re-orthogonalisation of \mathbf{p}_n w.r.t. the complete existing orthonormal basis \mathbf{P}_{n-1} all correlations with the previous basis functions are eliminated.

3. Normalisation of \mathbf{p}_n^\perp via

$$\hat{\mathbf{p}}_n^\perp = \frac{\mathbf{p}_n^\perp}{\|\mathbf{p}_n^\perp\|_2} \quad (3.116)$$

4. Expansion of \mathbf{P}_{n-1} with $\hat{\mathbf{p}}_n^\perp$ to yield the matrix \mathbf{P}_n containing the complete set of basis vectors from \mathbf{p}_0 to \mathbf{p}_n .

$$\mathbf{P}_n = \left[\mathbf{P}_{n-1}, \hat{\mathbf{p}}_n^\perp \right] = \left[\mathbf{p}_0, \mathbf{p}_1, \dots, \hat{\mathbf{p}}_n^\perp \right] \quad (3.117)$$

Figure 3.15 presents the residual matrix for the discrete orthogonal basis functions for degree $d = 500$. The range of 10^{-16} for the significant digits indicates, that the generation of basis functions of a high degree is in the range of the reachable relative floating-point accuracy of current implementations of IEEE standard floating point representations in hard- and software [2].

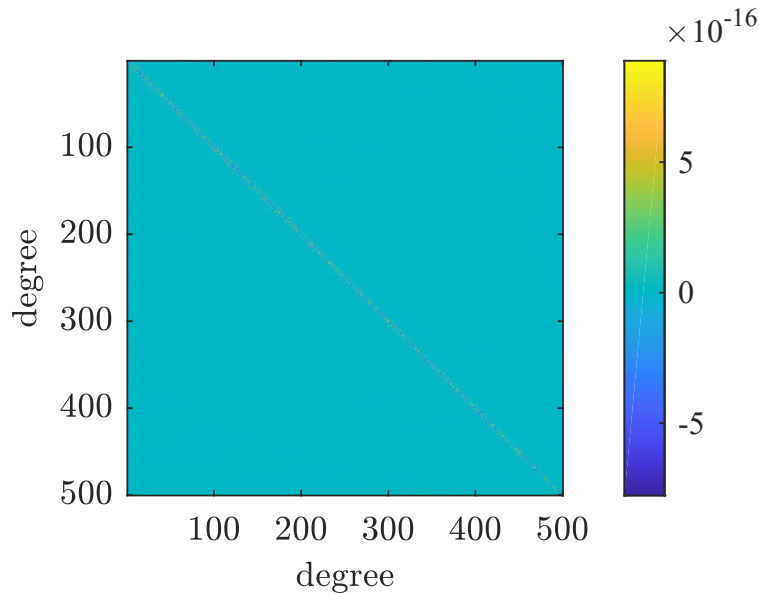


Fig. 3.15 The residual matrix $\mathbf{R} = \mathbf{B}^\top \circ \mathbf{B} - \text{diag}(\mathbf{B}^\top \circ \mathbf{B})$ for a discrete orthogonal polynomial of degree $d = 500$. The residual error is in the magnitude of the floating-point relative accuracy (eps) available in the calculating system.

3.4.3 Derivatives of Discrete Orthonormal Polynomials

For synthesising the basis functions for a vector \mathbf{x} just fundamental linear algebra is used. For solving ordinary differential equations (ODE) and partial differential equations (PDE) also the derivative of \mathbf{p}_n is needed.

While \mathbf{p}_n is synthesised via Equation 3.106 the derivative \mathbf{p}'_n can be synthesised by the recurrence relation,

$$\mathbf{p}'_n = \alpha_n (\mathbf{p}'_{n-1} \circ \mathbf{x} + \mathbf{p}_{n-1} \circ \mathbf{x}') + \mathbf{P}_{n-1} \beta_n. \quad (3.118)$$

These derivatives are concatenated to the matrix $\mathbf{P}' = [\mathbf{p}'_0, \mathbf{p}'_1, \dots, \mathbf{p}'_n]$. These basis functions are not orthogonal. But extending the algorithm to synthesize the basis functions, including complete re-orthogonalisation, results in a marginal additional computational effort. Moreover, the algorithm to compute the derivatives, can easily be implemented into the framework to compute the discrete orthogonal basis.

The numerical derivative \mathbf{y}' of a vector \mathbf{y} can be computed via the differential matrix \mathbf{D} as,

$$\mathbf{y}' = \mathbf{D} \mathbf{y}. \quad (3.119)$$

\mathbf{D} is a linear differential operator and is required for solving various kinds of problems like Boundary Value Problems (BVP) or Initial Value Problems (IVP). The quality of the linear differential operator affects the accuracy of the solution to the mathematical problem directly. The relation between the basis functions, their derivatives and the linear differential operator is,

$$\mathbf{P}' = \mathbf{D} \mathbf{P}. \quad (3.120)$$

Differential matrices are generally rank-1 deficient, but if computed for a high degree and high number of points they become more degenerate what results in an increasing condition number $\kappa = \text{cond}(\mathbf{D})$. This affects the solution of inverse problems negatively; thus, a regularising differential operator $\hat{\mathbf{D}}$ is introduced, which is defined as,

$$\hat{\mathbf{D}} \triangleq \mathbf{P}'_m \mathbf{P}_m^T = \mathbf{D} \mathbf{P}'_m \mathbf{P}_m^T. \quad (3.121)$$

In this case \mathbf{P}_m is a truncated subset of the basis functions containing just the first m basis vector sets. Using a regularising linear differential operator reduces the numerical effort and stabilises the solution with respect to present noise. This type of regularisation is called spectral regularisation.

For the cost function of a differential equation,

$$\epsilon = \| \mathbf{D} \mathbf{y} - \mathbf{y}' \|_2^2, \quad (3.122)$$

the solution, in a least square manner for the estimate $\hat{\mathbf{y}}$ w.r.t. \mathbf{y} , is,

$$\hat{\mathbf{y}} = \mathbf{D}^+ \mathbf{y}' + \text{null}(\mathbf{D}) \gamma. \quad (3.123)$$

In this solution $\text{null}(\mathbf{D}) \gamma$ represents the appropriate null-space for the problem. The null-space is a subset of the vector base for an inverse problem, whereby this subset is not influencing the solution since it is orthonormal to all other solutions. The null-space is, depending of the rank deficiency scaled by a scalar or vector and can be compared to the constant of integration. If the numerical variational integrator \mathbf{D}^+ is numerically perfectly conditioned the null space is a vector of ones,

$$\text{null}(\mathbf{D}) \gamma = \gamma \mathbf{1}. \quad (3.124)$$

Regularisation for this type of problems is not limited to spectral regularisation, e.g. also Tikhonov regularisation [35] could be used by implementing an additional penalty term to the cost function [29],

$$\epsilon_{Tikhonov} = \| \mathbf{D} \mathbf{y} - \mathbf{y}' \|_2^2 + \lambda \| \mathbf{S} \mathbf{y} \|_2^2. \quad (3.125)$$

The penalty term of the Tikhonov regularisation penalizes outliers according to the regularising parameter λ . A combination of spectral and Tikhonov regularisation is described in [46].

As mentioned before a differential matrix should be rank-1 deficient but when they are computed for high degrees the condition number increases and they start having additional null-spaces. If they are stabilised by computing the regularised differential matrix $\hat{\mathbf{D}}$ according to Equation 3.121, they are stable up to degree $d = 33$, see Figure 3.16.

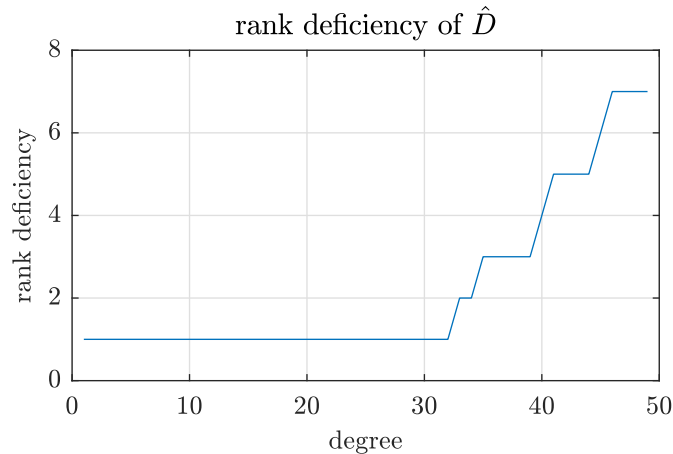


Fig. 3.16 Rank deficiency of the differential matrix $\hat{\mathbf{D}}$ computed according Equation 3.121 regarding to the degree of the used basis functions. $\hat{\mathbf{D}}$ is rank-1 deficient up to degree $d = 33$, for higher degrees the differential matrix degenerates and delivers more null-spaces. This is negative for solving inverse problems.

3.4.4 Local Approximation

In Section 3.2.2 the basics of polynomial regression was presented using the full Vandermonde matrix. In addition to this global approximation, where the basis functions are applied to the full length of the support, also a local approximation is possible. The local approximation applies the basis functions of a defined degree d to a limited portion of the data, defined by the support length l_s .

The original approach for local approximation was introduced by Savitzky and Golay [59] as local polynomial approximation to smooth and evaluate the derivatives of noisy spectrometer data. The smoothing used low degree geometric polynomials of a limited length. Due to the numerical instability of the approximation using Vandermonde polynomials this approach can be improved by using orthogonal basis functions instead of geometric polynomials, see [45].

The process of generating a local approximating matrix can be split up to following steps:

1. A unitary base \mathbf{G} for $m = l_s$ elements of degree d has to be synthesised. This base is unitary ($\mathbf{G}^T \mathbf{G} = \mathbf{I}$) and incomplete since $d < (l_s - 1)$.

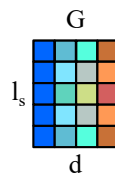


Fig. 3.17 Unitary base \mathbf{G} as starting point for local approximation.

2. From \mathbf{G} the local projection matrix $\mathbf{P} = \mathbf{G} \mathbf{G}^T$ is computed. The centre row p_c of this matrix represents the projection at the centre of the support. The upper rows (p_s) and lower rows (p_e) of the centre row in the matrix correspond to the projection of the data on the basis functions at the start and end of the data. These rows are, in contrast to the centre row, asymmetric because the signal at both ends could not be modelled perfectly. This fact is responsible for a Gibbs error at the end parts of local approximations.

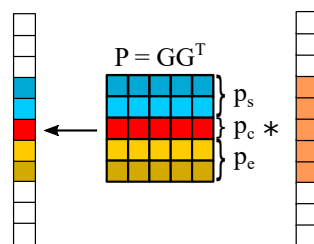


Fig. 3.18 Local projection matrix $\mathbf{P} = \mathbf{G} \mathbf{G}^T$

3. From the local projection matrix \mathbf{P} a global complete projection matrix $\bar{\mathbf{P}}$ is generated, whereby $\bar{\mathbf{P}}$ is of the dimension to span over all m data points. The core of $\bar{\mathbf{P}}$ is filled up diagonally with the centre row of the local projection matrix \mathbf{P} and at the start and end of the global projection matrix $\bar{\mathbf{P}}$ the top and the bottom lines of \mathbf{P} are placed.

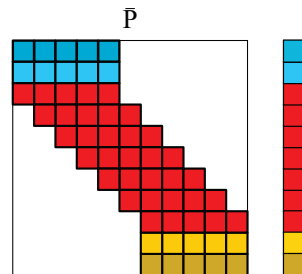


Fig. 3.19 Global complete projection matrix $\bar{\mathbf{P}}$, whereby $\bar{\mathbf{P}}$ is of the dimension to span over all given data points m .

The progress of local polynomial approximation becomes numerically intensive for large data sets. An alternative would be to generate a large matrix with a local approximation term around the trace of the matrix. This approximation term could alternatively be used as kernel for a convolution operation for the middle data sets, whereby the beginning or ending datasets have to be handled separately. This reduces the computational effort significantly. If local approximation is applied to time-series data instead of spatial data, this time-series data is streamed and therefore it has no real beginning or ending part. This aspect is important in data analytics where huge datasets over long periods of time are available, see [27, 47, 56].

3.4.5 Linear Differential Operator

As described in Chapter 3 in monitoring of structures inclinometers are often used. These inclination sensors measure the slope at a specific point on the observed object. This inclination is the first derivative of the deflection of the structure. The deformation of the structure is described by differential equations, e.g. in the case of a beam the Euler-Bernoulli equation,

$$\frac{d^4 y(x)}{dx^4} - \lambda y(x) = 0. \quad (3.126)$$

The goal is to reconstruct the deflection of the beam from the measured perturbed inclination values. This class of problem is an inverse problem, see Section 3.2, where, via a mathematical model for the structure, the output data is used to define the input, which is causing the deformation.

A Linear Differential Operator (LDO) has to be defined to enable the computation of the inverse solution. This concept using the LDO is not just suitable for

inclinometer measurements, that are related to a spacial domain, but also suitable for measurements in the temporal domain, e.g. accelerometer measurements.

In Chapter 3.4.2 the synthetisation of a set of discrete orthogonal polynomials \mathbf{B} and in Chapter 3.4.3 the generation of their derivative $\dot{\mathbf{B}}$ is described. The relation between \mathbf{B} and $\dot{\mathbf{B}}$ is,

$$\dot{\mathbf{B}} = \mathbf{D} \mathbf{B}. \quad (3.127)$$

Both sides are multiplied with the Moore-Penrose pseudo-inverse \mathbf{B}^+ of \mathbf{B} to compute the differential operator \mathbf{D} .

$$\dot{\mathbf{B}} \mathbf{B}^+ = \mathbf{D} \mathbf{B} \mathbf{B}^+ \quad (3.128)$$

The vector basis set and their derivatives can be computed for either a

1. complete set of basis functions, \mathbf{B} and $\dot{\mathbf{B}}$ or
2. an incomplete vector basis set, \mathbf{B}_r and $\dot{\mathbf{B}}_r$.

For a complete set of basis functions:

$$\mathbf{B} \mathbf{B}^T = \mathbf{I}, \quad (3.129)$$

and applying this to Equation 3.128 yields \mathbf{D} computed as,

$$\mathbf{D} = \dot{\mathbf{B}} \mathbf{B}^+. \quad (3.130)$$

\mathbf{D} is a non regularising differential operator with rank-1 deficiency. Hence the null-space $\mathbf{N}_{\mathbf{D}}$ of \mathbf{D} is

$$\mathbf{N}_{\mathbf{D}} = \mathbf{1} \gamma, \quad (3.131)$$

whereby γ is a scalar. The linear differential operator can now be defined as $\mathbf{A} = \mathbf{D}^+$. The resulting matrix equation for solving the inverse problems of inclinometer measurements is now defined as,

$$\mathbf{y} = \mathbf{A} \dot{\mathbf{y}} + \mathbf{N}_{\mathbf{D}} \gamma, \quad (3.132)$$

whereby $\mathbf{N}_{\mathbf{D}} \gamma$ is comparable with the constant of integration.

If a reduced number of basis functions are used for generating the orthogonal vector basis set \mathbf{B}_r and $\dot{\mathbf{B}}_r$, the regularising differential matrix can be defined as,

$$\mathbf{D}_r \triangleq \dot{\mathbf{B}}_r \mathbf{B}_r^+ = \mathbf{D} \mathbf{B}_r \mathbf{B}_r^+. \quad (3.133)$$

The differential operator \mathbf{D}_r is not suitable for solving inverse problems but the projection

$$\hat{\mathbf{y}} = \mathbf{D} \mathbf{B}_r \mathbf{B}_r^+ \tilde{\mathbf{y}} \quad (3.134)$$

implies a smoothing during the derivation or integration.

This regularising differential matrix enables a high degree global smoothing for inverse problems. In geo-monitoring, where data from displacement sensors and inclination sensors, which indicate the first derivative of the displacement, have to be combined, this approach enables more stable solutions where the effect of single outliers in the data is reduced.

3.4.6 Basis Function Approximation with Constraints

Discrete orthogonal polynomials are also suitable for solving initial value or boundary value problems with constraints, e.g. inclinometer measurements with constraining reference measurements. This type of problem belongs to the family of ordinary differential equations (ODE).

The m measurement values corresponding to discrete samples of a continuous forcing function $z(x)$ are forming the vector \mathbf{z} . In the case of inclinometer measurements the positions of the sensors define the location vector \mathbf{x} .

Note that the presented method is also applicable for time series data, where the time points of the individual measurements define \mathbf{x} .

As described in Chapter 3.3 in a system where a-priori knowledge is available constraints can be defined. These constraints can correspond to known zeros ($y(c_i) = 0$), to value pairs of the function ($y(c_i) = a_i$) or to a derivative of the function of grade k on known positions ($y^{(k)}(c_i) = a_i$). Dirichlet and Neumann boundary conditions are a special case of such generalised conditions as they appear in initial value (IVP) or boundary value problems (BVP).

To compute a numerical solution for a specific problem with constraints it is necessary to approximate the function by a continuous function, e.g. a polynomial, which fulfils the constraints. Discrete orthonormal polynomials are better suitable for a stable solution, compared to polynomials with a Vandermonde basis, since computing the inverse of the design matrix is more stable and efficient.

For the reconstruction of perturbed inclination measurements the algebraic model for the problem is defined as,

$$\mathbf{y} = \mathbf{L} \dot{\mathbf{z}}, \quad (3.135)$$

whereby the disturbed measurement values are in the vector $\dot{\mathbf{z}}$ and \mathbf{L} represents the discrete linear differential operator defined as,

$$\mathbf{L} \triangleq \mathbf{A}_n \mathbf{D}_n + \mathbf{A}_{n-1} \mathbf{D}_{n-1} + \mathbf{A}_1 \mathbf{D} + \mathbf{A}_0. \quad (3.136)$$

This problem is an inverse problem [65] that is ill-posed, because it covers multiple solutions. To solve this problem the residuum r ,

$$\mathbf{r} = \mathbf{L} \mathbf{y} - \mathbf{z}, \quad (3.137)$$

has to be minimised yielding least square solution resulting in the definition of the cost function $K = \|\mathbf{r}\|_2^2 = \|\mathbf{r}^T \mathbf{r}\|_2$ as,

$$K = \|\mathbf{L} \mathbf{y} - \mathbf{z}\|_2^2. \quad (3.138)$$

To ensure a unique solution to the problem, constraints must be imposed on the system. The constraints, that are gathered by boundary conditions and/or reference measurements e.g. optical reference measurements², are modelled by,

$$\mathbf{C}^T \mathbf{y} = \mathbf{d}, \quad (3.139)$$

whereby \mathbf{C}^T is the matrix of constraints and \mathbf{d} the vector with the values of the corresponding constraints. In this form the physical structure of the observed system is described.

The description of the system via an incomplete set of orthogonal basis functions \mathbf{B} of degree d is related with the coefficients $\boldsymbol{\alpha}$ via,

$$\mathbf{y} = \mathbf{B} \boldsymbol{\alpha}. \quad (3.140)$$

The basis functions \mathbf{B} are related with the eigenfunctions of the structure being monitored, whereby in this case they deliver the deformed curve based on the modes of the structure. The use of an incomplete set of discrete orthogonal polynomials results in a form of spectral regularisation.

The most general solution of the inverse problem is yielded by substituting $\mathbf{y} = \mathbf{B} \boldsymbol{\alpha}$ in $\mathbf{C}^T \mathbf{y} = \mathbf{d}$ resulting in,

$$\mathbf{C}^T \mathbf{B} \boldsymbol{\alpha} = \mathbf{d}. \quad (3.141)$$

An estimate for $\hat{\boldsymbol{\alpha}}$ for the coefficients $\boldsymbol{\alpha}$ of Equation 3.141 is given by,

$$\hat{\boldsymbol{\alpha}} = \{\mathbf{C}^T \mathbf{B}\}^+ \mathbf{d} + \mathbf{N} \boldsymbol{\gamma}, \quad (3.142)$$

where $\{\mathbf{C}^T \mathbf{B}\}^+$ is the pseudo-inverse of the least square solution, \mathbf{N} the orthonormal null space of $\{\mathbf{C}^T \mathbf{B}\}^+$ and $\boldsymbol{\gamma}$ the coefficients corresponding to the null space \mathbf{N} . Substituting this estimate into Equation 3.140 yields the curve estimate $\hat{\mathbf{y}}$,

$$\hat{\mathbf{y}} = \mathbf{B} \{\mathbf{C}^T \mathbf{B}\}^+ \mathbf{d} + \mathbf{B} \mathbf{N} \boldsymbol{\gamma}. \quad (3.143)$$

Expanding the cost function, Equation 3.138, with this estimate

$$K = \|\mathbf{L} \mathbf{B} \{\mathbf{C}^T \mathbf{B}\}^+ \mathbf{d} + \mathbf{L} \mathbf{B} \mathbf{N} \boldsymbol{\gamma} - \mathbf{z}\|_2^2 \quad (3.144)$$

²optical reference measurements with robotic total stations are assumed to be true in geotechnical applications

solved for γ in a least square sense yields,

$$\gamma = \{\mathbf{LBN}\}^+(\mathbf{z} - \mathbf{LB}\{\mathbf{C}^T\mathbf{B}\}^+\mathbf{d}). \quad (3.145)$$

The substitution of γ into Equation 3.142 yields

$$\hat{\alpha} = \{\mathbf{C}^T\mathbf{B}\}^+\mathbf{d} + \mathbf{N}\{\mathbf{LBN}\}^+(\mathbf{z} - \mathbf{LB}\{\mathbf{C}^T\mathbf{B}\}^+\mathbf{d}), \quad (3.146)$$

and using this estimation for the coefficient $\hat{\alpha}$ in Equation 3.140 yields the final solution for $\hat{\mathbf{y}}$,

$$\hat{\mathbf{y}} = \underbrace{\mathbf{B}\{\mathbf{C}^T\mathbf{B}\}^+\mathbf{d}}_{\mathbf{K}} + \underbrace{\mathbf{BN}\{\mathbf{LBN}\}^+}_{\mathbf{P}}(\mathbf{z} - \underbrace{\mathbf{LB}\{\mathbf{C}^T\mathbf{B}\}^+}_{\mathbf{K}}\mathbf{d}), \quad (3.147)$$

for easier reading it is defined,

$$\mathbf{K} = \mathbf{B}\{\mathbf{C}^T\mathbf{B}\}^+ \quad \text{and} \quad \mathbf{P} = \mathbf{BN}\{\mathbf{LBN}\}^+. \quad (3.148)$$

Substituting these terms in Equation 3.147 yields,

$$\hat{\mathbf{y}} = \mathbf{K}\mathbf{d} + \mathbf{P}(\mathbf{z} - \mathbf{LK}\mathbf{d}) \quad (3.149)$$

$$= \mathbf{K}\mathbf{d} + \mathbf{P}\mathbf{z} - \mathbf{PLK}\mathbf{d}. \quad (3.150)$$

Partitioning this equation for \mathbf{d} and \mathbf{z} yields,

$$\hat{\mathbf{y}} = (\mathbf{K} - \mathbf{PLK})\mathbf{d} + \mathbf{P}\mathbf{z} \quad (3.151)$$

$$= (\mathbf{I} - \mathbf{PL})\mathbf{K}\mathbf{d} + \mathbf{P}\mathbf{z}, \quad (3.152)$$

whereby the multiplicand of \mathbf{d} is defined as,

$$\mathbf{H} \triangleq (\mathbf{I} - \mathbf{PL})\mathbf{K}. \quad (3.153)$$

With this definition Equation 3.151 is rewritten in the form,

$$\hat{\mathbf{y}} = \mathbf{H}\mathbf{d} + \mathbf{P}\mathbf{z}. \quad (3.154)$$

In this form the term $\mathbf{y}_h = \mathbf{H}\mathbf{d}$ represents the homogeneous solution and $\mathbf{y}_p = \mathbf{P}\mathbf{z}$ the particular solution.

$$\mathbf{y} = \mathbf{y}_h + \mathbf{y}_p \quad (3.155)$$

In this generalised solution for this type of problems, the vectors \mathbf{d} and \mathbf{z} are variable, while the matrices \mathbf{H} and \mathbf{P} are defined by the specific problem. Thus, the matrices \mathbf{H} and \mathbf{P} can be computed a priori and computing the homogeneous and particular solution for new \mathbf{d} and \mathbf{z} is done by two efficient matrix multiplications. Therefore, this solution is suitable to be used on low power devices with limited computing power when compared with embedded systems.

3.5 Model Based Reconstruction of Monitoring Data

A suitable construction site was selected to apply the model-based reconstruction on real data.

In this project a new subway line is built underneath the subway station of an existing line. The new tunnel gets excavated while the surrounding metro lines are operated as usual. Therefore, the need for continuous parallel monitoring with short reaction times in case of unpredicted events is mandatory. Figure 3.20 shows the existing station, marked as the long purple area from the left side to the right side. The long thin purple area from top to bottom marks the newly built tunnel.

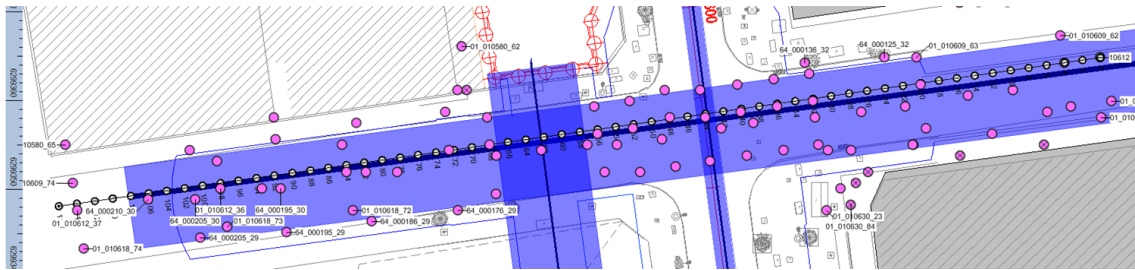


Fig. 3.20 Schematic representation of a complex measurement field associated with the monitoring of a subway tunnel construction. The white circles form a linear chain of 59 inclinometers monitoring a stretch of railway line. The pink circles correspond to reference measurements points acquired from theodolite measurements, © Geodata GmbH.

In such a case the task is the surveillance of the condition of the active tracks and determine if subsidence, deformation or lateral tilt appear. As soon as a deformation occurs that is greater than the expected deformations, an alarm must be triggered promptly.

Commonly the monitoring of the tracks would be done with a total station and reflective targets at the critical positions. The reliability of such a system is high and also the accuracy is sufficient over long distances [14, 28]. Since the rails are used continuously and passengers remain on the platforms, measurements with a robotic total station cannot be carried out without interruptions, since these measurements require the line-of-sight to be free from obstructions.

To ensure continuous monitoring, an inclinometer chain is used and significant reference points are monitored by a total station. In Figure 3.20 the white circles mark the positions of the horizontal inclinometer chain and the pink circles correspond to the positions of the retro reflectors, that are used for 3D displacement measurements carried out with the robotic total station. Furthermore, inclinometers deliver a higher resolution than total stations and are less affected by changes in temperature and air pressure, thus, they are more suitable to determine small changes in tilt and elevation for this application.

A horizontal inclinometer consists of several rigid rods connected to each other by joints and together form a continuous chain. The inclinometers attached to the rods measure the inclination of each individual rod, from which the rod length can be used to determine the settlement of each individual joint. Both ends of an inclinometer chain are located outside of the area where deformations are expected. Therefore the used measurement system was designed with $n = 59$ inclinometers, mounted on rigid rods each of length $l = 2$ m, yielding a measurement chain with total length $l_t = 118$ m. Additionally, $p=13$ retro-reflectors were installed to enable an independent verification of the measurement results emanating from the inclinometers. The retro-reflectors were located at the following nominal points $\mathbf{x} = \{4, 20, 32, 36, 40, 44, 48, 52, 56, 68, 72, 84, 88\}$ [m], each location corresponds to the end of an inclinometer rod. The rods of the inclinometer chain and an end point of the chain with an optical target (retro reflector) for the robotic total station is shown in Figure 3.21.



Fig. 3.21 Photograph of the inclinometer rods (covered with the yellow tape) mounted in a tunnel along the track, © Geodata GmbH.



Fig. 3.22 Photograph of the end of the inclinometer chain (A) together with a retro-reflector (B) for the total station measurements. © Geodata GmbH.

This measurement problem, where the changes in $m = 60$ elevations computed from inclination sensors and additional $n = 12$ optical measurements from a robotic total station corresponds to an over-constrained inverse problem described in Chapter 3.4.

3.5.1 Data Fusion

The data of the inclination sensors were acquired with an automatic data collection system which was set-up to a measurement interval of $t_m = 10$ min. The optical reference measurements were performed daily by workers in place at predetermined times. During these measurements, the subway line was closed to ensure safety.

The inclinometer measurements and the optical measurements use a completely different physical measuring principle. They are therefore completely independent of each other and do not influence each other. Therefore, each individual data source can be used alone for an independent reconstruction. The individual reconstructions are used for mutual validation.

Using a suitable data fusion procedure that combines both datasets enables the computation of the final results with higher precision and an additional validation of the correctness of the sensor data.

For data fusion the inclinometer data is considered to be the more important data source, because the sensors are measured at relatively short intervals and have a higher accuracy than the optical measurements. The data from the theodolite is used to verify the reconstructed data and to identify inconsistencies in the datasets caused by sensor failures or problems with the total station.

To determine the subsidence of the tracks the following computational procedures are performed:

1. Since the inclination measurements have no location or height information the two end points of the inclination measurement m_0, m_{118} are registered in the project coordinate system via the optical measurements of these positions $m_0 = [x_0, d_1]$ and $m_{118} = [x_{118}, d_{118}]$. For a measurement with an in-place inclinometer chain the registration of one point would be sufficient but the registration of two reference points was chosen since this results in an over-constrained reconstruction with one additional constraint more than required. This enables the detection of one defective inclination sensor. Further, a correction for one erroneous sensor can be computed. Given these reference points, the constraint matrix \mathbf{C}_1 and the vector $\mathbf{d}_1^T = [d_1, d_{118}]$ can be formed. The reconstruction is now computed solving:

$$\min_{\mathbf{y}_1} \|\mathbf{D}_i \mathbf{y}_1 - \mathbf{g}\|_2^2, \quad (3.156)$$

$$\text{given } \mathbf{C}_1^T \mathbf{y} = \mathbf{d}_1. \quad (3.157)$$

As far as no inconsistency from a defect sensor or other source is detected this solution can be considered as the correct and final computation procedure.

2. Additionally, to the previously described reconstruction a second one was performed, where all 13 measurements of the total station were used to compute the constraint matrix \mathbf{C}_2 and \mathbf{d}_2 . This extended reference data set results in

more constraining points for the reconstruction which split the inclinometer measurements into segments between each constraining point. Within a single segment the reconstruction is degree one over-constrained for each segment allowing the detection of one defective sensor in each of the twelve segments. This improves the robustness of the system for cases, where defect inclination sensors occur.

3. The difference between the two previously defined reconstructions $\Delta(\mathbf{y}) = \mathbf{y}_1 - \mathbf{y}_2$ should remain constant over time. If the measurements of the total station and the inclinometers diverge, this is an indication that damage has occurred to individual inclinometers, the retro reflectors or the total station. This results in a further level of consistency checking.

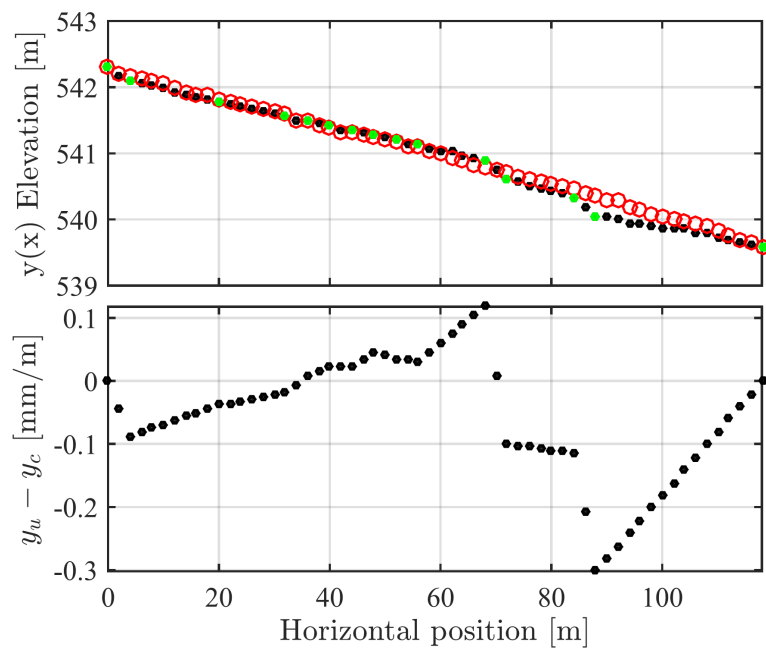


Fig. 3.23 Result of the data fusion of inclinometer and theodolite measurements, top: (red) an unconstrained reconstruction from the inclinometer data. (green) The theodolite reference points and (black) the constrained reconstruction. Bottom: The difference between the constrained and unconstrained reconstruction, [61] © 2016 IEEE.

An example for a measurement with the above reconstructions can be seen in Figure 3.23.

3.5.2 Long-Term Observations

Inclinometer and theodolite data were collected over three months at ten minute intervals. When reconstructing the deformation for this period, no significant height shifts were found. In the data, however, a very small periodic shift of some measurement points is detectable, which is so small that it has no critical effect on the measurement result. Figure 3.24 shows this vertical shift of all sensors of this inclinometer chain for the period of one week.

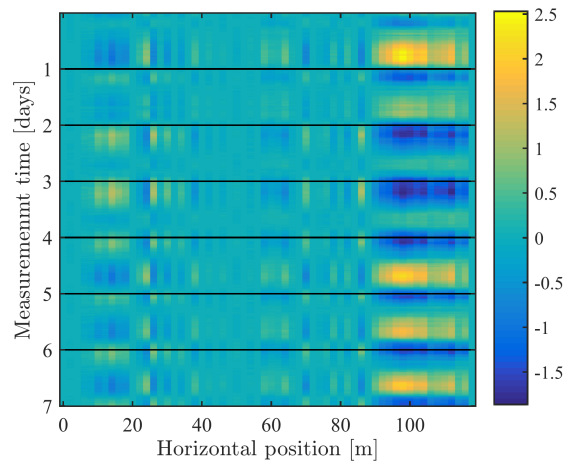


Fig. 3.24 Reconstructions for the 60 elevations, measured with a sampling interval of $t_s = 10$ [min] over a seven day time period. Note that the scaling of the vertical shift is in [$\mu\text{m}/\text{m}$], [61] © 2016 IEEE

A first assumption suggests an origin from daily temperature changes. Looking at the temporal course of the signal of a single sensor, it can be seen that not only a 24-hour cycle is present, but also an influence of another source is predominant. The signal of a single sensor is shown in Figure 3.25.

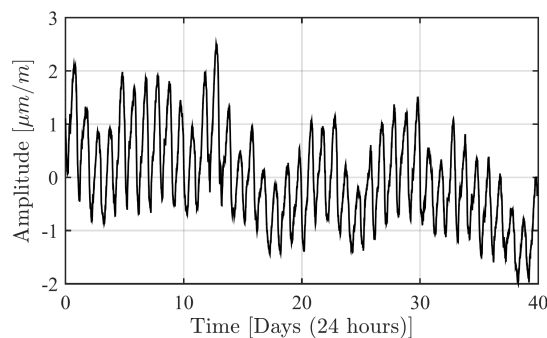


Fig. 3.25 A 40 day observation of the periodic portion of the reconstructed elevation, with the measurement period $t_s = 10$ [min], [61] © 2016 IEEE.

A spectral analysis reveals that there is a coincidence in the frequencies of the periodic signal and the diurnal and half-daily tidal patterns. The two-day pattern has an amplitude smaller than $d_2 < 1$ [$\mu\text{m}/\text{m}$], but is still clearly visible, see Figure 3.26.

The 7- and 14-day patterns are also noticeable in the frequency domain. In addition, there is a residual temperature sensitivity that requires further long-term observation.

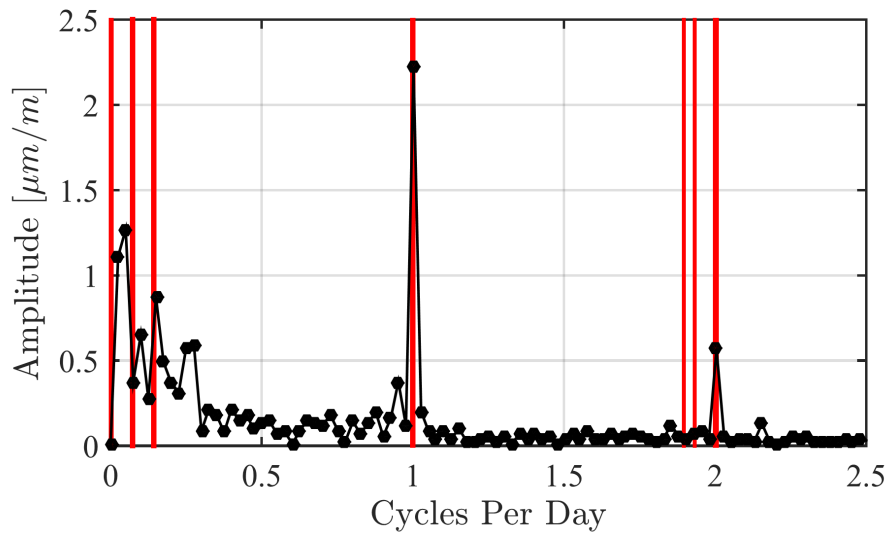


Fig. 3.26 The FFT of the signal from Fig. 3.25. The solid-earth diurnal and semi diurnal tidal modes are marked in red, [61] © 2016 IEEE.

The long term field measurement and model based reconstruction demonstrated, that the data contained enough information to verify that periodically appearing deflections in the inclinometer data could be assigned to solid earth tides. This correlation was not visible in the reconstruction made by trigonometric computations. In addition, it was shown, that the model based reconstruction is a replacement for trigonometric reconstruction of inclinometer data, especially when constraints from the surrounding environment should be considered in the reconstruction.

4 | Future Urban Monitoring Infrastructure

4.1 Distributed Monitoring

In the last years the use of connected sensors and availability of sensor data in real time occurred. This process also applies to the comparatively traditional mining industry. Several years ago it was sufficient to use data loggers that acquired data locally and a local supervisory system stored the data and provided engineers the necessary information on-site for evaluation, e.g. security relevant processes. With the emergence of internet communication technologies, surveillance systems evolved from a localised system to a networked sensor system that is permanently online and transmits sensor data to a server. There, the data is processed and the information obtained is passed on, regardless of location, to responsible persons who interpret the available information.

Nowadays different micro controller units (MCU's) with various configurations are available to enable low-power devices, that are battery driven and powerful enough to enable local computing and permanent internet connection. This is the basis for Internet-of-Things (IoT) devices, which are able to form a self managed intelligent sensor network. In urban areas and municipalities public sensor networks form the backbone for so-called smart cities, where environmental data of urban systems is collected and used to automate processes to improve urban cohabitation.

To meet this trend modern monitoring systems have to fulfil today's demands for interoperable systems. The acquired data of one sensor or a complete system is used by multiple systems for superior control. Therefore, the demand for reliable sensors with a secure connection to various supervisory systems is given.

Modern cloud based monitoring systems for challenging environments have to fulfil several demands in different domains to guarantee a high acceptance. These demands address modularity, security, available interfaces and the stability/robustness of the local devices as well as the possible services that the cloud solution provide. A system for urban automation has different demands than a system for monitoring mines and construction sites. On the one hand the main focus in a Smart City system lies in

the connectivity of various heterogeneous systems with event detection combined with advanced rule processing. On the other hand the focus of monitoring systems for mines and construction sites is the legal and security aspect. Thus, a reliable, continuous, secure and complete monitoring of processes is needed.

In this chapter the implementation of a monitoring system for mines within an urban control system is presented. The whole development of the presented generic platform is part of the Celtic Plus Project "Advanced Sensing for Urban Automation - ASUA".

4.2 The Celtic Plus ASUA Project

The major goal of the project was to develop a framework for various heterogeneous systems used for automating Smart City tasks. The technical focus of the project could be divided into three key elements: constrained devices, communication networks and information management.

To support the development process during the three-year project several demonstrators were developed to show the different aspects of the outcomes of the project and prove the abilities of the framework.

- Water quality monitoring (Rumania);
- Patients health monitoring system for hospitals and nursing homes (Belgium);
- Mine worker health and position monitoring system (Turkey);
- Urban Monitoring Information and Control System - **UrbMics** (Austria).

4.2.1 UrbMics in ASUA

The Austrian Prototype "Urban Monitoring Information and Control System" is a reference system, developed in cooperation between Geodata GmbH and the Chair of Automation, University of Leoben, during the participation in the ASUA project. In the UrbMics environment new approaches for monitoring in mining, tunnelling and structural monitoring in challenging environments are realised and tested.

The Urban Monitoring, Information and Control system consists of edge devices like wired sensors, wireless sensors and gateways as well as a private cloud framework where each part fulfils the demands for an integrated and reliable monitoring system for the rough industrial applications.

Additionally, the edge devices are designed to perform complex tasks in stand-alone modes, where no continuous connections to supervisory systems are possible. Such

complex tasks can be the continuous data acquisition of data from local wired or wireless sensors as well as performing complex computations like solving differential equations. This enables processing of derived values and additional local event processing and alarm triggering.

4.3 Monitoring Devices for Challenging Environments

The monitoring of construction sites for tunnelling or mining requires robust sensors and data acquisition devices. The conditions in such challenging environments are often rough. In Figure 4.1 a construction site in a tunnel is shown, where sensors were mounted next to the working face of a tunnel, which is still under construction. Geotechnical sensors are placed in the tunnel wall, e.g. they are mounted on the steel reinforcing bars, which are covered from shot concrete or boreholes are drilled into the rock and the sensors placed in these boreholes and the borehole grouted. The floor of the tunnel is quite wet and muddy and some rocks from the last blast still lie around while water drops from the ceiling.



Fig. 4.1 Conditions at a tunnelling construction site at the working face.

There are several different types of very specialised sensors available, that are used for monitoring in mining and tunnelling applications. The list of sensors includes extensometers, fibre-optical sensors for stress and temperature measurements, vibrating wire sensors or inclination sensors, but this list is not limited to these examples. These sensors are available in a robust case with IP68, [3], protection class specification and commonly have a bus system to access the data for further automated data processing. Since for some of these sensor types no robust designs

are available, some companies have to develop their own sensor system for suitable monitoring solutions. Since there is no common standard that specifies the bus or protocol used on a construction site there are different heterogeneous data systems in use. Thus, the need for a modular system, that enables the communication with the various monitoring systems and different data interfaces is given.

The automatic data transmission of sensor data on construction sites or in tunnelling has quite specific requirements, since the measuring positions are spread over a wide area and the environmental conditions are often rough (e.g. dirt, dust, mud, especially high/low temperatures, etc.). Additional infrastructure e.g. power supply or network connection is not very good. Figure 4.2 shows the planned measuring points for an urban tunnelling project, whereby the measurement points (coloured circles) are spread over wide urban areas.

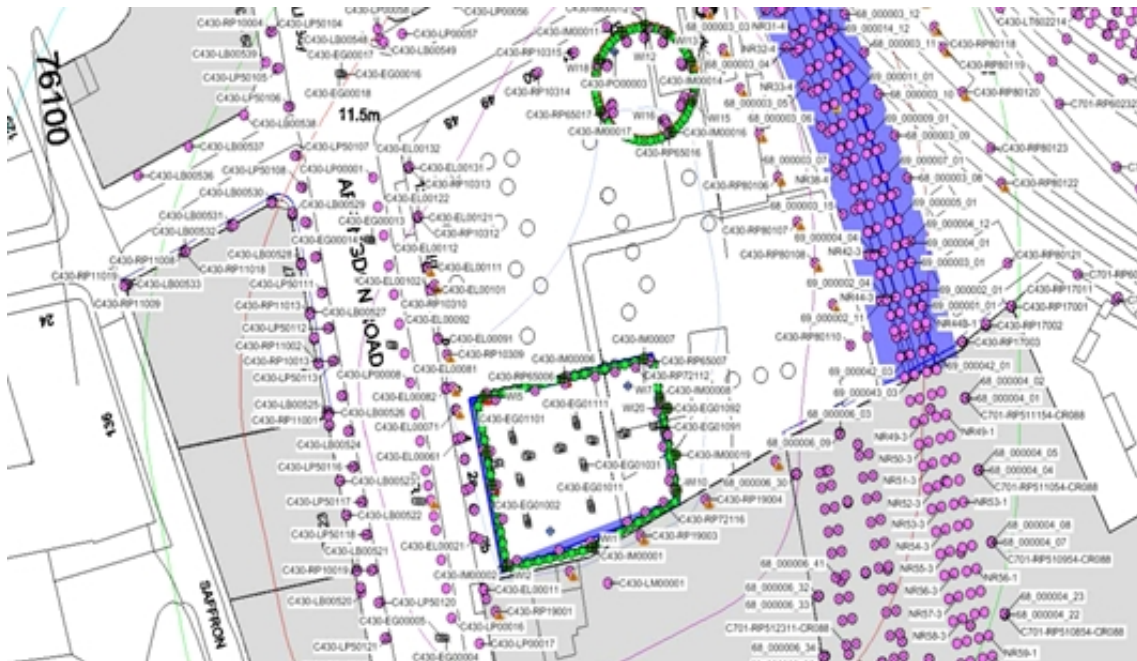


Fig. 4.2 Example for Urban Monitoring: During subsurface construction in urban area the measurement points (purple, green and blue circles) are spread over large urban areas. © Geodata GmbH

For monitoring urban processes with the purpose for urban automation in smart cities, it is essential that the data is provided in real time to responsible officials or third party systems to ensure a seamless operation of different systems in a horizontal manner.

Therefore, it is necessary to provide a system where all the legal issues are satisfied and the provided data of specific types of other third party systems can be found automatically by location, time and further generic characteristics. Further details for storing data online are described in section 4.4.

The wireless measurement node was developed during the work on this PhD thesis

at the Chair of Automation for the ASUA project. The node can be used for data acquisition with local data processing, as local relay station or as generic gateway to different cloud systems.

The node is designed as modular system that can be extended for special purposes. Since this multi-purpose measurement box is part of the UrbMics ecosystem it is commonly called *UrbMics Box*.

The measurement box is equipped with a single-board computer that enables local data processing and performing network management tasks, running a local data storage, triggering alarms or acting as a gateway for further UrbMics Boxes that are connected via a self-organising meshed WiFi.

To withstand the challenging environmental conditions the case of the measurement box is designed robust and watertight, whereby all used outer hardware fulfil the IEC 60529 standard (International Protection Code) IP67. According to the standard the components are designed as dust tight and water tight for 30 [min] to a depth up to 1 [m] [3]. An image of the UrbMics Box is shown in Figure 4.3.



Fig. 4.3 Wireless Measurement Box: A) robust aluminium case B) IP67 antenna for 800MHz to 2.5GHz C) LED-button for triggering predefined actions. D) IP67 Ethernet connector

The embedded system in the wireless measurement box needs a 5 [V] power supply. Since the common power supply on a construction site is 24 [V], a DCDC converter is used for providing all necessary voltage levels in the measurement box. Since the UrbMics Box is able to fulfil various different measurement tasks the hardware

configuration can be customised for the application on hand. The minimum hardware configuration consists of the embedded system, the power supply, the network device and at least one sensor interface. This configuration can be extended by a battery pack for possible power failures and further sensor interfaces, e.g. Bluetooth, Zigbee, LoRa, 433MHz, etc. A system diagram of the UrbMics Box is shown in Figure 4.4.

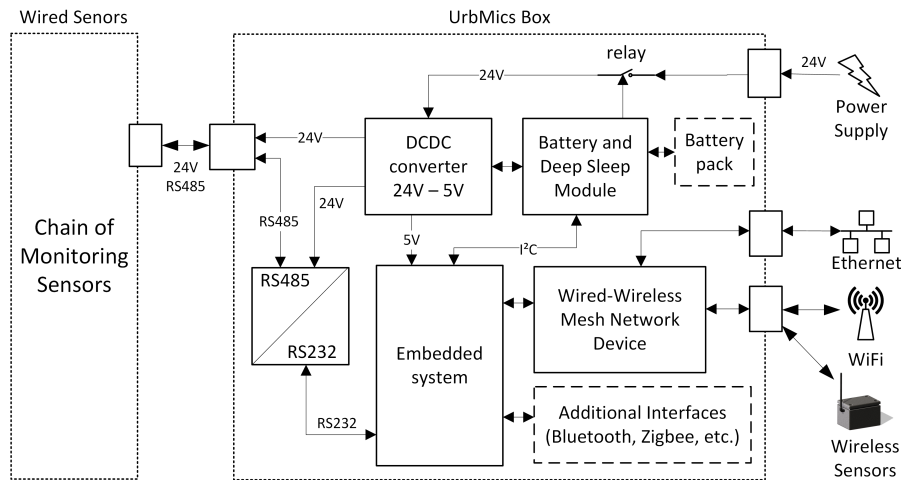


Fig. 4.4 System diagram for one configuration of the Measurement Box.

The wired sensors are connected directly to the UrbMics Boxes via a private RS485 network. This RS485 network allows a communication between the UrbMics Box and multiple attached sensors (over 100 tested) over a distance of at least 500 meters in an electrically noisy environment on a single cable. For communication, the Modbus protocol and the DAMOS protocol from Geodata are implemented, as most wired sensors commonly used for monitoring tasks use these two protocols.

Figure 4.5 shows a picture of the internal hardware of the Wireless Measurement Box.

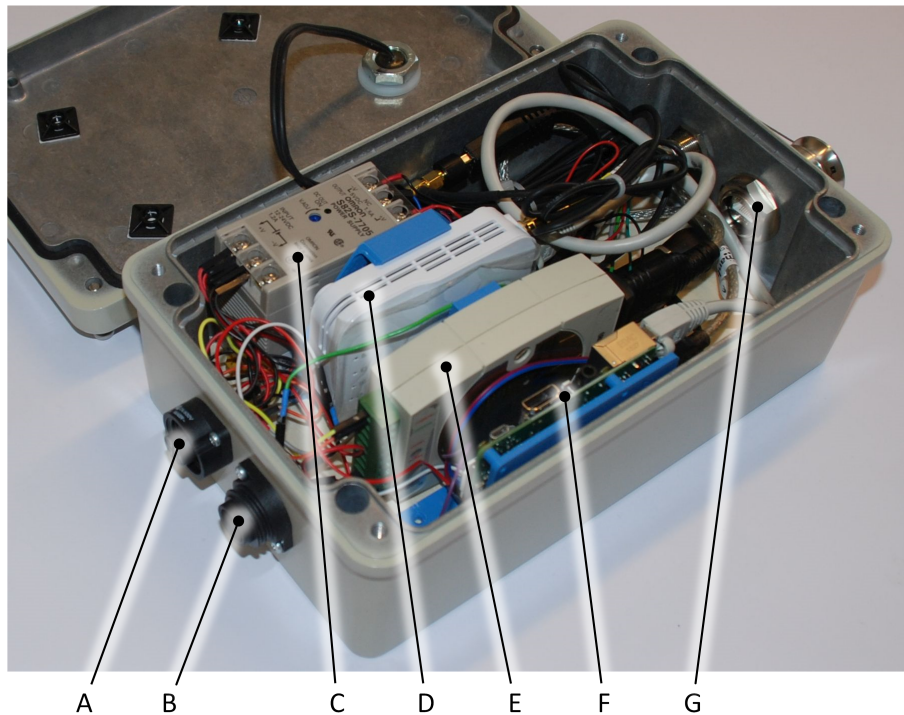


Fig. 4.5 Wireless Measurement Box with hardware for mesh networking; A) RS485 connector B) Power connector C) DC-DC converter D) Network Device E) RS232/RS485 converter F) Embedded device G) IP67 ethernet connector

4.4 Cloud Systems in ASUA

A public cloud system is necessary to provide the data to all further systems in an urban control system. Since each monitoring system is different, not all requirements can be covered by a generic cloud system. A proprietary private cloud may be necessary to support independent operation of the individual systems. Especially as the ideal operating conditions vary between systems and different standards/protocols are used for different technical solutions, e.g. some systems use client-server connections for data transmission, others use a publish and subscribe system. Further reasons for a private cloud are e.g. legal issues; storing raw sensor data in dedicated databases; providing configuration data for the different systems; enabling additional functionalities tailored for a specific monitoring system.

4.4.1 The ASUA Urban Automation Reference Platform

The Urban Automation Reference Platform is the framework for shared data developed within the Celtic Plus ASUA project. It provides the infrastructure for the data, that is used by automated systems in Smart Cities. Before the data is uploaded to the ASUA Cloud, it is converted locally or by a dedicated cloud service

into the final format so that it can be processed by other systems in the ASUA framework. The raw data and data that is not suitable for further processing (e.g. status or configuration data) is stored by private clouds beside the ASUA framework. In the case for the prototype developed by Geodata and the Chair of Automation this private cloud is the UrbMics Center.

The Urban Automation Reference Platform is designed to be a generic cloud system with different core features, e.g. rule processing, event triggering, alert triggering, data storage and data visualisation. The system is designed to allow the extension with new services and provides different application programming interfaces (API's) for third party applications (e.g. mobile phone apps, third party data visualisation) or API's for monitoring systems. The commonly used protocols in the ASUA reference platform are:

1. **RESTful Web Services (RWS)** for client-server data transmission;
2. **Open Geospatial Consortium - Sensor Web Enablement (OGC-SWE)** as a M2M readable data format for spatial and environmental data;
3. **Message Queuing Telemetry Transport (MQTT)** as a lightweight publish and subscribe data transmission protocol;
4. **Simple Network Management Protocol (SNMP)** for organising devices and collecting device information within the ASUA Urban Automation Reference Platform.

This list is not limiting the interfaces for systems in this framework but represents the focussed interfaces.

A graphical overview of the ASUA Urban Automation Reference Platform is shown in Figure 4.6.

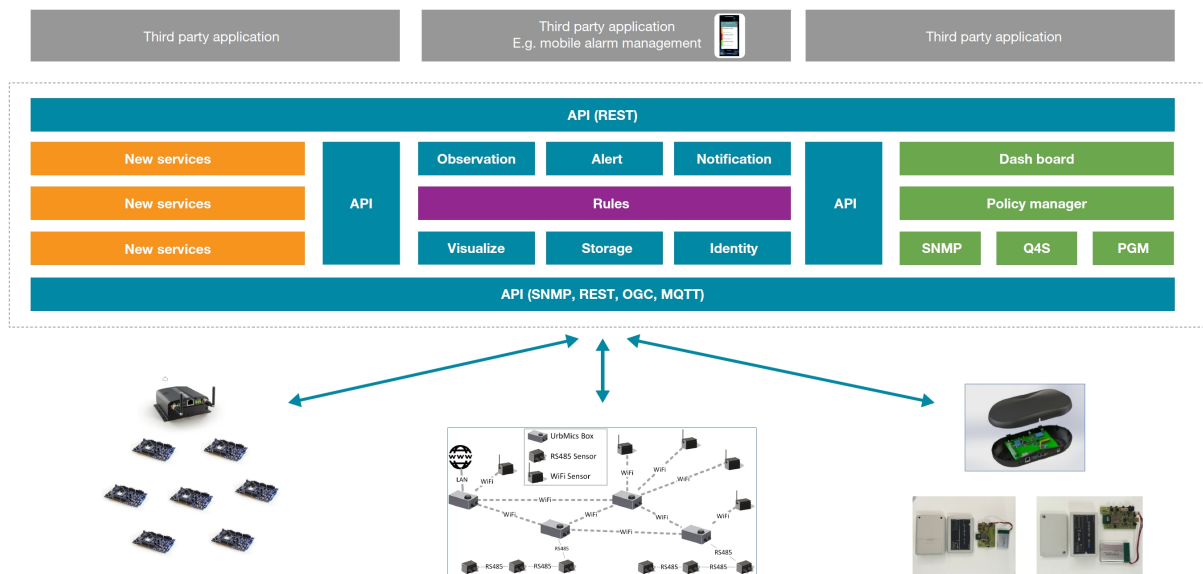


Fig. 4.6 ASUA Urban Automation Reference Platform Architecture: Core capabilities of the cloud framework. The framework is designed to be extendable for additional services and third party applications. Various API's and protocols are implemented for different monitoring and organisational tasks within the framework.

The ASUA Urban Automation Reference Platform is "public", meaning that other systems in this framework can access the sensor data and the associated metadata of these sensors.

4.4.2 UrbMics Centre

As described in Section 4.4.1, there is a need to use a private cloud (server) for several reasons. Since the UrbMic System is used for monitoring geological structures or infrastructure related to construction processes daily reports have to be generated and the raw and processed data has to be stored over long periods for legal issues. Dedicated software is used for data warehousing, data processing, event- and alarm triggering and report generation. For these tasks existing databases, that are reliable, have to be used. Also interfaces to several Geographic Information Systems (GIS) are available, that are not common for urban automation purposes and therefore implemented in the Urban Automation Reference Platform.

4.5 Local UrbMics Network

The counterpart to the cloud system is the local sensor network. A gateway node controls the devices that are used for monitoring on a construction site. It establishes a secure connection to the UrbMics Centre via a VPN connection and also acts as a relay

to transmit data to the ASUA IoT Server or other public cloud services. The gateway provides different services, the most important ones are: a local storage/database, a network time protocol (NTP) server, a Message Queuing Telemetry Transport (MQTT) broker for local communication, a SNMP agent and a mesh Wifi device. In addition, the gateway provides sufficient computational power to enable model based reconstruction as described in Chapter 3 of this thesis. Since the gateway has a modular design it may also be equipped with data acquisition hardware for wired sensors.

The local network commonly does not need a specific measurement box which acts as a gateway, since each wireless measurement box is able to transmit the data directly to the cloud systems. A dedicated gateway is needed in following cases:

1. Local model based reconstruction is performed with the use of data acquired from multiple devices, e.g. two or more wireless measurement boxes are acquiring the data of one structure (e.g. long rails);
2. Use of low-power wireless sensor nodes;
3. The use of wireless communication standards beside WiFi, e.g. LoRa, ZigBee, 6LoWPAN, wireless M-Bus (wM-Bus) or Bluetooth;
4. Local real time event detection and alarm triggering;
5. Offline modes for monitoring tasks where no connection to cloud services is possible (e.g. tunnelling and mining).

The UrbMics gateway provides other wireless measurement boxes with a network (and internet) connection via internal network devices, that span a wireless mesh network between several UrbMics Boxes (Figure 4.7). For the case when no dedicated gateway is needed, at least one of the UrbMics Boxes has to be connected to the internet via ethernet. The meshed network organizes itself and each connected UrbMics Box acts as an access point to this meshed WiFi for low-power wireless sensors nodes in the surrounding area. The data of the low-power sensor nodes is transmitted to the the cloud system via a wireless measurement box in a gateway setup.

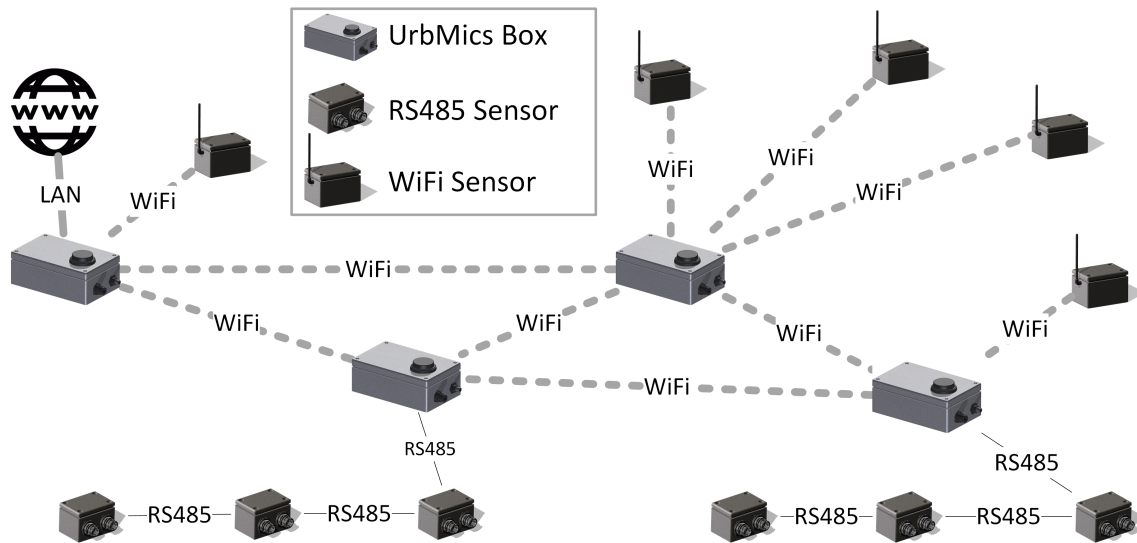


Fig. 4.7 Example for a local monitoring network with wired and wireless sensors [63].

For monitoring structures various sensor systems are available. For measurements over a long period of time most sensors are equipped with an internal data acquisition electronics and the data is provided via a fieldbus system like RS485. Examples for sensors used in mining applications are extensometers (measuring displacements along an axis), inclinometers (measuring displacement perpendicular to an axis), strainmeters or water level gauges. For sensors with no digital interface, e.g. vibrating wire sensors, a suitable data logger with analog digital converters and multiplexer provides the sensor data for the bus system. As bus interface commonly a RS485 network with half-duplex data transmission and Geodata's damos¹ protocol is used. The RS485 interface allows cable length of up to 1200 m and at least 32 devices in a bus-line [4].

In addition to the private RS485 network the CAN-bus is used by some sensors, e.g. magnetostrictive extensometers. The CAN-bus is also robust for data transmission and allows, depending on the bit rate, up to 500 m of cable length [33].

The meshed WiFi is realised by a dedicated additional hardware in the wireless sensor box. The mesh enabled access points establish the connection among each another by themselves. If the connection to one of the wireless sensor boxes in the meshed network is lost, the network reconfigures itself and new connections are established. Each UrbMics Box acts for monitoring sensors with a WiFi interface as a gateway to the meshed wireless network.

¹data acquisition and monitoring system

4.5.1 Handling of the Monitoring Sensor Data

Figure 4.8 shows a general sketch of the relation between the local monitoring devices that generate the data and the two cloud systems, the private and the public one. The first design consideration for the data transmission was, how the data is transmitted to the public cloud. On the one hand it is possible to transmit the sensor data directly or indirectly, whereby the data is forwarded from the private cloud (UrbMics Center) to the public one (ASUA IoT Server).

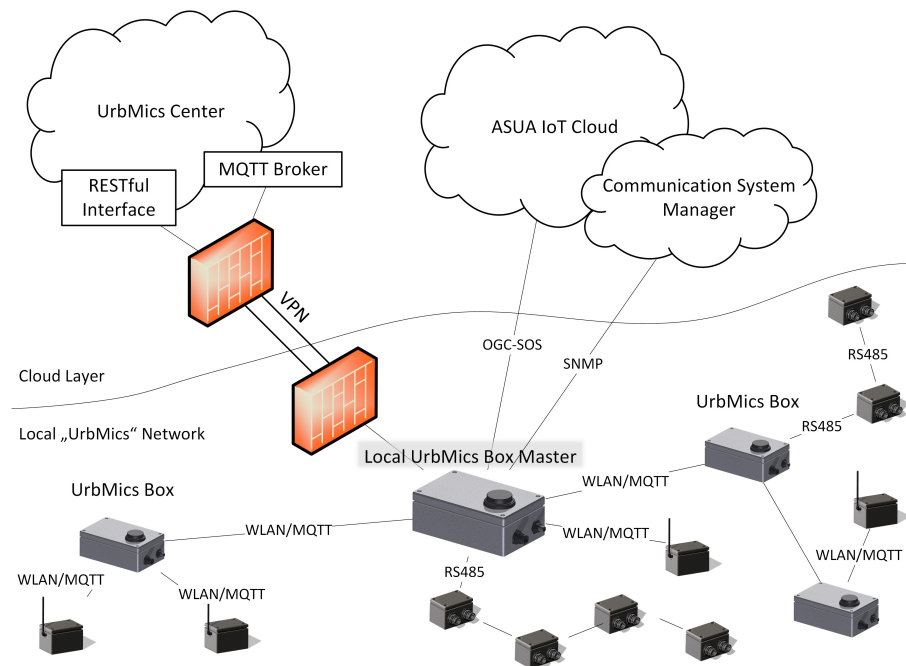


Fig. 4.8 Relation between monitoring sensors and devices and the two cloud systems, the private (UrbMics Center) and the public one (ASUA IoT Server).

When the monitoring data is transmitted to the public cloud via the private one the design of the system is easier and the local devices require less functionality and less configuration efforts. It is simpler to implement just one defined communication interface, where vendor wide the same standard is used and all functionalities are taken into account. Also all possibilities for data uplinks and configuration downlinks are implemented. The received data is processed (e.g. filtered or converted) and stored in the private cloud and then forwarded to the public one. During this processing the data may be checked for failures or inconsistencies and so it can be verified, that just validated data is forwarded to the public cloud.

In a system design, where the monitoring devices transmit the data directly to the private and the public cloud the local devices need much more features. The design of the configuration mechanism and the wide variety of communication interfaces lead to rather complex devices. Not only, that there are different communication standards and protocols (HTTP, FTP, TCP/UDP, RESTful HTTP, Ajax http, Websockets, MQTT, SNMP) and also different machine-to-machine (M2M) formats like XML

and JSON are used.

Since it is difficult to cover all different options and possibilities and keep the included features up to date these systems have to be adapted for the specific use case. Cases, when the direct data transmission should be applied are:

1. There is no need for a dedicated private cloud or server side complex data processing before data transmission to the public cloud.
2. The variety of different monitoring devices that have to be adapted is small.
3. The interfaces, that are used by the public cloud are standardised and already implemented.
4. The monitoring devices react directly to events of the cloud system.

The decision whether to use communication via a public cloud or private cloud has to be taken by the responsible person in charge or a case by case basis. In most cases, when suitable and reliable of-the-shelf devices are used, the scenario with the indirect data transmission will be more suitable.

4.5.2 Data and Metadata of Sensors

A key issue of urban automation systems is, that the available data of sensors can be found by type and location to trigger events and for advanced rule processing. The sensors, that are spread over a city, are often not predefined in the location. The system is expanded by new types of sensors that have to be integrated in the existing ecosystem. To enable automatic adaption of various sensors of different types and locations the metadata has to be available for all sensors in the complete monitoring system. This allows a horizontal interaction between different sensor systems without the need for overlaying processes to enabling the interaction of different systems.

Therefore, each sensor has to be registered on the server with metadata to describe the sensor type, location, features of interest and their corresponding units, precision and update intervals. To register a sensor in the ASUA framework the standards of Open Geospatial Consortium - Sensor Web Enablement (OGC-SWE) were implemented. In OGC-SWE the sensors are defined in SensorML, where models for sensors and a XML encoding for their metadata, e.g. properties and location, are provided. This XML file is then used to register each sensor in the public cloud. OGC-SWE also allows to upload sensor data in a machine readable format to the server.

In the ASUA framework a second communication interface for transmitting the data to the cloud using a publish and subscribe principle was implemented. The Message Queuing Telemetry Transport (MQTT) protocol offers an open source transmission protocol that is supported by a wide variety of devices and programming languages and it is simple to implement on different devices.

The ASUA IoT Server hosts a broker that handles the data flow. Devices or systems publish sensor data to the broker via a structured topic name, e.g. *"/ASUA/id123123/temperature"*. The broker pushes the data to all the clients, that subscribed for this specific topic. If the data cannot be transmitted immediately to a subscriber, the data is buffered until it is successfully transmitted to all recipients. The MQTT broker is hosted by the ASUA IoT Server for the data transmission of measurement devices, that are directly connected to the internet. For the case, that devices in a local UrbMics Network are not directly connected to the internet the gateway hosts a dedicated local broker combined with a service, that acts as a relay for transmitting the data to the ASUA IoT Server and/or the UrbMics Center.

However, the sensors have to be registered in the cloud system to provide the metadata as well as to inform the service, that the sensor itself publishes on a specific topic. This registration process is done via RESTful and OGC SensorML and just the data is transmitted via MQTT.

In the ASUA project an update of the software configuration of UrbMics devices via MQTT is also implemented. The UrbMics centre hosts a private MQTT broker that enables a secure connection with authorisation and authentication. An UrbMics device subscribes to a topic on which new configurations for specific devices, e.g. for a device with ID: *id123123* the subscription topic is *"/UrbMics/id123123/config"*, or a device group, e.g. *"/UrbMics/#/config"* whereby *#* is a wildcard to receive all messages of this topic level.

4.5.3 Setting Alarms in ASUA

Some devices of the ASUA system provide alarm setting possibilities, like buzzers and LED's. One wireless node of the UrbMics System is equipped with RGB LEDs to allow alarms via blinking or fading in different colours. To trigger the external alarm a MQTT topic for the devices was established, that allows the system to trigger an alarm in several predefined levels (e.g. L1 = normal situation, L2 = attention, L3 = local alarm, L4 = system wide alarm). Each of the alarm levels is indicated by different colours and different speeds of blinking or fading.

5 | Outlook and Conclusion

Smart monitoring applications are an emerging technology, whereby most systems cannot fulfil the demands on openness for easy integration to supervisory systems. With upcoming event-driven frameworks it is necessary to develop a new generation of smart monitoring devices enabling local data collection and local data processing.

The constrained polynomials enable the embedding of a-prior knowledge about a measurement situation and in this manner improve the quality of the results. In geo-monitoring application the uncertainty of a measurement is highly relevant and the constraints ensure a better confidence interval in each measurement. Furthermore if a limited number of monitoring sensors fail, the reconstruction is still possible with this method. The model-based reconstruction is mathematically so efficient that it can be implemented on an embedded system. This allows solutions with low power devices near the area where the monitoring is performed, e.g. in a mine or at a construction site, without the need for a permanent internet connection for online data processing.

The noise of sensors is not always of Gaussian type, as the detailed analysis of the inclination sensors proved. The sensor noise of the in geo-monitoring commonly used sensor, the Murata SCA103T, is of Cauchy-Lorentzian type. This distribution has no statistical moments, and therefore no mean or variance can be computed. The use of suitable parameter estimation, e.g. the 24 % truncated mean, leads to a significant improvement in estimating the location parameter. The SCA103T inclination sensor consists of two sensing elements, whereby the sensor analysis revealed, that the gain of the two internal sensing elements are not equal. Singular value decomposition allows to determine the appropriate correction factor for each sensor to reduce the noise level by a ratio of 0.66.

Future urban monitoring requires that monitoring devices have to be able to be integrated into larger monitoring systems. To enable autonomous collaboration between heterogeneous systems require, that sensor data and metadata are provided from each system in machine readable formats to enable automatic data exploration and data processing for surveillance services of the monitoring system. Since urban monitoring systems cannot offer all interfaces for every monitoring system by default it is necessary that urban monitoring systems can be extended with manufacturer-specific services and interfaces to enable the integration and control of devices. As this is currently not possible due to a lack of standardisation, it is often necessary to

use an additional private server to operate proprietary monitoring sensors.

The nowadays most commonly used inclination sensor for geo-monitoring tasks, the Murata SCA103T, was discontinued towards the end of the work on this thesis. Since there is currently no replacement high performance inclination sensor with comparable characteristics, high stability and low temperature dependency, the processing of the data of a less precise sensor plays an even bigger role. The next steps in research will be the characterisation of inclination and acceleration sensors and develop appropriate algorithms to improve the precision and stability of these newly used sensors.

In geo-monitoring, the demand for battery-powered sensors that provide data over a period of several years via radio is increasing. The Long Range Low Power (LoRa) radio data transmission technology plays a particularly important role here. Using LoRa, it is possible to reliably transmit sensor data over several kilometres despite a transmission power that is lower than that of WiFi. Data transmission via LoRa to satellites is also possible in a cost-effective and energy-efficient way. For short data transmission distances, Bluetooth Low Energy (BLE), Zigbee 3.0 and the "Narrowband IoT" standard are playing an increasingly important role, compared to the energy-intensive WiFi, and have to be considered as parts of monitoring infrastructures.

With the knowledge gained in this thesis it was possible to develop a new generation of networked sensors and devices for geo-monitoring. The first devices have now been in use for some time and significantly expand the possibilities of real-time data acquisition in tunnel and road construction and other infrastructure projects. Above all, a smooth and simple integration of the smart sensors into different monitoring platforms brings great advantages.

Appendices

A | Review of Statistical Distributions

Sensors are used to monitor objects and processes etc. The sensor data, which is acquired, is perturbed by noise, since there are different influences that interface with the measurement and the sensor itself. The central limit theorem states, that if there are multiple independent random variables or influences, that the normalised sum of these yields a normal distribution.

If it is possible to acquire a theoretical infinite number of measurements then the amount of data is called the statistical population. A statistical sample represents a subset of this statistical population, that is used for statistical analysis. The task in this statistical analysis is to find a model for the noisy sensor data and to estimate the parameters of this statistical model. Various tools are available to support choosing the right probability distribution and definitions for various parameters are available.

A.1 Histograms

Histograms are a simple method to visualize the distribution of a sample. The minimum and maximum of the data span the range of the data, which is then split into equal intervals, the *bins*. For each bin the data points, which lie in the corresponding interval, are counted. In the histogram a bar for each bin with the height of the counts is plotted. This bar series is a discrete estimate for the probability distribution of the data.

In Figure A.1 a noisy dataset is shown on the left side, on the right side the corresponding histogram is shown. Note: Histograms are usually shown vertically, but here for showing the relationship between bins and counts a horizontal visualisation was chosen.

The bars in the histogram represent the density of the data points in the range of all values. This density is also described by a continuous function, the probability density function (PDF) $P(\mathbf{y})$. It is defined as the derivative of the cumulative distribution function (CDF) $D(\mathbf{y})$. Thus, the PDF of a histogram is yielded by

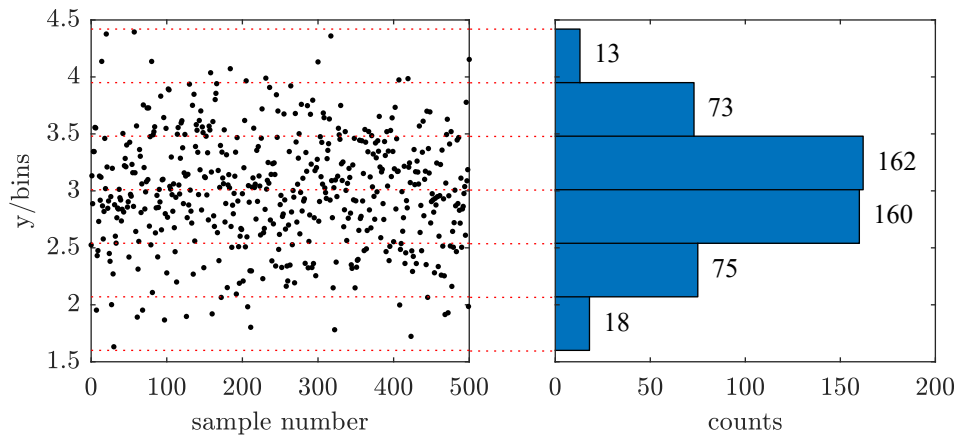


Fig. A.1 Noisy data and the corresponding horizontal histogram; Left: data of $n = 500$ samples with i.i.d. noise; Right: the corresponding vertical histogram for the data on the left side. The count of each bin is plotted beside the bars.

computing the cumulative sum of each bin. The PDF and CDF for a data set with 20000 independent identically distributed (i.i.d.) variables is shown in Figure A.2.

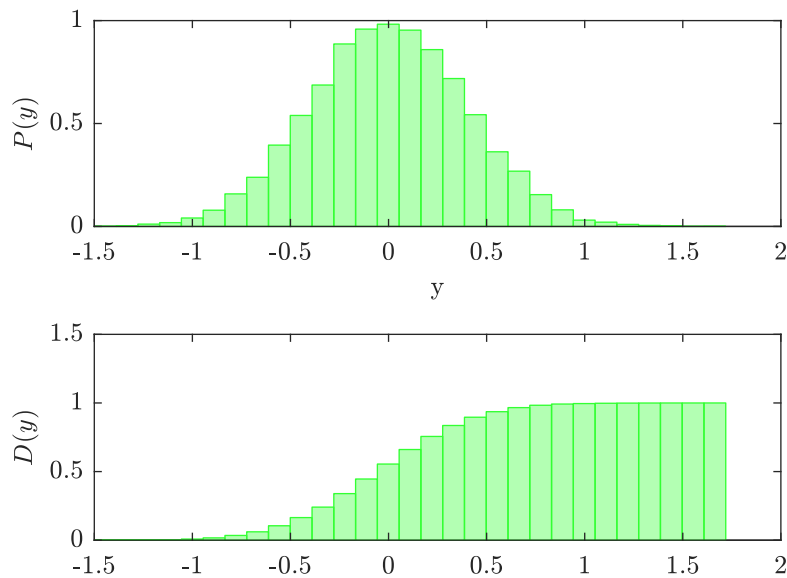


Fig. A.2 Probability density function (PDF) and cumulative density function (CDF) of 20000 i.i.d. variables

If the number of bins is chosen wrongly, this can lead to misinterpretation of the data, since some effects in the data can be lost or there is a high level of noise. There are several rules of thumb for estimating a good amount of bins for the histogram available, a non-exhaustive list includes the methods of the *square root rule*, the *Sturges formula* or the *Rice Rule*. There are also more complex methods available: He [30] proposed a stepwise Bayes rule for finding a appropriate number of bins. These rules are a good support for choosing the number of bins for continuous probability distributions. For discrete probability distributions or digital data other methods for bin generation may be more suitable, since in digital data the values

are a multiple of the sensors least significant bit of the sensors ADC and therefore can just take certain digital levels.

A.2 Statistical parameters

A statistical distribution can be defined by various parameters, e.g. the probability density function of the normal distribution is defined as,

$$f(x | \mu, \sigma^2) = \frac{1}{\sqrt{2\pi\sigma^2}} e^{-\frac{(x-\mu)^2}{2\sigma^2}}, \quad (\text{A.1})$$

whereby μ is the location parameter and σ the standard deviation as a measure for the width of the distribution. Figure A.3 shows the probability distribution function for the standard normal distribution (Gaussian distribution) with $\mu = 0$ and $\sigma = 1$. For an acquired dataset these parameters are not known in general, therefore the

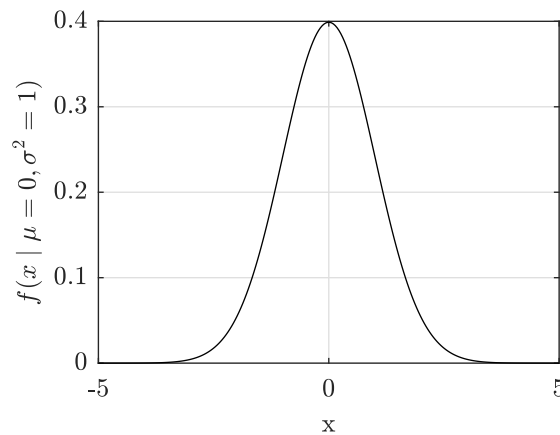


Fig. A.3 Probability density function of the standard normal distribution with the parameters $\mu = 0$ and $\sigma = 1$.

parameters have to be estimated from the sample data. Since not all sensor noises are of Gaussian type, this has to be checked from the sample data. Depending on the nature of the distribution, different ways of computing the appropriate parameters are necessary.

For the parameter estimation of normal distributions the statistical moments can be used. Statistical moments are a specific measure for the form and shape of the distribution. The first statistical moment is the mean value, the expectation of the distribution. It is defined as,

$$\bar{x} = \frac{1}{n} \sum_{i=1}^n x_i, \quad (\text{A.2})$$

and represents the location of the sample as an estimation for the location μ of the distribution.

Since higher degree moments are computed around the mean they are called central moments and for their computation the data is shifted to the centre by removing the mean \bar{x} . The second order moment s^2 is an estimate for the variance σ^2 of the distribution,

$$s^2 = \frac{1}{n-1} \sum_1^n (x_i - \hat{x}), \quad (\text{A.3})$$

and s as,

$$s = \sqrt{\frac{1}{n-1} \sum_1^n (x_i - \hat{x})}, \quad (\text{A.4})$$

as estimation of the standard deviation σ .

The third order moment defines the skewness of the distribution, and the fourth order moment the kurtosis. These moments are not handled in this thesis, but details can be found in the literature [17]. Since a minimum amount of data points is required to yield a reliable estimation the relation,

$$n = 5^d \quad (\text{A.5})$$

can be used as rule of thumb for a rough estimate what data size n is needed to compute a moment of order d . This estimation represents a good starting point for the data size, but depending on the data n may be larger for stable results.

These statistical moments yield a valid parameter estimation for normal distributions, even if the underlying distribution is not known, they deliver admissible parameter estimations. Nevertheless, there are also other estimations for e.g. the location that yields good estimates for other distributions.

For the location of a distribution the mode and the median are often computed. The mode represents the most often occurring value in the sample and the median is the middle of the data, where 50% of the datapoints are smaller and 50% are larger. In Figure A.4 the mean, median and mode are shown for a data set.

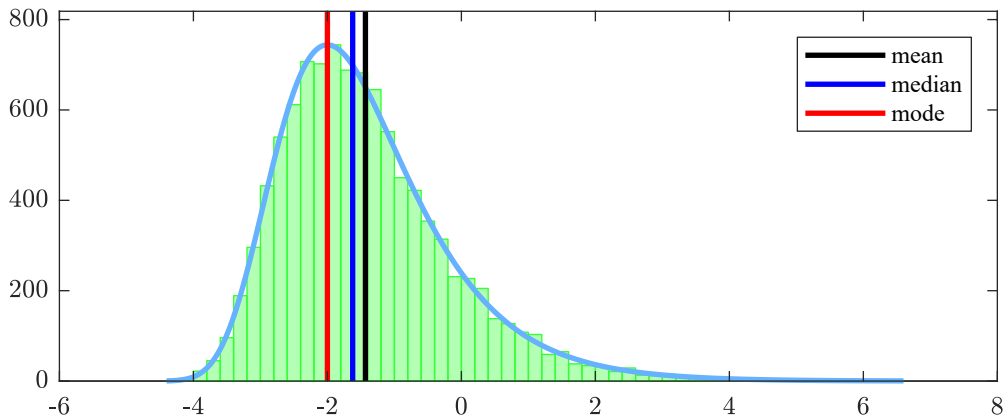


Fig. A.4 Comparison of mean, median and mode

Standard methods in statistics require, that a normal distribution is the underlying distribution of the data. For most datasets this holds true, thus these methods can be applied. Due to this fact most engineers assume that almost all sensor data is perturbed with Gaussian noise and do not check the true nature of the noise. Since there are some distributions where the standard methods do not yield the best estimation for the statistical parameters, also other distributions and the corresponding parameter estimation algorithms should be taken into account. Since the Cauchy-Lorentz probability distribution is an example for a distribution, where, for example, the mean is undefined, dedicated algorithms to estimate the location and dispersion have to be used. This distribution also occurs in the detailed analysis of the Murata SCA103T inclination chip, therefore a review of the Cauchy-Lorentzian is presented here.

A.3 Cauchy-Lorentz Distribution

The Cauchy-Lorentz¹ distribution is defined by

$$f(x) = \frac{1}{\pi} \frac{1}{1 + x^2}, \quad (\text{A.6})$$

in the range $-\infty < x < \infty$. In Figure A.5 the standard normal distribution and the Cauchy distribution are shown, [68].

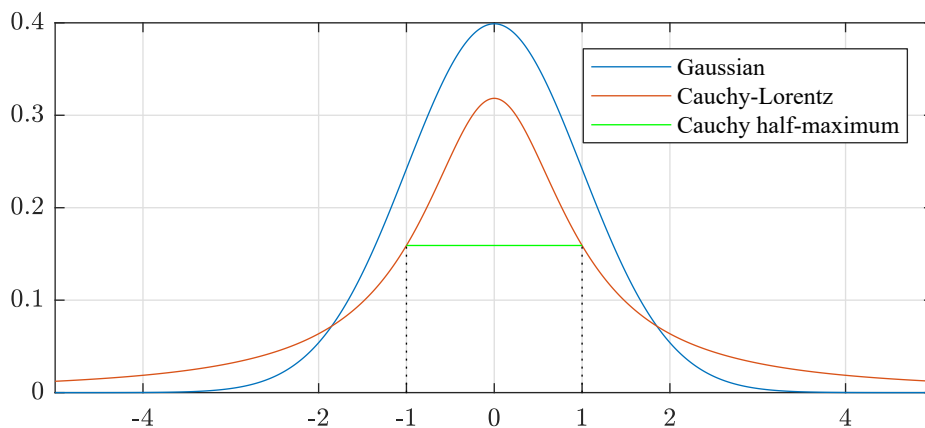


Fig. A.5 Comparison of the standard normal distribution and the Cauchy-Lorentz distribution. The tails of the Cauchy distribution are wider than the ones of the Gaussian.

The mean and variance for the Cauchy distribution are undefined. Compared to the Gaussian distribution, where the mean (first raw moment) converges to a value if the sample size is increasing, the mean of a larger sample size for a Cauchy noise diverges and does not yield a more accurate expectation of the true value. There are also no higher central moments for the Cauchy-Lorentz distribution. Due to this fact, the expectation value of the Cauchy distribution is undefined, [68].

¹or just Cauchy distribution

In the case of the Cauchy distribution the median and mode, which are at $x = 0$, are useful as a measure for the location and the *half-width at half-maximum* (half-maxima at $x = \pm 1$) and are a good estimate for the dispersion [68].

In scientific and engineering domains often the three-term definition of the Cauchy-Lorentz distribution is used,

$$f(x; x_o, \gamma, I) = I \frac{\gamma}{\gamma^2 + (x - x_o)^2} \quad (\text{A.7})$$

whereby x represents the point where the equation is evaluated, x_0 is the location parameter, γ the parameter describing the dispersion and I a scaling factor, [68].

A.3.1 Parameter estimation for Cauchy distribution

The estimation of the parameters for the Cauchy distribution is not trivial, since the mean is not a consistent estimator and the according variance is divergent. In literature [58, 68] often a truncation of the values is proposed to avoid the long tails of the distribution. Rothenberg [58] defined the estimator for the arithmetic average of $2a + 1$ central sample values as,

$$m(a) = \frac{1}{2a + 1} \sum_{i=-a}^a x_i, \quad (\text{A.8})$$

whereby $m(n)$ yields the full sample mean and $m(0)$ the sample median. Finding the minimum extrema of the estimator indicates, that the estimator is minimised when the ratio $r = a/n$ equals 0.2393. Thus, the average of the dataset where the lowest and highest 38 % of the values are neglected is a better estimate for the location parameter than the sample median or the full sample mean.

For estimating the half-width at half-maximum (HWHM) ($\triangleq \gamma$) also no standard procedure is available. In [68] the proposal is given to fit the probability density function to the sample data. Another proposed estimation for γ is the semi-interquartile range, which is defined as the half of the difference between the upper and lower quartile². Thus, an estimator for γ is,

$$\gamma = \frac{1}{2}(Q_3 - Q_1). \quad (\text{A.9})$$

²The quartile are the 25 %, the 50 % and 75 % quantiles, that divide the PDF into four parts of equal probability [68]

A.3.2 Random number generation

For testing and simulating the methods for models based reconstruction, where the noise of the inclinometer sensors is of Cauchy-Lorentian type, it is advantageous to have the possibility to generate data with noise of Cauchy type. To yield a random number in [68] the formula,

$$x = x_0 + \gamma \tan(2\pi\xi) \quad (\text{A.10})$$

is derived from the equation $F(x) = \xi$, whereby $F(x)$ is the cumulative distribution function,

$$F(x) = \frac{\gamma}{\pi} \int_{-\infty}^x \frac{1}{\gamma^2 + (t - x_0)^2} dt, \quad (\text{A.11})$$

and ξ is a pseudorandom number between 0 and 1. An alternative way to achieve random Cauchy noise is,

$$x = x_0 + \gamma \frac{z_1}{z_2}, \quad (\text{A.12})$$

whereby z_1 and z_2 are independent standard normal distributed numbers.

B | List of Figures

| | | |
|-----|---|----|
| 2.1 | Simplified MEMS model: The sprung proof mass is moved by the acceleration which causes the change of the two capacitances C1 and C2. This is used to derive the acceleration and suitable signal conditioning and filtering yields the inclination. MEMS sensors use multiple parallel-plate capacitors on one sensing element. | 10 |
| 2.2 | Sketch of a simplified basic electromechanical system of a pull-in MEMS [57]. | 10 |
| 2.3 | SEM image of a MEMS sensor for measuring acceleration and inclination. The proof mass is placed on the back-side of the structure [9]. . | 11 |
| 2.4 | Comparison of range and sensitivity of different inclination sensors . . | 12 |
| 2.5 | Schematic of the SCA103T inclinometer, [43] © Murata | 12 |
| 2.6 | Photograph of a pair of inclinometers connected to the data acquisition electronics. Each metal cylinder contains one MEMS sensor. In the implementation shown the Sensors are connected using the analogue interfaces, i.e. using the signals VDD, GND, OUT_1 and OUT_2 [63] © 2017 IEEE. | 13 |
| 2.7 | Laboratory set up to measure the stability of the inclinometer measurements. Left top: detail view of the two sensors, the right one with the SPI and the left one with analogue interface and additional data acquisition electronics included. Left bottom: detail view of the the measurement scale. Right: overall view of the complete laboratory set up [63] © 2017 IEEE. | 15 |
| 2.8 | Laboratory measurement to characterize the sensor performance: Top: The tilt measured in [mm/m] for various angles, (blue) precision analogue measurement, (gray) raw SPI data and (red) filtered SPI data 1 Hz bandwidth. The vertical green bars indicate the segmentation of the data for statistical evaluation. Bottom: the measured accelerations [63] © 2017 IEEE. | 16 |

- 2.9 Histogram of the tilt measurements together with the maximum Likelihood Gaussian (red) $\sigma_t = 2.5765 \text{ mm/m} \pm 7.2 \text{ } \mu\text{m/m}$ with 95 % certainty and the maximum entropy Cauchy-Lorentz distribution (blue) with the parameters $x_m = 60 \text{ } \mu\text{m/m}$, $\gamma = 1.2883 \text{ mm/m}$ and $I = 0.219$, [63] © 2017 IEEE. 17
- 2.10 The signal acquired from the SCA103T sensor after evaluation to *tilt*: (black) signal prior to filtering and (red) after filtering. A total of $n = 183\,311$ samples are used for the ensuing statistical analysis, [63] © 2017 IEEE. 18
- 2.11 Histogram for $x - y$ in each of the segments $i \in 1 \dots 11$ denoted by s_i , as shown in Fig. 2.10. The PDF for the Cauchy and Gaussian distributions are shown in red and blue respectively. The corresponding coefficients for the distributions are given in Table 2.2. The histograms have been centered around the median value of each segment, this simplifies the comparison of the results in each segment, [63] © 2017 IEEE. 19
- 2.12 Histogram of the values $x(t)$ and $y(t)$ with their corresponding Gaussian approximations with respective standard deviations, [63] © 2017 IEEE. 20
- 2.13 Deviation of the cumulative distribution functions $P(x)$ and $P(y)$ from their ideal Gaussian models and the respective χ^2 values, [63] © 2017 IEEE. 20
- 2.14 Histogram of the values $p(x - y)$ and $p(x + y)$ with Gaussian (red) approximations. Additionally for $p(x - y)$ a Cauchy-Lorentz (blue) distribution has been approximated, [63] © 2017 IEEE. 21
- 2.15 Bivariate histogram for $x(t)$ and $y(t)$, the color indicates the frequency and is proportional to $p(x, y)$, [63] © 2017 IEEE. 22
- 2.16 Histograms for the orthogonalised values d_{SVD} and s_{SVD} together with the Gaussian (red) and Cauchy-Lorentz (blue) PDF, [63] © 2017 IEEE. 23
- 2.17 Long Term Test stand in laboratory 24
- 2.18 Graph of the data logged from two inclinometers measuring in mutually orthogonal directions. This data was acquired with a measurement interval $t_s = 5 \text{ s}$: tilt of sensor I_1 (blue), tilt of sensor I_2 (cyan) and temperature T (red). There are approximately $n = 10^5$ samples, [63] © 2017 IEEE. 24
- 2.19 Linear estimation of the correlation between temperature and I_2 , the slope is $s_t = -25.53 \frac{\mu\text{m/m}}{\text{dC}}$, [63] © 2017 IEEE. 25

| | | |
|------|--|----|
| 2.20 | Schematic of the SCA830-D07 MEM inclinometer sensor [1]. | 25 |
| 2.21 | The full signal acquired with the SCA830 sensor over a period of approximately one hour. The portions marked in red correspond to all values lying within 1 % (percentile). This data set contains $n = 400\,693$ samples. The values are in LSB acquired directly from the ADC. The device features a 16-bit ADC with a range of ± 1 g, [63] © 2017 IEEE. | 26 |
| 2.22 | Histogram of the SCA830 Signal, with the Gaussian (red) and Cauchy-Lorentz (blue) models for the complete data set, [63] © 2017 IEEE. | 26 |
| 2.23 | Histogram of the SCA830 Signal, with the Gaussian (red) and Cauchy-Lorentz (blue) models for the centered 98 % percentile of the data set, [63] © 2017 IEEE. | 27 |
| 3.1 | Measurement principle for a vertical in place inclinometer measurement [42]. | 29 |
| 3.2 | General mathematical model for a measurement system. The mapping between input \mathbf{x} and output \mathbf{y} is defined by the model $f(\mathbf{x})$ and the corresponding parameters $\boldsymbol{\alpha}$ | 32 |
| 3.3 | A polynomial with three different types of constraints. At location c_1 a known zero constraint is implemented, location c_2 represents a known value pair and at location c_3 a constraint with a defined slope (derivative constraint) is shown [50]. | 39 |
| 3.4 | Example for a physical problem with constraining roots: A simple supported beam has zero constraints on both supports [50]. | 40 |
| 3.5 | Dataset with constraint value pairs: The black dots represent the noisy data, the red dots the constraining value pairs $\mathbf{x}_c = [-0.8, 0.3, 1]^T$ and $\mathbf{y}_c = [-0.5, 0.3, -0.5]^T$ | 43 |
| 3.6 | Particular solution for a value constrained polynomial. | 43 |
| 3.7 | Homogeneous solution for a value constraint polynomial. The homogeneous solution is the residual of the observed data and the particular solution. | 44 |
| 3.8 | The final approximation for the value constrained data yielded from the sum of the homogeneous and the particular solution. | 44 |
| 3.9 | The final approximation for the value constrained data yielded from the sum of the homogeneous and the particular solution. | 45 |
| 3.10 | Normal and derivative constraints on a cantilever. | 46 |

| | | |
|------|--|----|
| 3.11 | Plot of the first six Legendre polynomials in the interval of $[-1, 1]$ | 54 |
| 3.12 | The residual matrix $\mathbf{R} = \mathbf{B}^T \mathbf{B} - \text{diag}(\mathbf{B}^T \mathbf{B})$ for the Legendre polynomials of degree $d = 10$, computed for $n = 100$ nodes. \mathbf{R} is scaled by the first entry of the diagonal of $\mathbf{B}^T \mathbf{B}$ | 55 |
| 3.13 | The first eight Gram-Schmidt polynomials. | 55 |
| 3.14 | The residual matrix $\mathbf{R} = \mathbf{B}^T \mathbf{B} - \text{diag}(\mathbf{B}^T \mathbf{B})$ for the Gram-Schmidt polynomials of degree $d = 40$. \mathbf{R} is scaled by the first entry of the diagonal of $\mathbf{B}^T \mathbf{B}$ | 56 |
| 3.15 | The residual matrix $\mathbf{R} = \mathbf{B}^T \circ \mathbf{B} - \text{diag}(\mathbf{B}^T \circ \mathbf{B})$ for a discrete orthogonal polynomial of degree $d = 500$. The residual error is in the magnitude of the floating-point relative accuracy (eps) available in the calculating system. | 58 |
| 3.16 | Rank deficiency of the differential matrix $\hat{\mathbf{D}}$ computed according Equation 3.121 regarding to the degree of the used basis functions. $\hat{\mathbf{D}}$ is rank-1 deficient up to degree $d = 33$, for higher degrees the differential matrix degenerates and delivers more null-spaces. This is negative for solving inverse problems. | 60 |
| 3.17 | Unitary base \mathbf{G} as starting point for local approximation. | 61 |
| 3.18 | Local projection matrix $\mathbf{P} = \mathbf{G} \mathbf{G}^T$ | 61 |
| 3.19 | Global complete projection matrix $\bar{\mathbf{P}}$, whereby $\bar{\mathbf{P}}$ is of the dimension to span over all given data points m | 62 |
| 3.20 | Schematic representation of a complex measurement field associated with the monitoring of a subway tunnel construction. The white circles form a linear chain of 59 inclinometers monitoring a stretch of railway line. The pink circles correspond to reference measurements points acquired from theodolite measurements, © Geodata GmbH. | 67 |
| 3.21 | Photograph of the inclinometer rods (covered with the yellow tape) mounted in a tunnel along the track, © Geodata GmbH. | 68 |
| 3.22 | Photograph of the end of the inclinometer chain (A) together with a retro-reflector (B) for the total station measurements. © Geodata GmbH. | 68 |
| 3.23 | Result of the data fusion of inclinometer and theodolite measurements, top: (red) an unconstrained reconstruction from the inclinometer data. (green) The theodolite reference points and (black) the constrained reconstruction. Bottom: The difference between the constrained and unconstrained reconstruction, [61] © 2016 IEEE. | 70 |

| | | |
|------|--|----|
| 3.24 | Reconstructions for the 60 elevations, measured with a sampling interval of $t_s = 10$ [min] over a seven day time period. Note that the scaling of the vertical shift is in $[\mu\text{m}/\text{m}]$, [61] © 2016 IEEE | 71 |
| 3.25 | A 40 day observation of the periodic portion of the reconstructed elevation, with the measurement period $t_s = 10$ [min], [61] © 2016 IEEE. 71 | 71 |
| 3.26 | The FFT of the signal from Fig. 3.25. The solid-earth diurnal and semi diurnal tidal modes are marked in red, [61] © 2016 IEEE. | 72 |
| 4.1 | Conditions at a tunnelling construction site at the working face. | 76 |
| 4.2 | Example for Urban Monitoring: During subsurface construction in urban area the measurement points (purple, green and blue circles) are spread over large urban areas. © Geodata GmbH | 77 |
| 4.3 | Wireless Measurement Box: A) robust aluminium case B) IP67 antenna for 800MHz to 2.5GHz C) LED-button for triggering predefined actions. D) IP67 Ethernet connector | 78 |
| 4.4 | System diagram for one configuration of the Measurement Box. | 79 |
| 4.5 | Wireless Measurement Box with hardware for mesh networking; A) RS485 connector B) Power connector C) DC-DC converter D) Network Device E) RS232/RS485 converter F) Embedded device G) IP67 ethernet connector | 80 |
| 4.6 | ASUA Urban Automation Reference Platform Architecture | 82 |
| 4.7 | Example for a local monitoring network with wired and wireless sensors [63]. | 84 |
| 4.8 | Relation between monitoring sensors and devices and the two cloud systems, the private (UrbMics Center) and the public one (ASUA IoT Server). | 85 |
| A.1 | Noisy data and the corresponding horizontal histogram | 93 |
| A.2 | Probability density function (PDF) and cumulative density function (CDF) of 20000 i.i.d. variables | 93 |
| A.3 | Probability density function of the standard normal distribution with the parameters $\mu = 0$ and $\sigma = 1$ | 94 |
| A.4 | Comparison of mean, median and mode | 95 |
| A.5 | Comparison of the standard normal distribution and the Cauchy-Lorentz distribution. The tails of the Cauchy distribution are wider than the ones of the Gaussian. | 96 |

C | Bibliography

- [1] SCA830 Datasheet. Technical report, Murata Electronics Oy.
- [2] IEEE Standard for Radix-Independent Floating-Point Arithmetic. Standard, IEEE Standards Association, Piscataway Township, New Jersey, United States, 1987.
- [3] IEC 60529, Degrees of protection provided by enclosures (IP Code), (Geneva: International Electrotechnical Commission), 2001.
- [4] How Far and How Fast Can You Go with RS-485. Technical Report APPLICATION NOTE 3884, Maxim Integrated Products, Inc., 2006.
- [5] Energiemethoden. In *Technische Mechanik. Festigkeitslehre*. Vieweg+Teubner, Wiesbaden, 2008.
- [6] Geotechnische Erkundung und Untersuchung - Geotechnische Messungen - Teil 2: Verschiebungsmessungen entlang einer Messlinie: Extensometer. Standard, Austrian Standards International, Vienna, AT, 2017.
- [7] Geotechnische Erkundung und Untersuchung - Geotechnische Messungen - Teil 3: Verschiebungsmessungen quer zu einer Messlinie: Inklinometer. Standard, Austrian Standards International, Vienna, AT, 2020.
- [8] D. R. Albert. Monte Carlo Uncertainty Propagation with the NIST Uncertainty Machine. *Journal of Chemical Education*, 97(5):1491–1494, 2020.
- [9] F. S. Alves, R. A. Dias, J. Cabral, J. Gaspar, and L. A. Rocha. High resolution pull-in inclinometer. *2013 Transducers and Eurosensors XXVII: The 17th International Conference on Solid-State Sensors, Actuators and Microsystems, TRANSDUCERS and EUROSENSORS 2013*, (June):928–931, 2013.
- [10] L. C. Andrews and S. of Photo-optical Instrumentation Engineers. *Special Functions of Mathematics for Engineers*. Oxford science publications. SPIE Optical Engineering Press, 1998.
- [11] S. Auci, L. Mundula, and E. Quaquero. Bright Cities and City Information Modeling. 2019.
- [12] E. Barbeau. *Polynomials*. Springer-Verlag, 2003.
- [13] R. Barnard, G. Dahlquist, K. Pearce, L. Reichel, and K. Richards. Gram Polynomials and the Kummer Function. *Journal of Approximation Theory*, 94(1):128–143, jul 1998.
- [14] A. A. A. Beshr and I. M. A. Elnaga. Investigating the accuracy of digital levels and reflectorless total stations for purposes of geodetic engineering. *Alexandria Engineering Journal*, 50(4):399–405, 2011.
- [15] P. Bonate. A Brief Introduction to Monte Carlo Simulation. *Clinical pharmacokinetics*, 40:15–22, 2001.
- [16] J. P. Boyd. Chebyshev and Fourier Spectral Methods. *New York*, page 688, 2000.
- [17] C. Dorman. *Parametrische Statistik. Verteilungen, maximum likelihood und GLM in R.*, volume 53. 2013.
- [18] F. El-Nahhas. Construction monitoring of urban tunnels and subway stations. *Tunnelling and Underground Space Technology incorporating Trenchless*, 7(4):425–439, 1992.
- [19] G. V. C. Freue. The Pitman estimator of the Cauchy location parameter. *Journal of Statistical Planning and Inference*, 137(6):1900–1913, 2007.
- [20] W. Gautschi. *Orthogonal Polynomials, computation and Approximation, Numerical Mathematics and Scientific Computation*. Oxford University Press, 2004.

-
- [21] J. M. Gere and S. Timoshenko. *Mechanics of Materials*. PWS Publishing Company, Boston, 4th editio edition, 1997.
- [22] J. Golser. {F}allbeispiel zur {B}auwerksüberwachung mittels online {N}eigungssensoren. In *25. {C}ristian {V}eder {K}olloquium*, 2010.
- [23] G. H. Golub and C. F. Van Loan. *Matrix Computations (Johns Hopkins Studies in Mathematical Sciences)(3rd Edition)*. The Johns Hopkins University Press, 3rd edition, 1996.
- [24] C. Gomez and J. Paradells. Urban Automation Networks: Current and Emerging Solutions for Sensed Data Collection and Actuation in Smart Cities. *Sensors*, 15, 2015.
- [25] M. Gorawski and K. Grochla. Performance Tests of Smart City IoT Data Repositories for Universal Linear Infrastructure Data and Graph Databases. *SN Computer Science*, 1, 2020.
- [26] J. Gram. Ueber die Entwicklung reeller Functionen in Reihen mittelst der Methode der kleinsten Quadrate. *Journal Fur Die Reine Und Angewandte Mathematik - J REINE ANGEW MATH*, 1883:41–73, 1883.
- [27] C. Gugg. *An Algebraic Framework for the Solution of Inverse Problems in Cyber-Physical Systems*. Phd thesis, Montanuniversitaet Leoben, 2015.
- [28] M. Hägglund Eriksson. *Accuracy and Precision Analysis of Total Station Measurements*. PhD thesis, KTH Royal Institute of Technology, 2014.
- [29] M. Harker and P. O’Leary. Least squares surface reconstruction from gradients: Direct algebraic methods with spectral, Tikhonov, and constrained regularization. In *CVPR 2011*, pages 2529–2536. IEEE, jun 2011.
- [30] K. He and G. Meeden. Selecting the number of bins in a histogram: A decision theoretic approach. *Journal of Statistical Planning and Inference*, 61(1):49–59, may 1997.
- [31] Henri J. Nussbaumer. *Fast Fourier Transform and Convolution Algorithms*. Springer-Verlag Berlin Heidelberg, 2 edition, 1982.
- [32] S. C. Hill, J. Jelemensky, and M. R. Heene. Queued serial peripheral interface for use in a data processing system, 1987.
- [33] ISO. *Road vehicles – Controller area network (CAN)*. International Organization for Standardization, 2015.
- [34] A. Klenke. *Wahrscheinlichkeitstheorie*. Springer Spektrum, 2013.
- [35] R. Kress. *Numerical Analysis*. Springer-Verlag New York, New York, 1 edition, 1998.
- [36] E. Kreyszig. *Advanced Engineering Mathematics*. John Wiley & Sons, 2010.
- [37] X. Liu and B. Akinici. Requirements and Evaluation of Standards for Integration of Sensor Data with Building Information Models. pages 95–104, 2009.
- [38] G. Machan and V. G. Bennett. Use of Inclinometers for Geotechnical Instrumentation on Transportation Projects. *Transportation Research E-Circular*, E-C129(October):92, 2008.
- [39] A. Maier, R. Schmidt, B. Oswald-Tranta, and R. Schledjewski. Non-destructive thermography analysis of impact damage on large-scale CFRP automotive parts. *Materials*, 7(1), 2014.
- [40] MATLAB. *version 9.2.0 (R2017a)*. The MathWorks Inc., Natick, Massachusetts, 2017.
- [41] C. Mgbere, V. A. Knyshenko, and A. Bakirova. Building Information Modeling. A Management Tool for Smart City. pages 177–182, 2018.
- [42] M. T. U. D. Möser, G. INSTITUT, and L. INGENIEURGEODÄSIE). Bauwerk-süberwachungsmessungen, 2004.
- [43] Murata Electronics Oy. *THE SCA103T DIFFERENTIAL INCLINOMETER SERIES*, 2015.
- [44] P. O’Leary and M. Harker. Surface Modelling Using Discrete Basis Functions for Real-Time Automatic Inspection. In *3-D Surface Geometry and Reconstruction*, pages 216–264. IGI Global.
- [45] P. O’Leary and M. Harker. Discrete polynomial moments and Savitzky-Golay smoothing. *World Academy of Science, Engineering and Technology*, 72:439–443, 2010.
- [46] P. O’Leary and M. Harker. A framework for the evaluation of inclinometer data in the measurement of structures, 2012.
- [47] P. O’Leary, M. Harker, R. Ritt, M. Habacher, K. Landl, and M. Brandner. Mining Sensor Data in Larger Physical Systems. *IFAC-PapersOnLine*, 49(20):37–42, 2016.
- [48] P. O’Leary, M. Harker, and T. Suesut. Combined polynomial and periodic moments for the analysis of measured 3D surfaces. *Conference Record - IEEE Instrumentation and Measurement Technology Conference*, (May):354–358, 2008.

-
- [49] P. O’Leary, P. O’Leary, and M. Harker. Discrete polynomial moments for real-time geometric surface inspection. *Journal of Electronic Imaging*, 18(1):013015, 2009.
- [50] P. O’Leary, R. Ritt, and M. Harker. Constrained Polynomial Approximation for Inverse Problems in Engineering. In M. A. Wahab, editor, *Proceedings of the 1st International Conference on Numerical Modelling in Engineering*, volume NME2018, pages 225–244. Springer Singapore, 2019.
- [51] B. Oswald-Tranta and R. Schmidt. Crack depth determination with inductive thermography. In *Proceedings of SPIE - The International Society for Optical Engineering*, volume 9485, 2015.
- [52] B. Oswald-Tranta, R. Schmidt, and T. Grandl. Comparison of samples with flat bottom holes and with hidden occlusions using flash thermography. In *2016 Quantitative InfraRed Thermography*, 2016.
- [53] B. Oswald-Tranta, R. Schmidt, and C. Tuschl. Thermographic investigations of metal inclusions in 3D printed samples. *Proceedings of SPIE - The International Society for Optical Engineering*, 10214:1–9, 2017.
- [54] R. Penrose. A generalized inverse for matrices. *Mathematical Proceedings of the Cambridge Philosophical Society*, 51(3):406–413, 1955.
- [55] B. E. Rapp. Chapter 3 - Engineering Mathematics. In B. E. Rapp, editor, *Microfluidics: Modelling, Mechanics and Mathematics*, Micro and Nano Technologies, pages 21–50. Elsevier, Oxford, 2017.
- [56] R. Ritt and P. O’Leary. Symbolic Analysis of Machine Behaviour and the Emergence of the Machine Language. In *Theory and Practice of Natural Computing*, pages 305–316. Springer International Publishing, 2018.
- [57] L. A. Rocha, E. Cretu, and R. F. Wolffenbuttel. Analysis and analytical modeling of static pull-in with application to MEMS-based voltage reference and process monitoring. *Journal of Microelectromechanical Systems*, 13(2):342–354, 2004.
- [58] T. J. Rothenberg, M. Fisher Franklin, and C. B. Tilanus. A note on estimation from a Cauchy sample. *Journal of the American Statistical Association*, 59(February 2015):460–463, 1966.
- [59] A. Savitzky and M. Golay. Smoothing and Differentiation of Data by Simplified Least Squares Procedures. *Analytical Chemistry*, 36 (8):1627–1639, 1964.
- [60] E. Schmidt. Zur Theorie der linearen und nichtlinearen Integralgleichungen. *Mathematische Annalen*, 63(4):433–476, 1907.
- [61] R. Schmidt, P. O. Leary, M. Harker, P. O’Leary, and M. Harker. Precision Inclinometer Measurement System with a Wireless Gateway. In *2016 IEEE International Instrumentation and Measurement Technology Conference Proceedings*, pages 1–6. IEEE, may 2016.
- [62] R. Schmidt, P. O’Leary, M. Harker, K. Chmelina, and J. Golser. A Smart Multi-Sensor System for Structural Monitoring. In *GeoMonitoring 2016*, Braunschweig, 2016.
- [63] R. Schmidt, P. O’Leary, R. Ritt, and M. Harker. MEMS based inclinometers: Noise characteristics and suitable signal processing. In *I2MTC 2017 - 2017 IEEE International Instrumentation and Measurement Technology Conference, Proceedings*, pages 1–6. IEEE, may 2017.
- [64] M. H. Stone. The Generalized Weierstrass Approximation Theorem. *Mathematics Magazine*, 21(4):167, mar 1948.
- [65] A. Tarantola. *Inverse Problem Theory and Methods for Model Parameter Estimation*. Society for Industrial and Applied Mathematics, jan 2005.
- [66] J. Van Cranenbroeck. Continuous Beam Deflection Monitoring Using Precise Inclinometers. In *FIG Working Week 2007*, Hong Kong, SAR, 13..17 May, 2007.
- [67] A. van Dijk. Smart Cities Report. Technical report, Deloitte Netherlands, Netherlands, 2015.
- [68] C. Walck and P. P. Group. Hand-book on STATISTICAL DISTRIBUTIONS for experimentalists. *Hand-book on STATISTICAL DISTRIBUTIONS for experimentalists*, (September):26–35, 2007.
- [69] J. B. Waldner. *Nanocomputers and Swarm Intelligence*. ISTE, 2010.
- [70] I. working group on general approaches to the design of tunnels. Guidelines for the design of tunnels. *Tunnelling and Underground Space Technology incorporating Trenchless*, 3(3):237–249, 1988.

- [71] X. Xu, L. Ding, H. Luo, and L. Ma. From building information modeling to city information modeling. *Electronic Journal of Information Technology in Construction*, 19:292–307, 2014.
- [72] Y. Yu, H. Liu, D. Li, X. Mao, and J. Ou. Bridge Deflection Measurement Using Wireless. *International Journal on Smart Sensing and Intelligent Systems*, 6(1):38–58, 2013.
- [73] Y. Yu, H. Xie, J. Wang, and J. Ou. Deflection measurement using wireless inclination sensors for bridge. In *2010 International Conference on Intelligent Control and Information Processing*, pages 487–492. IEEE, aug 2010.